Development of a Model for Computational Fluid Dynamics Simulation of Liquefied Natural Gas Vapour Dispersion

Izunna David Udechukwu

Thesis submitted to the Faculty of Science, Engineering and Computing

Kingston University London

In partial fulfilment of the requirements for the degree of

Doctor of Philosophy

May 2015

Major Subject: Mechanical Engineering

Abstract

Liquefied Natural Gas (LNG) is currently playing an important role in the world energy markets. This is evidenced by growing demand and increased construction of LNG facilities across Europe and the United States. In the event of spill from any of the facilities handling LNG such as during liquefaction, transportation or regasification, flammable vapour is formed which disperses through the atmosphere constituting fire and explosion hazards. To ensure public safety in the midst of growing LNG demand and facilities construction, industries are usually mandated to demonstrate that public safety will not be undermined by potential spill from their facilities. One method that is currently being used to demonstrate compliance is through LNG vapour dispersion modelling using Computational Fluid Dynamics (CFD).

CFD modelling of dispersion phenomena is a challenging task that requires rigorous methodology to account for the underpinning physical processes. The modelling process comprises of two steps: source term quantification and vapour dispersion modelling. Source term quantification involves the physical description of spill rate, pool spreading and evaporation. Vapour dispersion utilizes the result of source term quantification in order to predict the turbulent entrainment and dilution process with the ambient wind. Existing models employ simplifying assumptions that circumvents explicit source term modelling. The spilled liquid is assumed to fill the entire substrate immediately at which time the spill rate becomes equal to evaporation rate. Following this assumption, a fixed inlet patch area and evaporation rate is applied at the gas inlet boundary. This approach fails to incorporate the transient pool development and subsequent evaporation into the dispersion modelling process.

The primary aim of this dissertation is to develop an efficient integrated pool spreading, evaporation and dispersion (I-PSED) model code for LNG vapour dispersion simulation. This represents a significant shift from the traditional method since the new methodology combines the spilling process, spreading on substrate and transient evaporation into a unified model. For the spilling process, the well- known orifice model has been adopted to predict the spill rate taking into account the decreasing head. A mass balance approach is adopted in conjunction with a well-established similarity model for spreading calculation. Heat transfer to the spreading

pool is incorporated based on film boiling correlation. The spreading model was then coupled to an atmospheric dispersion model within OpenFOAM framework through the implementation of a new boundary condition in which the gas inlet patch area changes based on the instantaneous pool radius.

The developed integrated code (I-PSED) is validated against data from the Coyote Series LNG Spill experiments as well as against Shell's Maplin Sand LNG spill experiments. Predictions of concentration obtained using the proposed model and those obtained using conventional approach are compared against experimental data at specific sensor locations. Also, arc-wise comparisons are carried out. Predicted results show good agreement with experimental data and clearly put the newly developed model ahead of the conventional approach for CFD simulation of LNG vapour dispersion. With the newly developed approach, the cloud arrival time and average concentrations at most sensor locations were better predicted. The effect of the turbulent production due to density stratification (buoyancy) created by the release of cryogen is investigated. Experience gathered shows that incorporation of a production term due to buoyancy in the turbulence model improves predictions under unstable atmospheric condition, otherwise the concentration field would be grossly over-predicted.

Dedicated to my mother Augustina

Acknowledgement

A deep and special appreciation goes to my supervisors, Dr Siaka Dembele, Dr Ali Heidari, Dr Konstantin Volkov and Professor Jennifer Wen who introduced me to the world of consequence modelling using Computational Fluid Dynamics, which has become a vital tool in addressing safety issues related to the accidental release of flammable gases in the oil and gas industry. Without the unwavering support, expertise and guidance of the supervisory team, it would have been impossible to complete this research project.

I also want to thank my friend and colleague Marco Macchi for useful discussions on object-oriented C++ programming which underpins the OpenFOAM Computational Fluid Dynamics toolbox used in this study. Other colleagues in the centre for fire and explosion studies whose names cannot be mentioned here due to the large number are also appreciated for their great companionship and contributions in one form or the other.

Financial support of Kingston University London, towards this research project is hereby acknowledged

And finally, the support and encouragement which I received from my family in the course of this research, especially at difficult times is deeply appreciated.

Contents

List of Figures

List of Tables

Nomenclatures

Latin alphabets

A_p	LNG pool area
Ar	Archimedes number
As	Sutherland coefficient
a_i	JANAF Coefficients
B_K	Boltzmann's coefficient
B	Cloud half width
Co	Courant number
C_c	Plume centre-line concentration
C_D	Discharge coefficient
C_{pL}	LNG specific heat capacity
C_{pW}	Specific heat capacity of water
C_{pa}	Air specific heat capacity at constant pressure
C_s	Roughness constant
D	Mass diffusivity
D_{eff}	Effective mass diffusivity
$D_p(t)$	Instantaneous pool diameter
E	Energy
E	A wall function coefficient
F_b	Body forces
F_G	Gravitational spreading force
F_I	Inertia spreading force
F_T	Turbulence factor
F_s	Surfaces forces
$F_{\tau,i}$	Frictional resistance to spreading
$\bar{f}$	Filtered variable
G	Filter function
G_b	Turbulence generation due to buoyancy
H	Effective height of release
H_L	Height of LNG above the breach

H_V	Heat of vapourization
h_0	Total enthalpy
h_{air}	Convective heat transfer coefficient
h_f	Film boiling heat transfer coefficient
h_{sq}	Quiescent heat transfer coefficient
h_{st}	heat transfer coefficient accounting for turbulence
J_i	Diffusive flux
K	Thermal conductivity
K_a	Thermal conductivity of air
K_L	Thermal conductivity of LNG
K_V	Von-Karman constant
K_{Vf}	Thermal conductivity of LNG vapour
K_W	Thermal conductivity of water
K_s^+	Dimensionless roughness height
K	Turbulent kinetic energy
L	Monin-Obukhov length
L_C	Critical length
M_a	Air molar mass
M_{evap}	Mass of LNG evaporating
M_s	Molar mass of gas at the source
$M(i)$	Instantaneous mass of LNG in the pool
m	Control volume mass
Nu_f	Film boiling Nusselt number
P	Pressure
Pe	Peclet number
Pr	Prandtl number
Pr_T	Sub-grid scale Prandtl number
Pr_V	LNG vapour Prandtl number
Pr_t	Turbulent Prandtl number
Q	Rate of LNG release
Q_{con}	Conductive heat transfer

Q_{conv}	Convective heat transfer
$\dot{Q}$	Rate of heat transfer to the control volume
q_s	Sub-grid scale heat flux
q_x	Heat flux in x-direction
q_y	Heat flux in y-direction
q_z	Heat flux in z-direction
$\dot{q}_c$	Conductive heat flux
$\dot{q}_{evap}$	Heat loss due to evaporation
$\dot{q}_{rad}$	Radiative heat flux
$\dot{q}_{sub}$	Substrate heat flux
$\dot{q}_w$	Ground heat flux
R	Universal gas constant
$R_p(t)$	Instantaneous pool radius
r_b	Breach radius
R	Position of a computational cell
S_E	Source term in the energy equation
S_{h0}	Source term of the total enthalpy equation
S_K	Spreading constant
S_c	Schmidt number
Sc_T	Sub-grid scale Schmidt number
S_y	A horizontal scaling parameter
S_z	A vertical scaling parameter
T	Temperature
T_*	Friction temperature
T_{air}	Air temperature
T_C	LNG pseudo critical temperature
T_L	LNG temperature
T_s	Sutherland temperature
T_w	Ground surface temperature
t'	Time at which ground is first wetted at a certain point
u^+	Dimensionless near wall velocity

u_*	Friction velocity
u_a	Air velocity
$V(i)$	Instantaneous volume of LNG in the pool
W	Work
X_c	Downwind location of the cloud center of mass
Y_1	Mass fraction
z_0	Roughness length

Greek symbols

α	Heat diffusivity
α_{eff}	Effective thermal diffusivity
α_G	Substrate thermal diffusivity
α_T	Sub-grid scale eddy diffusivity
β	Cloud half width parameter
Γ	Generalised coefficient of turbulent diffusion
γ_k	Sub-grid scale species fluxes
$\overline{\Delta}$	Filter width
δ_v	Control volume
ϵ	Surface emissivity
ε	Energy dissipation rate
η	Kolmogorov length scale
λ_G	Substrate thermal conductivity
μ	Dynamic viscosity
μ_a	Air dynamic viscosity
μ_T	Sub-grid scale eddy viscosity
μ_t	Turbulent viscosity

μ_V	Dynamic viscosity of LNG vapour at film temperature
ν	Fluid kinematic viscosity
ρ_a	Air density
ρ_l	LNG density
ρ_V	Density of LNG vapour
ρ_W	Water density
σ_s	Interfacial surface tension
σ_y	Standard deviation of plume concentration in the y-direction
σ_z	Standard deviation of plume concentration in the z-direction
τ_{ij}	Viscous stresses
τ_{ijSGS}	Sub-grid scale viscous stresses
τ_{wall}	Wall shear stress
φ	Pool thickness
ϕ_m	Monin-Obukhov parameter
φ_{min}	Minimum stable pool thickness
Ψ	A flux limiter

Chapter 1: Introduction

Global commitment to emission reduction and greener technology has led to a substantial increase in the use of natural gas in the recent years. This trend is expected to continue as natural gas is considered a viable alternative energy in the quest for a sustainable energy future. But natural gas fields are sometimes located in areas too remote from the consumers for economic transport through pipelines. In such situations, the gas is converted into liquid state referred to as Liquefied Natural Gas (LNG) and transported through large ships fitted with LNG tankers. The liquefaction process involves condensing the gas by super cooling at atmospheric pressure, reducing the specific volume by about 600 times compared to the gaseous state [1]. Considering the enormous reduction in volume achieved through liquefaction, the liquid state provides cost effective natural gas transportation over long distances offshore and onshore. Furthermore, storage space is maximally utilized in event that LNG needs to be stored in order to meet demand at peak seasons. Based on these reasons, LNG is expected to play a vital role in the world energy markets at least in the next several years

1.1. LNG properties

LNG is a highly flammable hydrocarbon mixture consisting mainly of Methane (typically 85 to 96%) and a small fraction of other hydrocarbons such as butane, ethane and propane. Its boiling point is considered to be -163^0C, the boiling temperature of methane being the major and most volatile constituent. Upon release in event of accidental spill, the cryogenic liquid forms a heavy gas cloud with density in the order of 1.15 times the density of air [2, 3] This leads to an initial negatively buoyant gas cloud which flows very close to the ground until it mixes with the ambient air and warms up sufficiently to become less dense than air thereby rise and disperse more rapidly. A full description of LNG properties has been reported elsewhere [4].

1.2. LNG facilities and associated hazards

The liquefaction, transportation and regasification of LNG necessitate the use of a range of facilities in the industry. These can be categorised into land-based and floating units. While the land based facilities such as storage tanks, liquefaction and

regasification plants are common in the industry and in the literatures, their floating counterparts are less known. For instance, an LNG FPSO (floating production, storage and offloading unit) as shown in Figure 1-1 processes hydrocarbon and liquefies gas to produce LNG. Similarly, an LNG FRSU (LNG floating storage and regasification unit) receives LNG and regasifies it to provide gas to an onshore consumer or the market gas grid.

Figure 1-1: A typical LNG FPSO [5]

In event of spill from an LNG facility, a flammable vapour cloud is formed which disperses through the atmosphere constituting fire and explosion hazards. A dispersing flammable gas cloud which travels unignited could pose health and safety issues such as asphyxiation and cryogenic hazard. If ignited by the initiating event or an external ignition source, it may result in fire and the flammable cloud would not travel a significant distance [6].Typical hazards associated with LNG include Asphyxiation, Fire, Rapid Phase Transition (RPT), Vapour Cloud Explosion (VCE) and Roll over.

1.2.1. Asphyxiation

The presence of high concentration of LNG vapour in the atmosphere could result in asphyxiation which is a condition of severely deficient supply of oxygen to the body. According to a previous study by Pitblado [3], dilution of oxygen in the breathing zone to below 15% results to impaired behaviour, below 10% causes vomiting and

nausea and below 6% it can lead to death. LNG concentrations required to reach this threshold is 28.2%, 52.2% and 71.3% respectively. For spills in outdoor environment, these concentration levels are only possible near the vicinity of a spill. Moreover, the effects of wind meandering and defensive measures taken by individuals close to the spill make asphyxiation less likely to occur in an outdoor environment. While asphyxiation is expected to be more likely in a confined space, there are fewer tendencies for it to occur owing to industrial regulations regarding confined space entry.

1.2.2. Fire Hazards

LNG readily evaporates upon release to ambient conditions due to its low boiling point. The resulting vapour will start to mix with atmospheric air and thereby get diluted as it is transported downwind of the release. However, some part of the dispersing vapour will still be within the flammability limit (5% - 15% concentration by volume). Should the flammable gas come in contact with an open flame or any source of ignition, the gas cloud would likely ignite causing fire hazard. Three types of fires are associated with LNG and are highlighted as part of this study: pool fire, flash fire and jet fire.

Pool fire- an accidental release of LNG normally results to the formation of a liquid pool on land or water depending on the type of surface around the release area [3, 5].If the pool encounters an ignition source, it may burn resulting in a pool fire. Pool fire can also occur if flammable vapour comes in contact with an ignition source and then burns back to the pool.

Jet fire –flammable gas leak from pipelines or from the base of storage containment usually occur at high pressures giving rise to the release of high velocity jet [7]. If the jet encounters an ignition source while in its limits of flammability, it will ignite resulting in a form of fire generally referred to as jet fire. Jet fires could occur during marine transportation if the LNG is stored at high pressures. It can also occur during unloading or transfer activities owing to high pressures associated with pumping. This form of fire can cause serious damage especially in the immediate vicinity of the release.

Flash fire –flash (or partial evaporation) sometimes occur during the release of flammable gases depending on the release condition such as the presence of a throttling device. In such situation, the dispersing gas cloud may become ignited if it encounters an ignition source. This results to a form of fire commonly known as flash fire. A typical flash fire may burn back to the spill source causing more catastrophic events

1.2.3. Rapid Phase Transition (RPT)

RPT is a pseudo-explosion that occurs due to increased heat transfer to LNG pool causing a sudden phase change from liquid to vapour with an associated rapid increase in pressure. This is not a real explosion as it occurs in the absence of burning. However, it is characterised by explosive kind of sound (loud bangs) emanating from puffs of LNG expelled into the atmosphere. While this phenomenon has never resulted from any major mishap involving LNG, it has been observed in a number of large-scale LNG spill experiments[8].

1.2.4. Vapour Cloud Explosion (VCE)

In event a dispersing gas cloud reaches an enclosed area such as a building, the build-up of the gas can increase its concentration up to the flammability range. Upon contact with an ignition source, explosion may occur which is generally known as vapour cloud explosion. Air intakes into buildings are usually elevated above heights attainable by most LNG dense vapour clouds to reduce the possibility of vapour induction into the building [4]. Thus a vapour cloud explosion is very unlikely to occur in buildings.

1.2.5. Rollover

Rollover is a hazardous event that occurs in LNG storage tanks due to stratification. The term stratification means the existence of two or more layers of liquid in a containment and the interface between any two layers is characterised by sharp gradient in density. Stratification can be fill-induced if a storage tank containing LNG is further filled with LNG of different density such as in a peak shaving plant or it can result from the presence of Nitrogen in the storage tank in which case it is referred to as autostratification. If the liquid at the top becomes denser than that at the bottom such that liquid rises from the vbottom to the surface. By moving to the

top, the liquid which was originally at the bottom loses pressure in proportionate to the head of the liquid in the tank [6].This drop in pressure reduces the boiling temperature thereby making it more likely that the liquid at the top might be above its boiling point and therefore vaporise. Considering that expansion ratio is 1:600, even a small flash can produce a very large volume of LNG vapour. The corresponding pressure build up within the tank can exceed the relieve valve design value prompting containment failure. Rollover can result in a significant fuel loss or lead to a more devastating incident under extreme conditions.

1.2.6. Cryogenic effects

LNG tankers are designed to ensure that LNG does not contact the hulls, but incidents can occur that will bring LNG into contact with the inner surface or the outer surface of the hull. This has the potential to cause low temperatures in areas that are not designed for such low temperatures, leading to some sort of brittle fracture. This type of structural failure was the main cause of an explosion that occurred in 1994 in Ohio [4].

1.3. Regulatory requirement

The aim of regulatory authorities is to reduce, possibly to near-zero, the risk and adverse environmental effects (damage to LNG facilities and more importantly human casualties) which could result from accidental spill. This is implemented in different parts of the world using nationally recognised codes and standards. In Europe, the code and standards specific to LNG handling include: EN 1473 which specifically addresses the risk assessment, including need for consequence modelling. This code has been well incorporated into the British Standards. Certain US standards can also be applied in Europe, including the NFPA 95A and 33 CFR part 127. The Chinese LNG industry is currently using European and US codes and India has developed its own high level codes based on a combination of certain elements of EN 1473 and NFPA 59A and referred to it as OISD STANDARDS. Therefore only EN1473 and NFPA 59A will be discussed further in this section.

1.3.1. BS EN 1473:2007

The EN 1473 as enshrined in the British Standards deals with procedures and practices that will result in safe and environmentally acceptable design, construction and operation of LNG plants[9].In section 4.4, it stated that a hazard assessment must be carried out during plant design and after a major retrofit to an existing plant. The acceptable methodology for hazard assessment is summarised in section 4.4.2.1 which includes the determination of the consequences of a potential spill, and in section 4.4.2.5, atmospheric dispersion calculation has been specifically mentioned

1.3.2. NFPA 59A:2013

Section 59 A of the National Fire Protection Agency (NFPA 59A) deals with safe production, storage and handling of LNG[10]. Issues related to hazard and consequence assessment of releases of LNG is presented in section 15.8.The need to use a mathematical model to predict distance to vapour concentration equal to the lower flammability limit has been emphasized. Furthermore, it is stressed that the model must be validated against experiment before it can be deemed a reliable tool for hazard assessment.

1.4. Phenomenology of LNG Vapour Dispersion

Upon release of LNG due to breach of containment, some vapour is generated immediately with some liquid suspension (aerosols) so small that they are unable to settle out of the gas/air mixture.

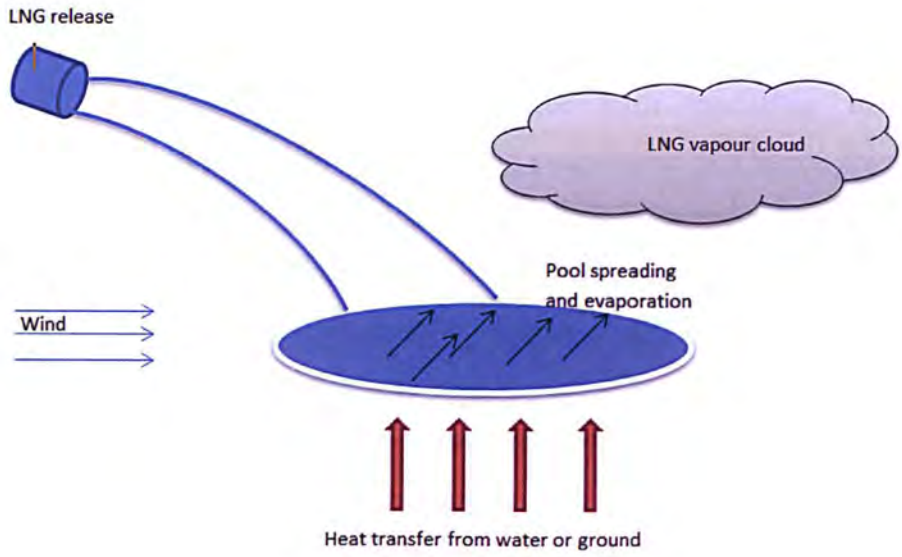

Figure 1-2: LNG release, pool spreading, evaporation and dispersion phenomena

The aerosol and vapour generated will immediately contribute to the LNG vapour cloud formed. However, considering that LNG is stored as a saturated liquid, only a small amount of it will flash to produce droplets. Most of the LNG will fall on the surface beneath (water or ground) as liquid and spread under gravity and inertia. As the liquid pool spreads, heat transfer from the water or ground causes it to evaporate. Thus, vapour emanating from the pool is the major source of vapour cloud as shown in Figure 1-2.

1.5. Motivation and Objective

Owing to the different types of hazards associated with the accidental release of LNG onshore and offshore, authorities in developed nations require the use of consequence models for risk assessment of LNG terminals. Consequence modelling refers to the prediction of the concentration field following a given spill scenario. The so called integral models earlier developed, performed relatively well but they are only one dimensional and hence unsuitable for real life dispersion scenarios[11]. One method that is currently gaining popularity is Computational Fluid Dynamics modelling[12]. However, CFD modelling of LNG dispersion is a challenging task and hence amenable to individual expertise in accounting for the underpinning physical processes.

Typically, consequence modelling of hazardous releases due to breach of containment should be carried out in two stages: source term modelling and atmospheric dispersion modelling [7]. Source term modelling involves the description of the spill rate, pool spreading and evaporation and hence provides input data for vapour dispersion calculation. Atmospheric dispersion modelling on the other hand involves the description of the time and space evolution of the vapour arising from the source term. According to Webber et al [7], hazard ranges will be of the order of some power of source parameters: pool size and vapour production rate. In agreement Irvings et al. [13] succinctly stated that the source term for dispersion calculation crucially depends on the area of the pool and its rate of evaporation. But, in most existing CFD models of LNG dispersion a fixed pool size and evaporation rate are prescribed directly, hence pool spreading and evaporation are not modelled and couple with dispersion[14-17].An assumption that underlies this traditional approach is that the pool spreads and quickly fills the substrate after which a quasi-equilibrium state is reached when spill rate equals the evaporation rate. Thus, a constant mass evaporation rate is applied over a fixed area (entire substrate) to represent the gas inlet boundary. This is clearly a non-physical assumption as spill rate cannot equal evaporation rate for the entire duration of the spill. Moreover, the Esso LNG spill experimental data as reported by Hissong [18]and previous source models [5, 6]have shown that the pool size varies in time. These works also reported that as the pool spreads, the area in contact with the substrate increases which consequently increase the mass evaporation. Thus, dispersion models which could account for time varying pool size and evaporation have been highly encouraged in one classical report by UK Health &Safety Executive (HSE)[7]. However, they recognised the difficulty in incorporating time varying pool sizes and evaporation rate in CFD models due to the need to couple the source term and dispersion model together. This is further complicated in the case of spills on water surface where transition from film boiling to nucleate boiling can take place. This present work therefore focuses on the development of a coupled model for LNG release, pool spreading, evaporation and dispersion modelling within the framework of OpenFOAM CFD toolbox. The expected output of this work is to provide a unified code in which explicit source term modelling is carried out to provide input to dispersion model, rather than make unrealistic assumptions. In the overall, the objectives of this work include:

Dispersion model development – A basic atmospheric dispersion model will be developed from a C++ CFD toobox generally known as OpenFOAM. This toolbox is chosen as it is open-source and allow programming access into the source code, hence allows unlimited implementation of physics to suit problem being solved. Thus, a combustion model available within the chosen toolbox will be modified by deleting the reaction term in the species transport equation thereby eliminate any form of combustion.This transforms the combustion solver into a cold flow solver thereby making it suitable for simulation of atmospheric dispersion of LNG vapour. However, since LNG has unique properties as a cryogenic and heavy liquid, the basic solver needs to be supported with submodels in order to fully characterise the processes that underlies the dispersion process. The vapour generated in the event of spill is buoyant as the liquid fuel is cryogenic, hence the effect of buoyancy on the generation of turbulent kinetic energy will be incoporated into the basic dispersion model developed.This will be achieved through the addition of a buoyancy term to a standard k-ε model available in OpenFOAM. Also, the effect of density stratification in the atmosphere will be incoporated through the creation of profiles of velocity, temperature, turbulent kinetic energy and its dissipation rate as wind inlet conditions, based on the atmospheric stratification condition under which the spill occurs. Another key process that will be characterised is the process of vapour generation – a process known as source term modelling in the vapour dispersion modelling community.The inclusion of a source term model is a major contribution of the current project as previous studies relied on simplifying assumptions (spilling rate equals vapour generation rate) rather than model the source term.

Source term model development – Source term refers to the series of processes that occur in the near field of a spill, including the liquid discharge, pool formation and spreading, heat transfer to the pool and subsequent vapourization of the pool. The implication is that source term model provides input to the vapour dispersion model, hence accurate representation of the source development is critical to the success of a dispersion model. For the liquid discharge process, a well known formulation (orifice model) will be used to obtain the mass flow rate of liquid from a breached containment. The spilled liquid reaches the substrate and spreads, hence the spreading process will be characterised based on a similarity model that hinges on a

balance of inertia and gravity forces. Mass conservation will then be applied to determine the instanteneous mass and hence volume of liquid in the spreading pool. As the pool spreads, heat transfer from the substrate causes it to vapourise generating vapour which is then advected by the dispersion model. The heat transfer to the pool will be modelled here based on film boiling and the vapourization process is characterised by applying energy balance.

Unification-It has been mentioned that the source term model supplies input (vapour) to the dispersion model, hence these two models have to be unified/coupled in some sense. Coupling the spreading and evaporation model to dispersion model will be done here through the development of a new boundary condition (LNG inlet boundary) which could read instantaneous results of the source term model and supply it as input data for dispersion calculation. In particular, the newly developed boundary will first read the instantenous pool radius and vapourization rate from the source term model.Using the vapourization rate read and knowing the density of LNG vapour at its boiling point, an instanteneous upward directed velocity is applied on the boundary cells within the instanteneous pool radius. For cells outside of the radius, the velocity is set to zero to represent zero vapourization rate which means that the cell has not been wetted. This unified model will be called integrated pool spreading, evaporation and dispersion (I-PSED) model in this study and would be validated using experimental data published in the literatures .

1.6. Thesis outline

This thesis is sectioned into five chapters. After the Introduction (Chapter 1), Chapter 2 presents a comprehensive literature review of LNG dispersion modelling approaches. This includes a discussion of the merits and shortcomings of early models i.e. the so-called integral models, presentation of the governing equations and closure relationships for CFD models. Existing CFD models (Ansys, FLACS, FDS, Star-CD) are then highlighted focusing on their strength and limitations. An alternative method (integrated model) is then proposed, followed by a discussion of the key aspects of source term (physics and modelling) to prepare ground for the actual model development carried out in chapter 3.

Chapter 3 presents the actual model development. Considering that there is no specific model in OpenFOAM for LNG dispersion simulation, it started off with

modification of an existing combustion model in OpenFOAM for dispersion application. This is complimented with a number of sub models accounting for the effect of atmospheric stratification and stability (stable, unstable and neutral) conditions at wind inlet boundaries. Then, a source term model is developed with a proper description of governing equations and solution method. Finally the two models (dispersion model and source term model) are coupled together through the creation of a new boundary condition which has been referred to as 'poolInletTempFixedValue' in this present study. Steps taken in the coupling process were duly shown.

In Chapter 4 the integrated model is then validated through the simulation of the Coyote LNG Spill experiments as well as the Maplin Sands LNG spill tests. First and foremost, a grid sensitivity analysis was carried out to ensure model predictions are independent of grid. Afterwards, Both Coyote and Maplin Sands series of experiments involving the spill of LNG were simulated using the new model developed as well as using the conventional approach, and results compared against experimental data. Both point-wise and arc-wise comparisons were carried out as recommended by the UK HSE through its Model Evaluation Protocol (MEP). Further validation studies were carried out via the simulation Shell's Maplin Sand experiment. Afterwards, the validated model is employed in a parametric study to assess the effects of certain key parameters.

Finally Chapter 5 presents concluding remarks and directions for future work. This includes a discussion of the tremendous effect of wind meandering and the need for further studies in this area. Other key areas requiring research attention were also highlighted, including the need to further investigate the effect of water-LNG turbulence on pool vapourization.

Chapter 2: Review of LNG vapour dispersion modelling approaches

LNG vapour dispersion modelling refers to the mathematical description of the flammable vapour transport in the atmosphere following a potential spill. The term dispersion in the modelling community is used to describe the combined processes of convection (due to the wind) and diffusion (due to turbulence) that occurs within the atmospheric boundary layer in the presence of any specie other than those constituting a pure air mixture. The concentration and temperature field of the flammable vapour following the release of LNG into the air may therefore be described by an advection-diffusion equation.

Dispersion modelling is an excellent example of interdisciplinary research area that has direct application in the LNG industry as a formidable tool for risk assessment. Furthermore, it forms the basis for an extensive and active body of current research in the academia and in the industry.

In the early years before the use of mathematical modelling became popular, LNG dispersion has been studied experimentally. Nowadays, the use of experiment to quantify the series of events following a spill of LNG has been rare. This is partly due to the high cost associated with such experiments and the potential risk involved. However, previously performed experiments are still useful as they provide data for the validation of models.

Different modelling approaches have been used in the past and in the recent times to study LNG vapour dispersion. These can be broadly categorised into those that assume the dispersing vapour to be passive and are known as the Gaussian plume models, to those that assume the plume to have a predefined shape (called integral models) and finally, those that rely on the equations that govern fluid motion known as Navier-stokes or Computational Fluid Dynamics models. In this present study, Computational Fluid Dynamics approach will be used as it is the only method that can handle complex terrain typical of realistic LNG vapour dispersion scenario. All three modelling techniques are first discussed, highlighting the gaps associated with each technique. Then a methodology will be proposed and used to advance the existing CFD methodology for better description of the physics of LNG vapour dispersion phenomena. The actual development of the proposed methodology will be presented in Chapter 3.

2.1. Gaussian model

The Gaussian model is the oldest of all LNG dispersion models. It assumes that the LNG vapour cloud has a Gaussian distribution in the vertical and horizontal direction [19], meaning that the concentration field is a normal probability distribution. In this model, the downwind concentration of the LNG vapour emanating from a continuous source of effective height (H) is calculated from[20]:

$$c(x,y,z,H) = \frac{Q}{\pi U(x)\sigma_y\sigma_z} exp\left[-\frac{y^2}{2\sigma_y^2}\right]\left\{\exp\left[-\frac{(z-H)^2}{2\sigma_z^2}\right] + \left[-\frac{(z+H)^2}{2\sigma_z^2}\right]\right\} \quad (2\text{-}1)$$

Where Q is the release rate per unit time, U is the convective velocity and is specified as an increasing function of x.The geometrical parameters σ_y and σ_z are the plume width and plume height respectively and are related to the turbulent diffusivities. Considering that the turbulent diffusivity is not known beforehand, the plume dimensions are parameterised from experiments and observations, particularly from the atmospheric stability condition. Thus, Gaussian models assume dispersion of LNG vapour is dominated by atmospheric turbulence, hence ignore dense gas effects. Moreover, the underlying assumption of a normal distribution does not fully represent the actual physics of dispersion process as it would not capture a range phenomenon including the possibility of cloud bifurcation.

2.2. Integral dense-gas models

Upon release of LNG, a heavier-than-air vapour is formed initially which undergoes three stages, comprising of negative-buoyancy dominated dispersion, neutral buoyancy stage and finally as a positively buoyant vapour at which time it behaves as a passive vapour. Due to the limitation of Gaussian type models in handling negative buoyancy; the need for a new approach became apparent leading to the development of a number of dense-gas models. These early dense gas models are based on self-similarity assumption and are commonly categorised as integral models. These models assume a predefined shape for the cloud and then advance the dimensions in space by modelling increase of the vapour cloud dimensions due to ambient wind entrainment. This entrainment is idealised to be the sum of the

contributions from the edge of the vapour cloud and through its top. A number of integral models have been developed in the past, including DEGADIS(US coast guard), HEGADIS (Shell oil), Cirrus (British Petroleum), SLAB, PHAST (DNV), with DEGADIS and SLAB being among the most widely used due to their simplicity of use and fast computational time [21-25].

2.2.1. Integral dense-gas model: DEGADIS

Dense gas dispersion (DEGADIS) model was developed by Havens et al[26] as an adaptation version of Shell HEGADIS model. Although the original version has undergone certain modifications to cope with passive clouds, the general principle hinges on the tendency for a dense gas cloud to fall towards the ground, even when released vertically upwards as a jet. As the vapour cloud slumps, the momentum associated with the fall causes the centre of the cloud to dip while the edges bulge. This causes the cloud to bounce back to resemble a layered cylinder in which the vertical dimensions are a small fraction of the horizontal dimensions[27] .This pancake-shaped cloud then gets entrained in the ambient wind which elongates and spreads it along as shown in Figure 2-1below.

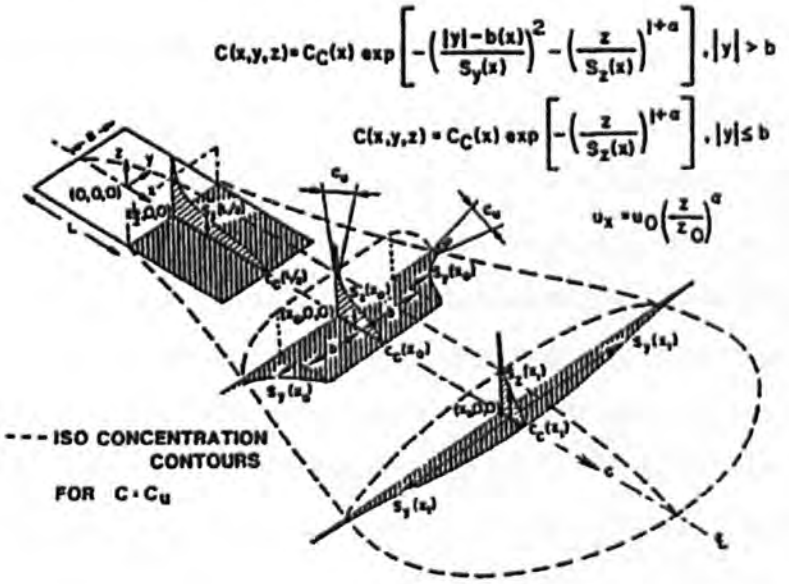

Figure 2-1: Schematics of dispersing heavy gas cloud used for DEGADIS model [26]

The model treats the dispersion of LNG vapour entrained into the wind from an idealised rectangular source of length L and width 2b as shown in Figure 2-1 above. Wind flow is in the positive x direction and is modelled using a power law profile.

For the calculation of downwind dispersion, DEGADIS assumes a power law concentration profile in the vertical direction and a modified Gaussian profile in the horizontal direction[26]. This results to a similarity form for the concentration profile representing the cloud as a homogeneous centre section with Gaussian concentration profile edges:

$$c(x,y,z) = \begin{cases} c_c(x)exp\left[-\left\{\frac{|y|-b(x)}{S_y(x)}\right\}^2 - \left\{\frac{z}{S_z(x)}\right\}\right], & \text{for } |y| > b \\ c_c(x)exp\left[-\left\{\frac{z}{S_z(x)}\right\}^{1+\alpha}\right], & \text{for } |y| \leq b \end{cases} \quad (2\text{-}2)$$

Where c is the concentration, c_c is the centreline ground level concentration, b is the cloud half width measured from the centreline to the edge, S_z and $S_y$are the vertical and horizontal concentration scaling parameters, respectively. These dependent variables (c_c, b, S_yandS_z) are obtained through the solution of a set of ten coupled equations: curve-fit to experimental data for vertical mixing, Richardson number, effective cloud depth, vertical turbulent velocity, plume effective half width, lateral spread, vertical source distance, energy balance, mass balance and an equation of state[26].

2.2.2. Integral dense-gas model: SLAB

The SLAB model was originally developed by Morgan et al[28] but has been substantially improved by Ermak [29] under the joint financial support of USAF and American Petroleum Institute (API). Even though the model was developed to treat denser-than-air releases in mind, it has the capability to also simulate neutrally buoyant clouds including lofting of the cloud as it becomes lighter-than-air. SLAB treats the dispersion of an LNG vapour from a rectangular source of an elevated area as shown in Figure 2-2.Applying the conservation laws to the idealised source results in a set of equations describing the conservation of mass, momentum and LNG vapour mass fractions. The dispersion is considered to occur in two stages comprising a steady state plume mode and a transient puff mode. In the steady state plume mode, the conservation equations are averaged over the crosswind plane, hence the downwind distance (x) becomes the only independent variable.

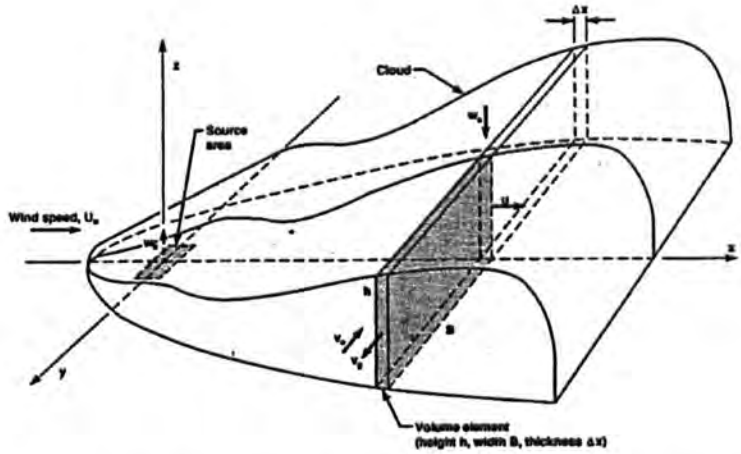

Figure 2-2: Schematics of dispersing heavy gas cloud used for SLAB model[29]

By solving the conservation equations in this mode, together with a set of equations describing the cloud geometry, and an equation of state, the cloud properties (ρ, Y_1, T, U) i.e. density, mass fraction, temperature and velocity respectively are obtained, along with the cloud shape and size parameters (B, b, h, Z_c).Using these parameters, the crosswind plane averaged volume concentration is calculated as follows:

$$C(x) = \frac{M_a Y_1}{M_s + (M_a - M_s)Y_1} \tag{2-3}$$

The subscripts a, and s, stand for ambient air and source respectively, such that $M_a$represents the molar mass of air. The three dimensional volume concentration field $C(x,y,z)$ is calculated through the horizontal $C_1\,(y,b,\beta)$ and vertical $C_2\,(z,Z_c,\sigma)$ profile functions, by assuming a crosswind profile.This leads to a pseudo-three dimensional concentration profile given as:

$$C(x,y,z) = 2 * B * h * C(x) * C_1(y,b,\beta) * C_2\,(z,Z_c,\sigma) \tag{2-4}$$

With the assumed crosswind profiles i.e. horizontal concentration profile and vertical profile expressed as follows,

$$C_1(y,b,\beta) = \frac{1}{4b}\left[\mathrm{erf}\left(\frac{y+b}{\beta\sqrt{2}}\right) - \mathrm{erf}\left(\frac{y-b}{\beta\sqrt{2}}\right)\right] \tag{2-5}$$

$$C_2(z, Z_c, \sigma) = \left(\frac{1}{2\pi}\right)^{\frac{1}{2}} \text{x } \frac{1}{\sigma} \text{x } \left[\exp\left\{-\frac{(z - Z_c)^2}{2 \text{ x } \sigma^2}\right\} + \exp\left\{-\frac{(z + Z_c)^2}{2 \text{ x } \sigma^2}\right\}\right] \quad (2\text{-}6)$$

$$\sigma^2 = \begin{cases} \frac{h^2}{12}, & Z_c > \frac{h}{2} \\ \frac{(h - Z_c)^2}{3}, & Z_c \leq \frac{h}{2} \end{cases} \quad (2\text{-}7)$$

Where $C(x)$ denote the averaged volume concentration, erf stands for error function. Equation (2-4)describes the concentration profile of the cloud in the plume steady state mode.

In the puff transient mode where the cloud is already lofted, an elemental volume of height (h) and half width, B, is selected for the treatment of LNG vapour dispersion as shown in Figure 2-2 above. Cloud properties within the volume are spatially averaged in all three dimensions, so that they are functions of time alone. This makes it possible to derive a set of volume averaged conservation equations for mass, momentum, energy and species transport. These equations form the basis of the SLAB model in the puff mode, along with equations for the downwind location of the cloud centre of mass X_c, the cloud length parameters B_x and b_x and the width parameters B_y and b_y and finally an equation of state to provide closure. With the conservation equation solved for the volume averaged mass fraction, it was possible to define the average puff volume concentration C (t) as in equation **(2-3)**, where the dependent variable is now downwind travel time rather than downwind travel distance. Then, a pseudo-three dimensional time-dependent profile is obtained for the volume averaged concentration in a similar manner as in the plume mode as,

$$C(x, y, z, t) = \left[4 \text{ x} B_x \text{x} B_y \text{ x h x } C(t) * C_1(x - X_c, b_x, B_x)\right] * \left[C_1(y, b_y, \beta_y) * C_2(z, Z_c, \sigma)\right] \quad (2\text{-}8)$$

Both plume and puff models assume air entrainment to account for atmospheric turbulent mixing. Also the effect of ground friction on the vertical wind profile is accounted for using a power law wind profile. Further details of the theoretical background of the SLAB model are available in Ermak [29].Only the transition from the steady state plume mode to the transient puff dispersion mode will be discussed further in the immediate next section.

2.2.2.1. Transition from steady plume to transient puff mode

The transient puff dispersion mode can be entered at the beginning of a simulation through the specification of an instantaneous release or a short duration evaporation source or during a simulation after the release has completed and the steady state period is over[29].In the latter case in which transition from steady state to transient mode occurs during the simulation, there would also be a corresponding transition from the spatially averaged steady state conservation equations to the transient puff conservation equations. As previously discussed, even though both sets of equations are derived by application of conservation laws, in the steady state plume mode the equations are spatially averaged over the crosswind plane, whereas in the transient puff mode, the equations are averaged over all three directions. The time of transition is therefore an important parameter that needs to be specified in order to efficiently transit into the puff transient mode. A common approach is to take this time as corresponding to the end of the release.

2.2.2.2. Analysis of the merits and limitations of integral models

As discussed in the previous sections, integral models employ spatial averaging in the cross wind, plane such that transport equations become a function of downwind distance only. With transport quantities depending only on the downwind distance (x), the original partial differential equations reduce to ordinary differential equations which are then solved. By solving ordinary differential equations in one dimension instead of three dimensional partial differential equations, integral models save computational cost. However, even though three-dimensionality is later implied by assuming profile functions in the crosswind direction and in the vertical direction, these models are inherently one dimensional considering the nature of the governing transport equations and have been described as one in many previous studies of LNG dispersion, including study by Sklavounos and Rigas [14] and PhD thesis of Qi [30] .By being one dimensional, these models cannot cope with the complex terrain typical of LNG dispersion problems, especially in the presence of obstacles such as buildings in the travelling path of the dispersing gas cloud. Moreover, in integral models, certain parameters are tuned based on specific experiment which raises question as to how appropriate it is to employ these models in simulating other spill scenarios outside the conditions for which the model has been tuned.

2.3. CFD modelling technique

Another approach is based on solutions of equations that govern fluid flows in three dimensional space and time, and is generally referred to as CFD models. CFD models even though more computational tasking, includes detailed description of flow physics, and hence is capable of describing the underlying physical processes more accurately compared to integral models [31].With recent developments in computational effort, CFD methodology is becoming increasingly popular replacing the one dimensional integral models which fail at incorporating domain features such as obstacles (buildings) in the travelling path of the dispersing gas cloud. Another key advantage of the CFD approach is that the conservation of mass and momentum of fluid parcels are ensured in the governing equations, rather than rely on semi-empirical formulations as do integral models. Based on the foregoing, CFD approach will be used in this study for the modelling of LNG vapour dispersion. The application of CFD to the modelling of LNG vapour dispersion is challenging and requires adequate knowledge of the key physics underlying the dispersion process.

Figure 2-3 describes the algorithm underlying vapour dispersion modelling. This includes problem definition, solving governing equations of the problem and post-processing of results.

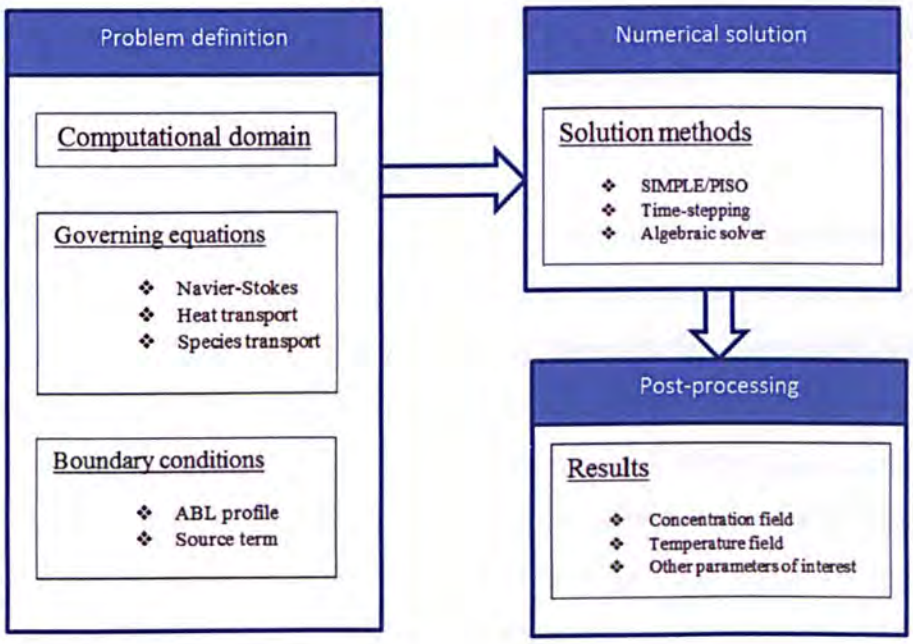

Figure 2-3: Algorithm underlying the CFD modelling technique

Definition of the problem which is to be simulated is a key component of the entire modelling process .It comprises of three elements: (1) computational domain and its discretisation (2) Governing equations specification (3) setting the boundary and initial conditions. The computational domain must be a representative of the physical geometry within which the engineer intends to analyse the flow. Also, the equations must be carefully chosen and well-constructed in a manner that represents the physics of the problem, as wrong equations must lead to wrong results. This is one of the key advantages of using open-source CFD toolbox such as OpenFOAM which grant full access to the source code including governing equations enabling the user to add new equations or modify existing ones, depending on problem physics. OpenFOAM will be used in chapter 3 to further advance CFD simulation of LNG vapour dispersion. Also appropriate boundary conditions must be specified to solve the equations, otherwise the problem will be ill-posed.

In the solution stage, the governing equations are discretised transforming them to a set of algebraic equations which are then solved iteratively to obtain the flow field properties of interest. For risk assessment purposes in LNG industry, the concentrations as well as temperature distribution of the LNG vapour in space and time are required. Care must be taken to adopt right solution technique as inappropriate solution method will result in numerical errors which could accumulate and contaminate the field properties being sought. Finally, the results are post-processed, solution analysed and judgement made accordingly.

2.3.1. Computational domain

Flow modelling in CFD requires the definition of a geometry within which the flow is computed. The domain is then divided into small cells known as control volumes within which the governing equations are solved. Domain size is strongly dependent on the flow scenario being computed as does the size of the cells. It has to be borne in mind also that high cell densities are usually required where high gradients are expected. For LNG vapour dispersion, the region of interest can be the release source and the near-ground region. Coarse cells can be used in other regions. Considering there is no general method for determining these scales, a typical approach is to start with an initially small domain and increase progressively until solution no longer changes as size of the domain or cell is varied. An unstructured or structured mesh

could be used. The use of computational domain also allows the inclusion of obstacles. This is possible due to the inherent three dimensionality of CFD approach as opposed to the one dimensional integral models.

2.3.2. Governing equations

CFD model of dispersion processes are based on the equations governing fluid flows i.e. the three dimensional Navier-Stokes equations for continuity and momentum transport. An energy equation is included to predict the temperature field and a species transport equation is also employed to predict the concentration field. To obtain the set of conservation equations, the fluid flow is modelled with infinitesimally small control volumes fixed in space with the fluid moving through it. In the context of this methodology, the equations are expressed in a standardised conservative form. But it is possible to switch from one form to another through the concept of material derivative:

$$\frac{D}{Dt} = \frac{\partial}{\partial t} + (\vec{U} \cdot \nabla) \tag{2-9}$$

Equation (2-9) above means that the rate of change of a fluid property (mass, momentum, energy, mass fraction) as seen by an observer following the flow equals the rate of change of the property in the control volume fluid element plus the net rate of flow of the quantity across the control volume boundaries. The elemental volume considered is so small that fluid properties at the faces can be expressed accurately enough by using the first two terms of the Taylor's series. For instance, the pressure at the west (W) and east (E) faces which are both halfway from the middle of the elemental volume (see Figure 2-4) can be expressed as follows:

$$P + \frac{\partial P}{\partial x}\frac{1}{2}\delta x \tag{2-10}$$

And on the west (W) face, the pressure is expressed as in equation (2-11)below:

$$P - \frac{\partial P}{\partial x}\frac{1}{2}\delta x \tag{2-11}$$

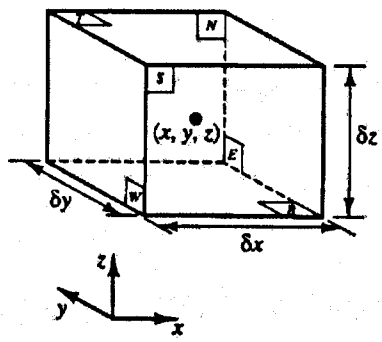

Figure 2-4: Elemental volume for CFD conservation laws

Continuity equation

The continuity equation is based on the fact that mass can neither be generated nor destroyed in a control volume provided there is no chemical reaction. By implication, this means that the material derivative of the mass in the fluid element must always be equal to zero.

$$\frac{Dm}{Dt} = \frac{\partial m}{\partial t} + (\vec{U} \cdot \nabla \mathrm{m}) = 0 \qquad (2\text{-}12)$$

This implies that, the rate of increase of mass in fluid element must be equal to the rate of mass inflow through its boundaries. With reference to Figure 2-4, the rate of increase of mass in the fluid element is

$$\frac{\partial}{\partial t}(\rho \delta x \delta y \delta z) = \frac{\partial \rho}{\partial t}\,\delta \mathrm{v} \qquad (2\text{-}13)$$

And the net rate of mass inflow through the boundaries of the volume element is:

$$\left(\rho u - \frac{\partial(\rho u)}{\partial x}\frac{1}{2}\delta x\right)\delta y \delta z - \left(\rho u + \frac{\partial(\rho u)}{\partial x}\frac{1}{2}\delta x\right)\delta y \delta z$$

$$+ \left(\rho \mathrm{v} - \frac{\partial(\rho \mathrm{v})}{\partial y}\frac{1}{2}\delta y\right)\delta x \delta z - \left(\rho \mathrm{v} + \frac{\partial(\rho \mathrm{v})}{\partial y}\frac{1}{2}\delta y\right)\delta x \delta z$$

$$+ \left(\rho w - \frac{\partial(\rho w)}{\partial z}\frac{1}{2}\delta z\right)\delta x \delta y - \left(\rho w + \frac{\partial(\rho w)}{\partial z}\frac{1}{2}\delta z\right)\delta x \delta y \qquad (2\text{-}14)$$

Substituting equations (2-13) and (2-14) into equation (2-12)and gives the continuity equation:

$$\frac{\partial \rho}{\partial t} + \nabla \cdot \left(\rho \vec{U}\right) = 0 \tag{2-15}$$

Momentum equation

Momentum conservation is obtained by the application of Newton's second law of motion to an elemental fluid. Simply put, conservation of momentum means that the rate of change of momentum of the fluid element must be equal to the net force acting on it. This leads to the following formulation for a fluid element:

$$m\frac{D\vec{U}}{Dt} = F_s + F_b \tag{2-16}$$

In Equation (2-16) the forces acting on the fluid element has been decomposed into surface forces (F_s) and body forces (F_b).The former are defined at the boundaries of the elemental volume and includes pressure (i.e. the hydrostatic part of the stress tensor) and viscous stresses (the deviatoric part of the stress tensor), while the latter (body forces) are defined on the control volume itself and can include buoyancy forces.

To obtain the momentum equation for the x-direction, one needs to balance the forces acting on surfaces and then include the effect of body forces as source term[32]. In this approach, the pressure which is a normal force is denoted as P and the viscous stresses which are tangential forces are denoted by $\tau_{ij}$where the subscripts shows that the stress acts in the j-direction on a surface normal to i-direction as shown in Figure 2-5

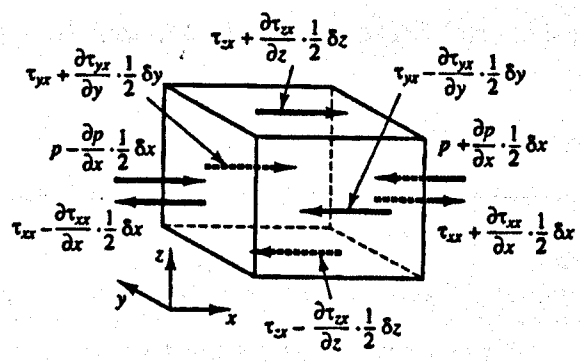

Figure 2-5: Control volume showing components of stress in the x-direction

A balance of the surface forces on the control volume in the x-direction leads to:

$$F_{sx} = \frac{\partial(-P + \tau_{xx})}{\partial x} + \frac{\partial \tau_{yx}}{\partial y} + \frac{\partial \tau_{zx}}{\partial z} \tag{2-17}$$

So far, only surface forces have been considered, the effect of body forces is commonly incorporated as a source term F_{bx} giving a more comprehensive net force in the x-direction expressed as:

$$F_{sx} = \frac{\partial(-P + \tau_{xx})}{\partial x} + \frac{\partial \tau_{yx}}{\partial y} + \frac{\partial \tau_{zx}}{\partial z} + F_{bx} \tag{2-18}$$

Substituting equation (2-18) into (2-16) and casting in a conservative form gives the x-component of the momentum i.e. equation (2-19).By adopting the same procedure as in x-momentum, the components of momentum in the y-direction and z-direction can be easily obtained as expressed by equation (2-20) and equation (2-21):

$$\frac{\partial \rho u}{\partial t} + \nabla \cdot (\rho u \vec{U}) = \frac{\partial(-P + \tau_{xx})}{\partial x} + \frac{\partial \tau_{yx}}{\partial y} + \frac{\partial \tau_{zx}}{\partial z} + F_{bx} \tag{2-19}$$

$$\frac{\partial \rho v}{\partial t} + \nabla \cdot (\rho v \vec{U}) = \frac{\partial \tau_{xy}}{\partial x} + \frac{\partial(-P + \tau_{yy})}{\partial y} + \frac{\partial \tau_{zy}}{\partial z} + F_{by} \tag{2-20}$$

$$\frac{\partial \rho w}{\partial t} + \nabla \cdot (\rho w \vec{U}) = \frac{\partial \tau_{xz}}{\partial x} + \frac{\partial \tau_{yz}}{\partial y} + \frac{\partial(-P + \tau_{yy})}{\partial z} + F_{bz} \tag{2-21}$$

The source terms (F_{bx}, $F_{by}$and F_{bz}) are the contributions due to body forces only. In heavy gas dispersion problems, the body force due to gravity is important and can be modelled as$F_{bz} = \rho g_i$ and zero in other directions.

Energy equation

The energy equation is a direct result of the first law of thermodynamics which states that energy can only be transferred from one region to another but can neither be created nor destroyed, meaning that energy is always conserved. In Fluid dynamics, energy conservation is satisfied by ensuring that the rate of change of energy of a fluid element equals the sum of the net heat supplied to the elemental fluid and the work done on it:

$$m\frac{DE}{Dt} = \dot{Q} + W \tag{2-22}$$

To obtain the energy equation in a form suitable for fluid dynamics problems, the heat addition and work done on the fluid particle has to be determined in terms of more physical parameters such as enthalpy or temperature. Referring to Figure 2-6, the net rate of heat addition to the fluid element due to heat flow in the x-direction can be expressed as:

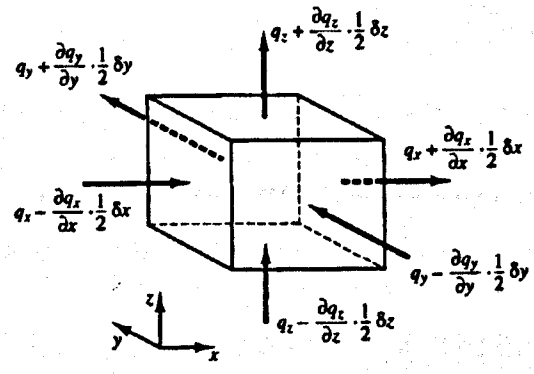

Figure 2-6: heat flux components in all three directions

$$\left[\left(q_x + \frac{\partial q_x}{\partial x}\frac{1}{2}\delta x\right) - \left(q_x - \frac{\partial q_x}{\partial x}\frac{1}{2}\delta x\right)\right]\delta y\delta z = -\frac{\partial q_x}{\partial x}\delta x\delta y\delta z \tag{2-23}$$

In the same manner, the contributions from the y-direction and z-direction can be included to obtain the rate of heat addition per unit volume of the fluid particle as;

$$-\frac{\partial q_x}{\partial x} - \frac{\partial q_y}{\partial y} - \frac{\partial q_z}{\partial z} = -\nabla \cdot \vec{q} \tag{2-24}$$

With $\vec{q}$ being a function of temperature gradient based on Fourier's law with the negative sign showing that heat flows in the direction of decreasing temperature gradient ($\vec{q} = -K\nabla T$), giving finally

$$\dot{Q} = \nabla \cdot (K\nabla T)\delta x\delta y\delta z \tag{2-25}$$

The net rate of work done on the fluid element due to surface forces acting in the x-direction can be expressed as

$$W_x = \left[\frac{\partial(u(-P + \tau_{xx}))}{\partial x} + \frac{\partial(u\tau_{yx})}{\partial y} + \frac{\partial(u\tau_{zx})}{\partial z}\right]\delta x\delta y\delta z \qquad (2\text{-}26)$$

Rate of work done in other directions follows the same structure as equation (2-26) so that the net work on the control volume, given as:

$$W = \left[-\nabla \cdot (Pu) + \frac{\partial \tau_{ij} U_i}{\partial x_j}\right]\delta x\delta y\delta z \qquad (2\text{-}27)$$

Substituting equations(2-27) and (2-25) into (2-22)and including the rate of work done by body forces as a source term (S_E) results in the final form of the energy equation:

$$\frac{\partial \rho E}{\partial t} + \nabla \cdot (\rho E\vec{U}) = -\nabla \cdot (P\vec{U}) + \frac{\partial \tau_{ij} U_i}{\partial x_j} + \nabla \cdot (K\nabla T) + S_E \qquad (2\text{-}28)$$

For compressible flows, it is more appropriate to express energy equation in terms of total enthalpy such that pressure energy can be easily included, such that

$$h_0 = E + \frac{P}{\rho} \qquad (2\text{-}29)$$

By using equation (2-29) , the energy equation (2-28)can be expressed in terms of total enthalpy as follows:

$$\frac{\partial \rho h_0}{\partial t} + \nabla \cdot (\rho h_0 \vec{U}) = \frac{\partial P}{\partial t} + \frac{\partial \tau_{ij} U_i}{\partial x_j} + \nabla \cdot (K\nabla T) + S_{h0} \qquad (2\text{-}30)$$

Where $\frac{\partial \tau_{ij} U_i}{\partial x_j}$ is the viscous dissipation term which has been neglected as it is usually small. Also, sensible enthalpy is used instead of the total enthalpy as there is no chemical reaction so the heat of formation is justifiably dropped.

Species conservation equation

On the same basis of conservation, one can write transport equation for each chemical species involved in the system by taking into account the time rate of increase of the chemical specie in the elemental volume as well as the rate at which chemical species enter and exit the surfaces of the control volume. Species conservation is of immense importance in LNG vapour dispersion as it provides the concentration field which is a key parameter in risk assessment of accidental spills of LNG. If Y_k denote the mass fractions of the chemical species, such that Y_1 is the mass

fraction of a particular chemical specie. The conservation of Y_1 in the presence of a velocity field $\vec{U}$ is expressed as [33]:

$$\frac{\partial \rho Y_1}{\partial t} + \nabla \cdot \left(\rho Y_1 \vec{U} + J_1\right) = \mathrm{R} \qquad (2\text{-}31)$$

Here, the first term stands for the rate of the change of the mass fraction of the chemical specie per unit of the control volume. The term $\rho Y_1 \vec{U}$ is the convective flux through the faces of the control volume as explained earlier, J_1 is the diffusive flux resulting from the gradients of mass fractions in the flow field. Therefore, the divergence of the two fluxes (convection and diffusion) forms the second term of the conservation equation (2-31).The term appearing on the right hand side (R) is the rate of species generation or destruction due to chemical reaction. For LNG dispersion process, there is no chemical reaction so that the reaction term can be justifiably neglected.

Neglecting the chemical reaction term and expressing the diffusion term in terms of concentration gradient, equation (2-31)can then be expressed as:

$$\frac{\partial \rho Y_1}{\partial t} + \nabla \cdot \left(\rho Y_1 \vec{U}\right) = \nabla \cdot \left(\rho D \nabla Y_1\right) \qquad (2\text{-}32)$$

The generalised species conservation for an arbitrary number of chemical species can then be written in a compact form as:

$$\frac{\partial \rho Y_K}{\partial t} + \nabla \cdot \left(\rho Y_k \vec{U}\right) = \nabla \cdot \left(\rho D \nabla Y_k\right), \quad \text{where } \mathrm{k} = 1 \ldots\ldots \mathrm{N} \qquad (2\text{-}33)$$

With N representing the total number of species in the LNG vapour-air mixture

Simplified form of the Equations

The conservation equations for continuity, momentum, energy and chemical species can be further simplified for the case of LNG vapour dispersion simulation through the application of appropriate constitutive relations. First, the vapour can be considered as an ideal gas such that it follows the ideal gas constitutive relation widely known as the equation of state:

$$P = \rho R T \qquad (2\text{-}34)$$

The second constitutive relation concerns the characterisation of the viscous stresses. LNG vapour dispersion process is considered as a Newtonian flow which means that

the viscous stresses can be modelled using a constitutive relation analogous to Hooke's law. Thus, the viscous stresses relates linearly to the velocity gradients through the dynamic viscosity as follows:

$$\tau_{ij} = \mu \left(\frac{\partial U_i}{\partial x_j} + \frac{\partial U_j}{\partial x_i} \right) \tag{2-35}$$

And the last set of constitutive relations expresses the temperature and pressure dependence of the thermophysical properties of the fluid. In particular, enthalpy, dynamic viscosity and thermal diffusivities are strongly dependent on the temperature. This is of major importance in LNG dispersion where sharp gradients in temperature exist. The enthalpy relates to the specific heat capacity through the temperature gradient:

$$\nabla h = C_p \nabla T \tag{2-36}$$

The specific heat at constant pressure C_p itself is afunction of temperature as follows:

$$C_p = R \left(\sum_{0}^{4} a_i T^i \right) \tag{2-37}$$

Equation (2-37) is commonly adopted to evaluate the specific heat capacity of gases at constant pressure. It involves a number of coefficients, a_i whose values are obtained by curve-fitting (to polynomial) the thermodynamic data compiled by NIST in what is generally called the JANAF tables [34]. OpenFOAM uses a set of 14 coefficients for each gas. This is specified in two sets where the first 7 are used for high temperature conditions above a cut-off temperature usually 1000K and the second set is used at temperatures below this cut-off temperature. For the calculation of, C_p, only the first five coefficients of each set are used. The remaining coefficients ($a_5$anda_6) are used for the calculation of enthalpy and entropy.

Dynamic viscosity is calculated based on Sutherland correlation [35] as a function of temperature, Sutherland coefficient, A_s and Sutherland temperature, T_s via:

$$\mu = \frac{A_s \sqrt{T}}{1 + \frac{T_s}{T}} \tag{2-38}$$

The values of the Sutherland coefficients need to be specified properly in order to correctly approximate the dynamic viscosity of each gas. With the viscosity

determined, the mass diffusivity and heat diffusivity respectively can then be calculated as a function of dynamic viscosity according to:

$$D = \frac{\mu}{\rho Sc} \tag{2-39}$$

$$\alpha = \frac{\mu}{Pr} \tag{2-40}$$

The Prandtl number is related to the thermal conductivity, *K*, according to:

$$\mathrm{Pr} = \frac{\mu C_p}{K} \tag{2-41}$$

It then follows that if the value of Prandtl number is known or by assuming it to be equal to unity, the thermal conductivity *K* can be calculated using dynamic viscosity and the specific heat capacity as in the constitutive relations presented above.

Incorporating the simplifications and constitutive relations leads to the more generalised Cartesian-tensor form of governing equations in the order of continuity, momentum, sensible enthalpy and species transport:

$$\frac{\partial \rho}{\partial t} + \frac{\partial(\rho U_j)}{\partial x_j} = 0 \tag{2-42}$$

$$\frac{\partial(\rho U_i)}{\partial t} + \frac{\partial(\rho U_i U_j)}{\partial x_j} = -\frac{\partial P}{\partial x_i} + \frac{\partial}{\partial x_j}\left(\mu\left(\frac{\partial U_i}{\partial x_j} + \frac{\partial U_j}{\partial x_i}\right)\right) + F_{bz} \tag{2-43}$$

$$\frac{\partial(\rho h)}{\partial t} + \frac{\partial(\rho U_j h)}{\partial x_j} - \frac{\partial P}{\partial t} = \frac{\partial}{\partial x_j}\left(\alpha \frac{\partial h}{\partial x_j}\right) + S_E \tag{2-44}$$

$$\frac{\partial(\rho Y_k)}{\partial t} + \frac{\partial(\rho U_j Y_k)}{\partial x_j} = \frac{\partial}{\partial x_j}\left(\frac{\mu}{Sc}\frac{\partial Y_k}{\partial x_j}\right) \tag{2-45}$$

In the governing equations above, i denotes a component of velocity vector in three dimensional space, U_j is the fluid velocity in the x_j direction. P is pressure, μ is themolecular viscosity and F_{bz} is thesum of body forces acting in the fluid such as buoyancy, or Coriolis which represents the influence of earth rotation on the fluid

motion. Further, h represents the sensible enthalpy, S_E is a source term denoting the irreversible rate of enthalpy due to viscous dissipation, Y_k is the species mass fractions and D is the coefficient of mass diffusion. The subscript (k) signifies the species and takes values depending on the number of species in the LNG-air mixture.

2.3.3. Turbulence Modelling

Smooth laminar flow is possible only if fluid flows at sufficiently low velocity or on a very small scale, otherwise the flow becomes unstable such that small perturbations are magnified making the flow highly chaotic and irregular. This flow regime is generally known as turbulent. It is almost impracticable to predict the regime of flow, but estimation can be made using a non-dimensional parameter known as Reynolds number. This prescribes the relative importance of inertia and viscous forces according to:

$$Re = \frac{UL}{\nu} \tag{2-46}$$

Here, U and L are respectively a characteristic velocity and length scale associated with the flow, and ν the fluid kinematic viscosity. It is generally accepted that the transition between the two regimes occur when the Reynolds number reaches a threshold known as the critical value which depends on flow scenario .Below this Reynolds number, viscosity outweighs inertia and any perturbations are damped out. Above this threshold, small perturbations become exponentially magnified to yield large coherent structures. These structures are often referred to as vortices or eddy, since they are rotational in nature. Creation of these eddies is generally associated with regions of high shear and their characteristic size, l is of the order of the shear layer thickness[36]. The ratio of the size of the large scales and the smallest scales of motion i.e. the Kolmogorov scales, η defines the range of eddy scales active in a given turbulent flow according to:

$$\frac{l}{\eta} = Re^{3/4} \tag{2-47}$$

As can be readily seen in equation (2-47),the range of scales in a given turbulent flow is directly proportional to the Reynolds number. Therefore, for industrial and environmental flows for which Reynolds numbers are typically in the range of 10^4and10^6 , the Kolmogorov scales are about 10000 times smaller than the largest

eddies in the flow [36].In DNS, all the scales of motion must be resolved. For LNG vapour dispersion, the wide range of scales present makes resolution of the Navier-Stokes equations using Direct Numerical Simulations (DNS) currently not plausible. Two methods are currently being used for more economical computation of such flows i.e. Large Eddy Simulation (LES) and Reynolds-Averaged Navier Stokes (RANS).The application of these two methodologies to turbulent dispersion of LNG vapour is described in what follows.

2.3.3.1. Large Eddy Simulation (LES) of LNG vapour dispersion

LES employs a process generally known as 'filtering' to filter the governing equations of LNG vapour dispersion resolving eddies of length scale larger than the filter size so that only the eddies smaller than the filter size are modelled. In order to separate the large scale eddies from the small scale, LES applies a filtering operation producing a filtered variable denoted by an over bar as shown in equation(2-48).This process is better visualised as decomposition of the transport equations into two parts: the resolved part representing the large scale eddies which are solved for directly, and the sub-grid part represents the small scales whose effect on the resolved scales is included via a sub-grid scale model.

$$\bar{f}(x) = \int f\,(x')\,G\,(x,x';\,\bar{\Delta})\,d\,x' \qquad (2\text{-}48)$$

Where G denotes the filter function and $\bar{\Delta}$ denotes the filter width. Thus, all eddies of length scale less than the filter width are filtered out for modelling while eddies of other sizes are retained and resolved directly. By applying the filtering operation to the governing equations, the filtered transport equations are obtained. For low Mach number flows such as LNG vapour dispersion, the incompressible form of the filtered equations can be used, but in a form that accounts for density variation [37].Therefore the filtered equations in the order of mass conservation, momentum, species transport and energy becomes:

$$\frac{\partial \tilde{\rho}}{\partial t} + \frac{\partial(\tilde{\rho}\bar{U}_j)}{\partial x_j} = 0 \qquad (2\text{-}49)$$

$$\frac{\partial(\tilde{\rho}\bar{U}_i)}{\partial t}+\frac{\partial(\tilde{\rho}\bar{U}_i\bar{U}_j)}{\partial x_j}=-\frac{\partial\bar{P}}{\partial x_i}+\frac{\partial}{\partial x_j}\left(\mu\left(\frac{\partial\bar{U}_i}{\partial x_j}+\frac{\partial\bar{U}_j}{\partial x_i}\right)\right)+\frac{\partial(\tau_{ijSGS})}{\partial x_j}+F_{bz} \quad (2\text{-}50)$$

$$\frac{\partial(\tilde{\rho}\bar{Y}_K)}{\partial t}+\frac{\partial(\tilde{\rho}\bar{U}_j\bar{Y}_K)}{\partial x_j}=\frac{\partial}{\partial x_j}\left(\frac{\mu}{S_c}\frac{\partial\bar{Y}_K}{\partial x_j}\right)+\frac{\partial\gamma_K}{\partial x_j} \quad (2\text{-}51)$$

$$\frac{\partial(\tilde{\rho}c_p\bar{T})}{\partial t}+\frac{\partial(\bar{U}_jc_p\bar{T})}{\partial x_j}=\frac{\partial}{\partial x_j}\left(K\frac{\partial\bar{T}}{\partial x_j}\right)+\frac{\partial q_{sj}}{\partial x_j} \quad (2\text{-}52)$$

Where τ_{ijSGS} , γ_k and q_{sj} denote sub-grid scale (SGS) stresses, sub-grid scale species fluxes and sub-grid scale heat fluxes respectively. The tilde denotes Favre filtering which entails that density is variable for each time step. To close the set of equations, a closure model is usually adopted for the sub-grid terms. A number of modelling approaches exist in the literatures with the most widely used being the eddy-viscosity model in which the SGS terms are prescribed via a simplified Boussinesq approximation:

$$\tau_{ijSGS} = -2\mu_T\,\bar{S}_{ij} \quad (2\text{-}53)$$

Here $\bar{S}_{ij}=\frac{1}{2}\left(\frac{\partial\bar{U}_i}{\partial x_j}+\frac{\partial\bar{U}_j}{\partial x_i}\right)$ and μ_T are respectively the rate of strain tensor and sub-grid eddy viscosity. The sub-grid eddy viscosity can be parameterised via the filtered strain rate $\ddot{S}=\left(2\bar{S}_{ij}\bar{S}_{ij}\right)^{1/2}$ and the filter size Δ, giving the well-known Smagorinsky model as shown in equation (2-54):

$$\mu_T = l_s^{\,2}\,\ddot{S} = (C_{sm}\,\Delta)^2\ddot{S} \quad (2\text{-}54)$$

The values of the Smagorinsky coefficient, C_{sm} has to be determined and specified during problem set-up as it varies depending on flow scenario. There are currently three major versions of Smagorinsky models which differ from one another based on the formulation of the Smagorinsky coefficient. This include: (a) specifying the Smagorinsky coefficient as a constant value throughout the domain otherwise referred to as 'LES-Standard in this present study, (b) a traditional Smagorinsky coefficient closure that requires the specification of a wall damping function generally referred to as the LES-WALE, and (c) a standard closure that assumes

scale-invariance (LES-Dynamic) model. Full description of the three models is available elsewhere in[38] and [39] and will not be discussed further in this study.

Similar to the eddy viscosity model, μ_T , an eddy diffusivity α_T can be defined for the turbulent heat transport as:

$$\alpha_T = \frac{\mu_T}{Pr_T} \tag{2-55}$$

Where μ_T can be determined from equation (2-54)and $Pr_T$is the subgrid scale Prantl number. Then the subgrid scale heat fluxes can be estimated from the eddy diffusivity concept:

$$q_{sj} = \alpha_T \frac{\partial \bar{T}}{\partial x_j} \tag{2-56}$$

And the sub-grid scale specie fluxes can be determined using similar argument as applied for the turbulent heat fluxes as:

$$\gamma_k = \frac{\mu_T}{S_{cT}} \frac{\partial \bar{Y}_K}{\partial x_j} \tag{2-57}$$

Where S_{cT} is the subgrid scale turbulent Schmidt number and must be specified during simulation.

2.3.3.2. RANS modelling approach

RANS models are less computationally tasking (cheapest) compared to LES and DNS techniques and hence the most appropriate for industrial scale simulations. With this approach, the dependent variables in the governing partial differential equations are decomposed into mean and fluctuating parts in what is generally referred to as Reynolds decomposition, given as:

$$\begin{cases} u = \bar{U} + U' \\ p = \bar{p} + p' \\ h = \bar{h} + h' \end{cases} \tag{2-58}$$

Substitution (2-58) into the governing equations followed by time-averaging of the resulting partial differential equations produces the following time-averaged equations:

$$\frac{\partial \rho}{\partial t} + \frac{\partial(\rho \bar{U}_j)}{\partial x_j} = 0 \tag{2-59}$$

$$\frac{\partial(\rho \bar{U}_i)}{\partial t} + \frac{\partial(\rho \bar{U}_i \bar{U}_j)}{\partial x_j} = -\frac{\partial \bar{P}}{\partial x_i} + \frac{\partial}{\partial x_j}\left(\mu\left(\frac{\partial \bar{U}_i}{\partial x_j} + \frac{\partial \bar{U}_j}{\partial x_i}\right) - \overline{\rho U_i' U_j'}\right) + F_{bz} \tag{2-60}$$

$$\frac{\partial(\rho \bar{h})}{\partial t} + \frac{\partial(\rho \bar{U}_j \bar{h})}{\partial x_j} - \frac{\partial \bar{P}}{\partial t} = \frac{\partial}{\partial x_j}\left(\alpha \frac{\partial \bar{h}}{\partial x_j} - \overline{\rho U_j' h'}\right) + S_E \tag{2-61}$$

$$\frac{\partial(\rho \bar{Y}_k)}{\partial t} + \frac{\partial(\rho \bar{U}_j \bar{Y}_k)}{\partial x_j} = \frac{\partial}{\partial x_j}\left(\frac{\mu}{Sc}\frac{\partial \bar{Y}_k}{\partial x_j} - \overline{\rho U_j' Y_k'}\right) \tag{2-62}$$

The resulting averaged equations above are the transport equations for mean flow quantities with no approximations made. Non-linearity of the governing equations introduces the new quantities appearing in equations (2-60) to (2-62) which are the correlations between fluctuating velocities $\overline{\rho U_i' U_j'}$, another between fluctuating velocity and enthalpy $\overline{\rho U_j' h'}$ and also between fluctuating velocity and mass fraction $\overline{\rho U_j' Y_k'}$. These correlations depict the transport of momentum, heat and mass respectively, due to turbulence. The values of these turbulent quantities must be determined in order to close the averaged equations. Attempt to close the Reynolds stresses using existing transport equations results in the introduction of higher order terms into the governing equations, a condition generally referred to as the *closure problem* in the turbulence modelling community. Thus an alternate approach is required to evaluate these turbulent quantities. Boussinesq introduced the eddy viscosity concept in which it is assumed that the Reynolds stresses are proportional to the mean velocity gradients in a manner similar to viscous stresses in laminar flows[40]. The approximation due to Boussinesq is expressed as:

$$-\overline{\rho U_i' U_j'} = \mu_t\left(\frac{\partial \bar{U}_i}{\partial x_j} + \frac{\partial \bar{U}_j}{\partial x_i}\right) \tag{2-63}$$

Where μ_t denotes the turbulent (eddy) viscosity which is not actually a fluid property but is a value that depends on turbulence, hence it may vary from region to region within the flow field. Thus Boussinesq approximates the transport of turbulent momentum to be proportional to the gradient of velocity. Alike to this analogy, the turbulent heat transport is assumed to be proportional to the gradient of enthalpy:

$$-\overline{\rho U_j{}' h'} = \frac{\mu_t}{\mathrm{Pr}_t}\frac{\partial \bar{h}}{\partial x_j} \tag{2-64}$$

Also turbulent mass diffusion is prescribed by assuming it to be proportional to the gradient of mass fractions as follows:

$$-\overline{\rho U_j{}' y_k'} = \frac{\mu_t}{Sc_t}\frac{\partial \bar{Y}_k}{\partial x_j} \tag{2-65}$$

By substituting equations (2-63) to (2-65) into the time-averaged equations, the Reynolds-averaged Navier-stokes can then is obtained in a more detailed and compact form as:

$$\frac{\partial \rho}{\partial t} + \frac{\partial(\rho \bar{U}_j)}{\partial x_j} = 0 \tag{2-66}$$

$$\frac{\partial(\rho \bar{U}_i)}{\partial t} + \frac{\partial(\rho \bar{U}_i \bar{U}_j)}{\partial x_j} = -\frac{\partial \bar{P}}{\partial x_i} + \frac{\partial}{\partial x_j}\left(\mu_{eff}\left(\frac{\partial \bar{U}_i}{\partial x_j} + \frac{\partial \bar{U}_j}{\partial x_i}\right)\right) + F_{bz} \tag{2-67}$$

$$\frac{\partial(\rho \bar{h})}{\partial t} + \frac{\partial(\rho \bar{U}_j \bar{h})}{\partial x_j} - \frac{\partial \bar{P}}{\partial t} = \frac{\partial}{\partial x_j}\left(\alpha_{eff}\frac{\partial \bar{h}}{\partial x_j}\right) \tag{2-68}$$

$$\frac{\partial(\rho \bar{Y}_k)}{\partial t} + \frac{\partial(\rho \bar{U}_j \bar{Y}_k)}{\partial x_j} = \frac{\partial}{\partial x_j}\left(D_{eff}\frac{\partial \bar{Y}_k}{\partial x_j}\right) \tag{2-69}$$

Notice that due to the substitution, an effective dynamic viscosity (μ_{eff}) has been introduced which is the sum of the molecular viscosity and turbulent viscosity:

$$\mu_{eff} = \mu + \mu_t \tag{2-70}$$

The turbulent viscosity (μ_t) is calculated from transport equations as described in the next section. Alike to the dynamic viscosity, an effective thermal diffusivity (α_{eff}) has been introduced which is given as

$$\alpha_{eff} = \alpha + \frac{\mu_t}{\mathrm{Pr}_t} \tag{2-71}$$

Where Pr_t is the turbulent Prandtl number and is a function of buoyancy [38], but typical value in the range (0.85 to 1) is widely accepted. The effective mass diffusivity (D_{eff}) is:

$$D_{eff} = \frac{\mu}{\rho Sc} + \frac{\mu_t}{\rho Sc_t} \tag{2-72}$$

Where Sc_t is the turbulent Schmidt number for which typical values in the range of 0.2 and 1.3 has been used in many previous CFD studies [41].

Clearly, the turbulent dynamic viscosity μ_t is a very important parameter which must be prescribed in order to close the set of averaged equations. This is achievable through the application of a closure model. Three possibilities are currently available and are subdivided into:

- **Mixing length models** which are also called zero equation models because they do not solve an addition transport equation so that μ_t is determined from mean flow quantities and a characteristic length scale which depends on geometry.
- **One equation models** which makes use of a length scale as well, but a transport equation is required for the quantification of turbulent kinetic energy
- **Two equation models,** in which two transport equations are required, one for turbulent kinetic energy k, and another for its dissipation rate (specific ω or absolute ε) and then local values of μ_t are calculated from the values of these scalars

A fundamental limitation of mixing length models is the assumption that Reynold stresses can be parameterised based on mean flow, however turbulence does not respond immediately to changes in the mean flow but rather adjusts over a time scale typical of the turbulent structure [42].For, one equation models, even though the influence of fluctuating properties are felt through the turbulent kinetic energy, they

still depend on the geometry through the definition of a characteristic length scale. Thus, the first category of models in order of complexity which do not depend on the definition of characteristic length, is the two equation family of models. This property of two equation models is of fundamental importance in predicting many types of flows including recirculation flows. In fact, mixing length is generally inappropriate for flows in which convection and diffusion are important [42].

Existing two equation models can be subdivided into two categories: the k-ε family and k-ω family of models, each having specific pros and cons. Therefore, an informed choice has to be made, usually as a compromise between suitability (area of application) and feasibility (computational cost).For instance, the k-ω model is widely known to perform well in wall bounded flows. In particular, it is a low Reynolds number formulation which is in fact suitable for simulation of flows in the near-ground region, hence it appears to be suitable for simulation of dense gas dispersion including LNG vapour. However, the use of k-ω require fine grid near the walls ($y^+ \approx 1$). This strict constraint combined with the requirement for a reasonably good aspect ratio will produce an incredibly enormous number of cells in large domains such as those required for LNG dispersion simulation. A step forward therefore would be to use a high Reynolds number turbulent model (k-ε model) which permits higher values of y^+ and then apply wall treatment to bridge the near-wall region. This is a very popular two equation turbulence closure approach and will be used in this study as described in the section that follows.

Standard k-ε model

Boussinesq approximation does not overcome the difficulty of modelling turbulent flow field but it does reduce the problem to one of determining the value of eddy viscosity. The k-ε model assumes that the turbulent viscosity is linked to the turbulent kinetic energy and the dissipation rate through the relation

$$\mu_t = \frac{c_\mu \rho k^2}{\varepsilon} \tag{2-73}$$

Instantaneous values of k and ε are obtained from transport equation for turbulent kinetic energy and its dissipation rate as follows:

$$\frac{\partial \rho k}{\partial t} + \frac{\partial(\rho u_i k)}{\partial x_i} = \frac{\partial}{\partial x_i}\left[\left(\mu + \frac{\mu_t}{\sigma_k}\right)\frac{\partial k}{\partial x_i}\right] + G_k - \rho\varepsilon \tag{2-74}$$

$$\frac{\partial \rho \varepsilon}{\partial t} + \frac{\partial(\rho u_i \varepsilon)}{\partial x_i} = \frac{\partial}{\partial x_i}\left[\left(\mu + \frac{\mu_t}{\sigma_\varepsilon}\right)\frac{\partial \varepsilon}{\partial x_i}\right] + c_{\varepsilon 1}\frac{\varepsilon}{k}(G_k) - c_{\varepsilon 2}\,\rho\,\frac{\varepsilon^2}{k} \tag{2-75}$$

$$G_k = \frac{\partial u_i}{\partial x_i}\left(\mu_t\left(\frac{\partial u_j}{\partial x_i} + \frac{\partial u_i}{\partial x_j}\right) - \frac{2}{3}(\rho k \delta_{ij})\right) \tag{2-76}$$

Where G_k denotes the turbulent kinetic energy generation or destruction due to mechanical shear. Default values for the k-ε model constants are well reported in the literatures[43, 44] and are the following:

Table 2-1: Standard k-εmodel constants

c_μ	$c_{\varepsilon 1}$	$c_{\varepsilon 2}$	σ_k	σ_ε
0.09	1.44	1.92	1.3	1.0

The values presented in the table above have been found to perform satisfactorily in a number of turbulent flow situations, but it is worthwhile to mention here that they were derived for neutral ABL condition i.e. when there is no vertical temperature gradient in the ABL [45]. Based on this fact, Alinot and Masson[45] reported alternative values for stable and unstable atmospheric conditions. These modifications will be duly applied in all simulations carried out in the present study. Notice that the standard k-ε model as presented in equations (2-74) and (2-75) does not include the buoyancy term which accounts for the effect of buoyancy on turbulence generation and destruction. The buoyancy term can be of key importance in LNG vapour dispersion simulation. In Ansys CFX, buoyancy term is included in the turbulent kinetic energy equation by setting the buoyancy turbulence option to 'production' during simulation set-up. It is also included in the energy dissipation equation if the option is set to 'production and dissipation. Considering that OpenFOAM includes the k-ε model in its standard form as one of the two equation models, in the present study a buoyancy term is added to the standard k-ε model in OpenFOAM. The implementation is described in the model development section (Chapter 3)

As earlier mentioned, k-ε model is a high Reynolds number turbulence closure model that must be complemented with a wall function for better treatment of the near-ground region. The main effects of the ground are two folds: (1) increasing the generation of turbulent kinetic energy through shear and (2) abrupt damping out of fluid velocity components by forcing a no-slip condition. The former is overcome through addition of a source term (G_k)to the transport equation for the turbulent kinetic (G_k) as described in the previous section, but the later demands high grid resolution down to the ground to accurately capture the associated sharp gradients in flow quantities. This standard method of applying very fine mesh close to the wall is called integration method and generally necessitates an LNR (low Reynolds Number) type of turbulence model. At higher Reynolds number, the region under the influence of the ground diminishes. However, there is still need to fully resolve flow gradients in the near-wall region using high mesh density. For a fully three dimensional flow, this becomes non feasible and a function that bridge near wall flow profiles is instead introduced. This latter method is referred to as *wall function* approach which employs an HRN (high Reynolds Number) turbulence model[46]. The k-ε model in its standard form is a high Reynolds formulation that must be used together with a wall function. By so doing the flow quantities are assumed to have a known profile in the near-wall region, hence the transport equations are not discretised in this region.

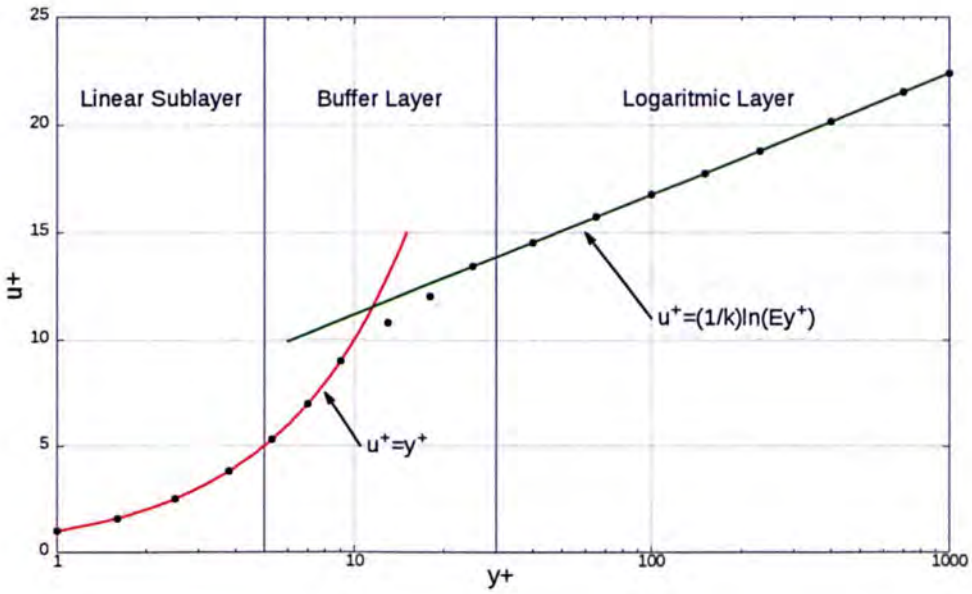

Figure 2-7: Law of the wall for smooth surfaces

From an engineering standpoint, the near-ground region is commonly subdivided into three distinct layers, comprising of a viscous layer where flow Reynolds number is very low as viscosity dominates, a buffer layer which marks transition from laminar to turbulent regime and a logarithmic outer layer where flow is dominantly turbulent (Figure 2-7).The buffer layer serves as a transition regime between the viscous sub-layer and the logarithmic layer as shown in figure above. Currently there exists no conventional method to apply a turbulence model, with the first node positioned in the buffer layer. Rather than attempt to model the buffer layer, the general practise is to locate the first central node in the viscous sub-layer (LRN model) or in the logarithmic layer (HRN) model. Thus, a low Reynolds number turbulence model is considered appropriate for the former approach and a high Reynolds number turbulence model such as the k-ε range of models will be appropriate for the later. This present study will employ the k-ε model and wall functions available in OpenFOAM. The standard wall function used in many CFD packages are based on Launder and Spalding [44].When k-ε model is used in OpenFOAM, the first central node needs to be located in logarithmic region considering that k-ε model is designed for HRN flows. By employing a grid where the first interior node is located in the logarithmic region, the logarithmic law is directly applied to the first interior nodes as boundary conditions

One form of the logarithmic law implemented in OpenFOAM is as shown in Figure 2-7 above and reproduced below:

$$U^{+} = \frac{1}{K_{\mathrm{v}}} \ln \mathrm{E} y^{+} \tag{2-77}$$

Where the velocity and vertical positions have been made dimensionless using friction velocity and coefficient of kinematic viscosity, y^{+} is evaluate as follows:

$$y^{+} = y \, \frac{\rho C_{\mu}^{1/4} k^{1/2}}{\mu} \tag{2-78}$$

$$U^{+} = \frac{U}{u_{*}} \tag{2-79}$$

The friction velocity is a function of the local density and wall shear stress (τ_{wall}):

$$u_* = \sqrt{\frac{\tau_{wall}}{\rho}} \qquad 2\text{-}80$$

And K_v is the Von Kaman constant which equals 0.42, E is a wall function coefficient which is set to a default value of 9.8 in OpenFOAM for smooth walls. The turbulent kinetic energy transport equation is solved all the way to the walls and its dissipation rate is calculated using the formula:

$$\varepsilon = \frac{C_\mu^{3/4} k^{3/2}}{yk} \qquad (2\text{-}81)$$

The coefficient of turbulent viscosity is then recalculated using the following formulation:

$$\mu_t = \mu\left(\frac{yk}{\ln(Ey^+)} - 1\right) \qquad (2\text{-}82)$$

Equations (2-77) is used as long as $y^+$is greater than y_l which is the y^+ value at which the logarithmic and larminar graphs cross each other. In theversion of OpenFOAM used for this study, y_l is set equal to 11 while in Fluent, it is set to 11.225.Outside this region, $u^+ = y^+$ is used. The wall function equations presented so far are designed for smooth ground and are therefore inadequate for modelling LNG dispersion in real life scenario. Blocken et al [47] were the first to report this problem attributing it to the difficulty in obtaining fully developed wind profile in the atmospheric boundary layer. In their exact words, a typical ABL problem domain consists of (1) a central region where obstacles (buildings, trees, stacks) are modelled explicitly with their geometrical shape and (2) upstream and downstream region where obstacles are modelled implicitly i.e. their effects are included as roughness elements, e.g. by means of wall functions applied to the bottom of the domain. These wall functions must be formulated such that they have the same overall effect on the flow field as the obstacles being represented. This roughness is commonly expressed in form of aerodynamic roughness length (z_0) or, less often in form of equivalent sand-grain roughness height (k_s). In OpenFOAM, roughness is prescribed by two

variables: the roughness height k_s and the roughness constant C_s. Typical values of roughness height for different types of surfaces are reported in Wieringa [48] and as for the roughness constant, there is no general guidance value, although values in the range of 0.5 -1 are recommended in ANSYS Fluent user guide [49]for nonuniform sand-grains, ribs, and wire-mesh roughness, but acknowledged there is no general rule. The implemented functions accounting for roughness in the present study are the following:

$$u^+ = \frac{1}{k}\ln(\mathrm{E}y^+) \; - \; \Delta B \tag{2-83}$$

Where ΔB depends on the type and size of roughness and is usually computed based on the curve fit of Cebeci and Bradshaw[50] to the sand-grain data of Nikuradse [51], wherein roughness is categorised into three regimes. In order to define the regimes, a dimensionless roughness height is defined, such that:

$$K_s^+ = \frac{\rho k_s c_\mu^{1/4} k^{1/2}}{\mu} \tag{2-84}$$

For smooth walls $(K_s^+ < 2.5)$, ΔB is set to zero. Otherwise if $(K_s^+ > 90)$ it is modelled as follows:

$$\Delta B = \frac{1}{k}\ln(1 + \; C_s K_s^+) \tag{2-85}$$

And in the intermediate level of roughness where the range is $(2.5 < K_s^+ < 90)$

$$\Delta B = \frac{1}{k}\ln\left[\frac{K_s^+ - 2.25}{87.75} + C_s K_s^+\right]\sin\{0.4258\,(\ln K_s^+ - 0.811)\} \tag{2-86}$$

2.3.4. Numerical Technique

A close look at the PDE's governing LNG vapour dispersion as presented in the previous sections readily reveals that they are coupled and highly non-linear. Thus, these equations do not have analytical solution, even for the simplest flow scenario. Fortunately, a numerical solution can be sought; an approach that is commonly referred to as Computational Fluid Dynamics.

CFD aims to convert the coupled non-linear PDE's governing fluid motion into a set of discrete algebraic equations. The solution of these discretised equations then becomes the result of the original partial differential equations at a number of locations and time within the computational domain. Based on the foregoing, it is clear that the discretisation process comprises of two basic steps: first is to discretise the computational domain into a number of cells called control volumes whose centres represent the pre-defined locations and secondly to discretise the governing partial differential equations to obtain the set of discrete algebraic equations, one for each pre-defined control volume centre. There currently exist three main methods for discretising the governing equations. These comprise of the finite difference, finite element and finite volume methods.

A finite difference method linearizes the PDE's using truncated Taylor series expansion. The main advantage of this scheme is that it can achieve order accuracy higher than second order. But this is usually at the expense of conservation of flow quantities. Moreover, the finite difference scheme can only be used with structured grids.

Finite volume method discretises the domain into a set of non-overlapping polyhedral control volumes. At the centre of each of these volumes, a node is positioned. These set of nodes form the selected points at which the values of flow quantities are sought [52] and interpolation scheme is employed to obtain cell face values. Since the integral of quantities a face shared by any two neighbouring cells are the same, this scheme benefits from being conservative.

The finite element method is very similar to finite volume method, save that certain functions known as weight functions have to be evaluated at cell corners. These functions are used during integration to help minimise residuals. But, this approach results to matrices for which an efficient solution may be difficult.

In this work, OpenFOAM which is inherently a finite volume CFD code has been employed to seek the solution of the governing equations.

The term finite volume discretization in CFD entails approximation of continuum equations, such as the governing equations presented, into discrete form thereby making them suitable for numerical implementation on digital computers. This is the solution technique underlying OpenFOAM and most CFD software packages, including Fluent, CFX, and Star-CD etc. For the purpose of demonstration of how the finite volume discretization technique has been applied to the governing equations of LNG dispersion, we hereby define a generic variable such that the transport equations can be replaced here with a single equation representing the transport of a generic quantity ϕ :

$$\frac{\partial \rho \phi}{\partial t} + \frac{\partial \rho \phi u_i}{\partial x_i} = \frac{\partial}{\partial x_i}\left(\Gamma \frac{\partial \phi}{\partial x_i}\right) + S_\phi \qquad (2\text{-}87)$$

Where Γ represent the coefficient of turbulent diffusion and S_ϕ a source term. The four terms in the general transport equation represent the transient term, the covective term, the diffusion term and the source term. Notice that equation (2-87) transforms to our governing equations for different values of ϕ (1, u, v, w, h, Y_k, k, and ε). Now, we need to concern ourselves with the discretization of only the generalized equation. This has the benefit of allowing the construction of a generic computer code for equation (2-87) , which can be used repeatedly for the different meanings of ϕ .Thus, the idea of generalization is a time-saving approach.

The diffusion coefficient and source term must be defined such that their meaning derives from the variable being solved for. For instance, in the equation for enthalpy, the diffusion depicts the heat diffusion between control volumes whereas in the species transport equation it transforms to the coefficient of mass diffusion. Note also that to cast the governing equations in the general form involves manipulating the transport equation for each quantity until all the terms i.e. the transient term, the convective term and the diffusive term conforms to the generic form. The coefficient of the gradient ($\frac{\partial \phi}{\partial x_j}$) in the diffusion term then becomes the expression for Γ and all the remaining terms on the right hand side, except the pressure terms, form a lumped parameter representing the source term, S_ϕ .The pressure field is calculated in a predictor-corrector procedure via the equation of state or a separate pressure equation (Poisson equation) for incompressible flows. Considering that I-PSED is a density-based model, the ideal gas equation of state has been used in the present study.

2.3.4.1. Domain and time discretisation

The dependent variable ϕ would, as a matter of fact be a function of space coordinates and time. In three dimensions,

$$\phi = \phi(x, y, z, t) \tag{2-88}$$

Equation (2-88) shows that the numerical solution for the independent variable is a function of independent variables (x, y, z, t) which specify the locations at which solution is sought. The set of coordinates defines the control volumes (cells) involved in the solution process. The cells can be of any shape, as in Figure 2-8 , since only the coordinates of the centre, corners, and faces are required as input from which the numerical algorithm determines the shape, volume and location of the cell. There exist certain codes that can only use structured mesh (e.g. cubic cells) but the OpenFOAM code which has been applied for this study does not have this limitation.

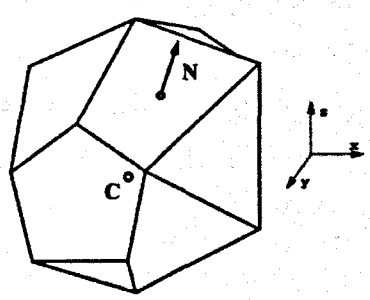

Figure 2-8:A random-shaped computational cell [53]

In the general control volume shown in Figure 2-8, the cell centre is depicted by point C and surfaces are shared with neighbouring cells, except for any face that lies on the domain boundaries. The unit normal vector to one of the faces is denoted by N.

2.3.4.2. Equation discretisation

The basic principle behind the equation discretisation using finite volume method is to integrate the transport equation over the control volumes and over time. Integrating (2-88)over a three dimensional control volume V_p and time t:

$$\int_{t}^{t+\Delta t}\left[\int \frac{\partial \rho\phi}{\partial t}\mathrm{dv} + \int \frac{\partial \rho\phi u_i}{\partial x_j}\mathrm{dv}\right]\mathrm{dt} = \int_{t}^{t+\Delta t}\left[\int \frac{\partial}{\partial x_i}\left(\Gamma\frac{\partial \phi}{\partial x_j}\right)\mathrm{dv} + \int S_\phi \ \mathrm{dv}\right]\mathrm{dt} \tag{2-89}$$

Applying Gauss's divergence theorem to the spatial derivatives in equation ((2-89) and rearranging gives:

$$\int_{t}^{t+\Delta t}\left[\int \frac{\partial \rho\phi}{\partial t}\mathrm{dv} + \int (\rho\phi u_i)\cdot \boldsymbol{n}\,\mathrm{ds}\right]\mathrm{dt} - \int_{t}^{t+\Delta t}\left[\int \left(\Gamma\frac{\partial \phi}{\partial x_j}\right)\cdot \boldsymbol{n}\,\mathrm{ds} - \int S_\phi \ \mathrm{dv}\right]\mathrm{dt} = 0 \tag{2-90}$$

Where **n** is the unit normal vector to the surface of the control volume. Equation (2-90) is the basis for the formulation of finite volume method. Choosing appropriate schemes, the volume integrals can be approximated. The integration process otherwise known as discretization is a well-known procedure and hence will not be described in this section; rather it has been included in Appendix A.

The discretization process requires that the values of the fluxes must be obtained at the cell faces, hence interpolation schemes are normally employed for this process. A number of interpolation techniques have been adopted in the CFD modelling community ranging from the central differencing scheme to the upwind scheme, the blended schemes and other high order schemes such as QUICK. These schemes are normally grouped into two: (1) first order and (2) higher order schemes based on the truncation error resulting from the Taylor's series from which they are derived. Higher order schemes such as central differencing are more accurate than lower order schemes (Upwinding) and are usually selected to seek better solution accuracy. However, spurious oscillations occur around discontinuities in every high order schemes which is unacceptable [54]. In this present study which involves the injection of a low temperature LNG vapour into a relatively high temperature ambient environment, discontinuities (sharp gradients in temperature) is expected around the cloud front as it mixes with the ambient wind and has to be handled in some sense. A successful method of avoiding any oscillation under this condition is

through the use of slope (flux) limiter function. The essence of the flux/slope limiter function is to modify the gradients only when there is need to prevent oscillation. This means that if a flux limiter is applied for instance to a central difference scheme, it preserves the second order nature of the scheme in the region where variation is smooth, while it intervenes where there is jump by modifying the gradient. Numerical schemes that are capable of exhibiting such classical behavioural pattern are said to be total variation diminishing (TVD).

Total variation diminishing (TVD) method

To measure the level of oscillations, the total variation (TV) of the solution is first defined:

$$TV(\phi^n) = \sum_f |\phi_N^n - \phi_P^n| \tag{2-91}$$

Here, P and N denote the node points in the neighbourhood of the face *f*. It then follows that if the RHS of equation (2-91) is constant, then the total variation will be constant as long as the function is monotonic. But, if the values of ϕ develop local maxima or minima, then$TV(\phi)$ increases by virtue of the absolute value in equation (2-91).This increase therefore represents a measure of the oscillations in the solution. Therefore a numerical scheme is referred to as total variation diminishing (TVD) if and only if:

$$TV(\phi^{n+1}) \leq TV(\phi^n) \tag{2-92}$$

Clearly, such a numerical scheme will not produce oscillations near discontinuities considering that oscillation is a monotonically decreasing/increasing function and a TVD scheme will never increase the total variation. It was Harten [55] who proposed that a good recipe for the construction of an oscillation-free second order scheme is to constrain the scheme such that the total variation of the solution should not increase. This led to the development of certain higher order schemes, including one developed by Jasak [56] as the sum of a first order scheme and a limited higher order correction:

$$\phi_f = (\phi)_{LO} + \Psi(r)[(\phi)_{HO} - (\phi)_{LO}] \quad (2\text{-}93)$$

Where the subscripts LO and HO means lower order and higher order respectively, $\Psi(r)$ is a flux limiter and is evaluated from gradient in flow properties (r).The limiter functions are constructed such that equation (2-93) satisfies (2-92). Notice that if the limiter function is zero, the scheme is first order which is oscillation free, while if it is unity, the scheme is higher order. Thus, the flux limiter is a non-linear function that ensures the scheme is oscillation free in the regions of discontinuity by manipulating the gradient. A number of limiters have been proposed in the literatures and are all implemented in OpenFOAM. Examples include those proposed by Van Leer[57], Superbee [58], Van Albada [59] and Sweby [60]. For this present study, the Sweby limiter option has been used for all convective terms. More details about the Sweby's limiter function as well as other limiters are available in the literatures[56, 60].

2.4. Boundary conditions

Division of the computational domain into discrete cells will as a matter of fact place some of the cell faces at the domain boundaries. These faces do not host any shared interface with any other control volume so that the convective and diffusive terms will depend on the values at the centroid of the neighbouring cells, hence certain values (boundary condition) are imposed on these boundary cells during problem set up and special treatments are needed to pass boundary values to associated cells and keep the required data set complete. The provided boundary information (value) must be a true representation of the physical behaviour of the system or at least a very close approximation for the problem to be well-posed. On a general level, the boundary conditions are categorised as either numerical or physical. Numerical boundary conditions are of two types; the first type specifies boundary values directly and is referred to as Dirichlet boundary condition. The second type specifies the gradient of variables at the boundaries and is known as the Von-Neumann boundary condition. The Dirichlet condition is straightforward to use in discretised equations because the value is given whereas in Von-Neumann only the gradient is given and must be integrated over a half of the first computational cell at the vicinity of the boundary[33].

The physical boundary conditions depict the physical condition of the system such as inlet, wall, outlet symmetry plane etc. In all CFD toolbox, both commercial and open-source, there exists a connection between these physical boundaries and the numerical ones previously described as the selection of any physical boundary instructs a CFD tool to apply certain numerical conditions.

Here some most widely used physical boundary conditions are briefly explained:

Wall/non-slip boundary

The wall boundary condition imposes fixed value for the velocity (zero) and fixed gradient for the pressure at the wall surface. The physical basis of the zero velocity is to restrict any relative motion between the fluid and the wall surface which is exactly the case from a physical point of view. Also, the wall surface is impermeable so there would be no flux passing through the wall, hence a fixed pressure gradient of zero. For LNG vapour dispersion, the ground surface must be specified as wall with some level of roughness depending on terrain

Inlet boundary

The inlet boundaries introduce flow into the computational domain. They are normally constructed on the basis of a prior knowledge of flow velocity at the inlet. Thus, it is a Dirichlet type condition and requires that fixed velocity at the inlet will be imposed and this must be used with a zero gradient pressure condition in order to keep physical consistency. For LNG vapour dispersion simulation, inlet boundary condition must be used at the incoming wind boundary and at the boundary representing gas inflow.

Outlet boundary

For the outlet boundary condition it becomes very important to make adjustments so that maintain a constant total mass in the system. One way to achieve this condition is by adjusting the velocity of the outgoing flow. This adjustment should guarantee the mass conservation in the system, while the pressure is maintained at zero gradient condition. But, this may introduce instabilities leading to the occurrence of backflows at the outlet boundary. A more convenient approach for specifying the outlet boundary condition is using a fixed value pressure at the outlet; this condition, in most practical cases, is a physically valid assumption which means that the flow pressure right at the outlet would be equal to the ambient pressure. A zero gradient condition would be applied to the velocity in this case and the pressure Equation

enforces the conservation of total mass for the system. For LNG vapour dispersion, an outlet type boundary condition would be appropriate at all enclosing surfaces apart from the wall i.e. the downwind boundary, the top boundary and the sides.

Symmetry plane boundary

This type of boundary condition is applied in cases where there exists a plane of symmetry in the geometry. It acts like a mirror and hence models only half of the domain and maps the result to the other half in a process that can be best described as reflection. For LNG dispersion modelling, this type of boundary condition will be appropriate for the side boundaries if there is no wind angle. This will go a long way to reduce the computational cost while maintaining solution accuracy. However, if wind angle is used, the side boundaries cannot be considered as planes of symmetry. In such a situation, an outlet boundary condition will be more appropriate.

2.4.1. Wind inlet boundary: stability and stratification

The specification of wind inlet condition is not trivial due to the complex physical processes inherently in the atmosphere which need to be accounted for. For instance, gradients in temperature along the height of the atmospheric boundary layer (ABL) create a corresponding density gradient and the boundary layer is said to be stratified. If air adjacent to the ground is colder than air above (stable atmosphere), mixing is suppressed as the vertical density gradient acts to dampen vertical motion and mixing of air. On the other hand, warmer, less dense air near the ground (unstable atmosphere) will lead to increased vertical mixing. Thus for any given wind, the turbulence intensity will depend on atmospheric stability. Thus the level of turbulence to which the cloud is subjected is a function of the stability condition.

Stable conditions occur during the night when there is little or no wind[61, 62]. Under this condition, surface cooling causes the air to be warmer than the ground beneath. This creates a positive temperature gradient leading to suppression of turbulence which consequently inhibits upward motion. Unstable conditions mostly develop during the day as the surface rapidly absorbs heat and transfer some of the heat to the surface wind [62]. Unlike in stable condition, a negative temperature gradient is created which enhances turbulence. The air warms up, become less dense than surrounding air and rises. Neutral condition is not very common and is usually the transition between stable and unstable conditions. This occurs during dawn and dusk with an effect that mechanical shear dominates turbulence production and

buoyancy remains negligible [63]. Therefore a parcel perturbed under this condition will maintain its original course.

In specifying the wind inlet conditions, inflow profiles are given for the wind speed, temperature, turbulent kinetic energy and dissipation rate in a manner that reflects the stability condition. Thus, the stability or stratification condition under which a given spill occurred has to be known in order to properly set up the wind inlet condition. A common method to define the stability condition of the atmosphere is through the Monin-Obukhov length; a characteristic length which specifies the relative contribution of shear and buoyancy to buoyancy production in the atmosphere. Based on the Moni-Obukhov length, atmospheric stability is commonly classified into five as summarised in Table 2-2 [64, 65].Thus, by knowing the Monin-Obukhov length of the site, stability condition is readily obtained.

Table 2-2: Classification of atmospheric conditions based on Monin-Obukhov length

Very stable	$0 < L < 200m$
Stable	$200 < L < 1000m$
Neutral	$\lvert L \rvert > 1000m$
Unstable	$-1000\text{m} < L < -200m$
Very unstable	$-200\text{m} < L < 0$

Where information about Monin-Obukhov length is not available, stability can be determined based on surface wind speed, insolation and cloud cover as shown in Table 2-3. The letters A-F refers to different combinations of surface speed, insolation and cloud cover, with A to C referring to unstable condition, D refers to neutral condition while E and F refer to stable condition. Thus, class A represents the condition of greatest instability and F represents condition of greatest stability. Historically, this classification method was introduced by Pasquill and Gifford and later improved by Turner, hence it is generally known as Pasquill-Gifford-Turner (PGT) classification [66]. However, as noted by Magidi [67] , this method of classification is not so accurate due to human error in determining cloud cover. Other classification methods are well documented in the literatures[66]

Table 2-3:Atmospheric stability classification based on PGT[67]

	Daytime solar Insolation			Night-time cloud	
Wind Speed (m/s)	strong	moderate	slight	$\geq \frac{4}{3}$	$\geq \frac{4}{3}$
<2	A	A-B	B	-	-
2-3	A-B	B	C	E	F
3-5	B	B-C	C	D	E
5-6	C	C-D	D	D	D
>6	C	D	D	D	D

2.4.2. LNG inlet boundary: source term

In LNG dispersion simulation, the incoming LNG into the domain is specified as an inlet condition, usually as a circle positioned at the base of the domain to represent a spreading pool which is boiling and injecting LNG vapour into the domain, see Figure 2-9 below. The definition of the interface between the source term model and dispersion model is a matter with diversified views[7].In two-phase models, the flow is considered as part of source term until the point where momentum (due to discharge) becomes negligible, advection dispersion model then takes over following the decay of momentum. For vapourizing pool source, the distinction is clearer since the behaviour of the pool and the cloud are very different, hence source must be the rate at which gas is created [7].The pool size and vapour generation rate must therefore be of interest. The former is affected by a number of factors such as the existence of bund or any form of constraint, sloping terrain as well as wind. The latter is affected by the rate of heat transfer from the substrate. Thus, the coupling of the near-field (source) and the far-field (dispersion) in CFD models is achieved by placing the LNG inlet boundary on the substrate to accurately mimic pool spreading on the substrate as well as the simultaneous heat transfer and subsequent pool vaporization which introduces vapour into the computational domain

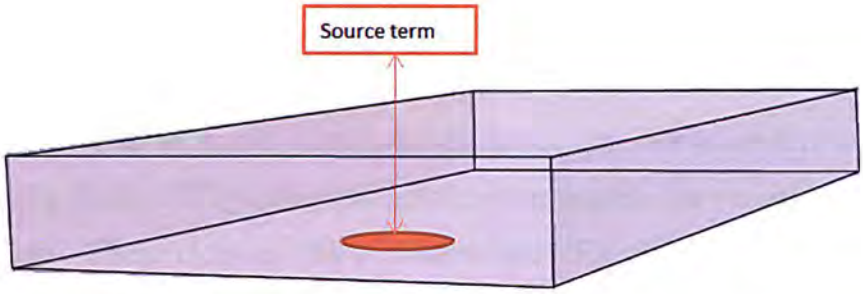

Figure 2-9: source model-dispersion model interaction through inlet boundary condition

The source term represented in Figure 2-9is a spreading pool which is evaporating simultaneously thereby injecting gas into the domain. The release of LNG, spreading, heat transfer (by conduction and convection) is handled with a source term model. The vapour dispersion is handled through a dispersion model. Therefore CFD models should be able to cope with these two aspects as well as interface them correctly. This is the main focus of the model developed in this study, as previous studies do not recognise the transient nature of source development but rather they relied on simplification assumptions to specify a constant (average) evaporation rate over the entire substrate area. But before developing a source term model and coupling that to a CFD dispersion model (as recommended in MEP) which is the main work carried out in this study, an overview of physics of source term and modelling techniques will be presented first in the next section.

2.5. Assessment of available models

The myriads of physical processes underlying LNG vapour dispersion make modelling amenable to certain simplifying assumptions. Each assumption made introduces some level of uncertainty in the modelling process and thereby drop model quality. As a remedy, the UK health and safety (HSE) through its Model Evaluation Protocol (MEP) [13]provides guidance on how dispersion models should be assessed. According to this guideline, source term model should provide input to dispersion models and are therefore almost as important as the dispersion model itself. Most previous studies avoided source term modelling, relying on an assumption that a spilled LNG will spread speedily and cover the whole substrate and thus evaporate all over the surface at which time the evaporation rate becomes equal to the spill rate. Studies that relied on this assumption, such as those of

Cormier et al[17, 62], Sklavounouss and Rigas [14], Gavelli et al [15, 16] neglected source term modelling – an obviously important aspect of dispersion modelling. There currently exist a number of dispersion models which have been developed and can be applied to predict LNG vapour dispersion. These models are in most cases part of a wider CFD package alongside other models for varieties of fluid dynamics problems. These include ANSYS Fluent and CFX, Star-CD, FLACS and FDS, with Fluent and CFX being the most widely used. This section intends to analyse existing CFD tools based on recommended best practice for LNG dispersion model as contained in HSE Model Evaluation Protocol (MEP).

2.5.2. ANSYS FLUENT

Fluent package was developed by ANSYS Inc. (www.ansys.com) and is implemented within a finite volume framework. It incorporates a model termed *species transport model* for dispersion calculations. A typical drawback of this model however is that it is a commercial package and thereby heavily limits user programming access and consequently hampers incorporation and modification of physical models to suit problem physics. This is a well-known problem in CFD modelling community and has reflected in a number of previous studies of LNG dispersion simulation carried out using this model. For instance, while it is well-known that realistic LNG dispersion model should incorporate transient pool spreading and evaporation (source term) model, all current studies carried out in FLUENT so far curiously avoids source term modelling. Rather, it is assumed that the pool fills the substrate immediately at which time the spill rate becomes equal to the evaporation rate. This simplified approach is thought to be adopted due to the difficulty in implementing source term model in commercial packages under the limited programming access provided. A more realistic approach should reflect transient pool spreading and evaporation rather than rely on non-physical assumptions. Models which could account for time varying pool size and evaporation has been highly encouraged in a number of Health & Safety Executive (HSE) reports [7, 13].

2.5.3. ANSYS CFX

CFX is another commercial CFD package released by ANSYS for solving a wide range of fluid flow problems. It does not have a dedicated model for dispersion

modelling, but incorporates a range of mixture transport models that can be adapted for such a problem, such as the *multi-component mixture model.* Being a commercial package, CFX suffers same drawbacks as FLUENT which significantly reduce its applicability in real life dispersion simulation. Consequent upon the inherent limitations, LNG dispersion modelling within the frame work of CFX has not been able to incorporate transient pool spreading and evaporation. Sklavounos etal[14]employed the general purpose CFD package "*CFX*" to solve the sets of equations governing LNG cloud dispersion in order to simulate the Coyote Series large scale spill trials (spill into a dike and subsequent dispersion). In order to circumvent explicit source term modelling, they calculated an upward directed velocity from an average vaporisation rate reported during the experiment using the density of methane. This velocity was implemented as velocity inlet condition at the inlet of the LNG, similar to the common practise. A recent simulation by Udechukwu et al[68]within CFX faced a similar challenge and therefore relied on same assumptions to specify source term over an arbitrary gas inlet patch area.

2.5.4. Star-CD

Star-CD developed by CD-ADAPCO England (www.cd-adapco.com) is yet another general purpose commercial package. Using this package, R.K. Calay & A.E Holdo [69]carried out a simulation of the dispersion of flashing jet release. The purpose of their work is in two-fold: (1) to investigate the sensitivity of concentration field to inlet conditions, and (2) to derive and validate expressions that could be used to calculate inlet conditions from the conditions known prior to a leak. The result of their simulation showed a strong dependence of concentration field on inlet conditions. While they claimed to have obtained good agreement with experiment in respect of concentration field, the data is curiously missing in their paper. But judging by their prediction of droplets' temperature field, it is readily seen that there is a wide gap between their result and experimental data .Similarly, the prediction of droplet size as a function of distance from the release source was not in agreement with experiment

2.5.5. FLACS

The Flame Acceleration Simulator (FLACS) was developed by Gexcon AS (www.gexcon.com) primarily for explosion modelling, hence it was designed for

dispersion modelling. FLACs predict transient pool spreading and evaporation using the shallow layer equations and can be applied to predict dispersion via the Navier-stokes equations. Thus, it uses finite volume technique for both source term and dispersion model, which make it computationally costly. Moreover, in a study conducted by Midha et al [70], FLACS grossly over-predicted results at most sensor locations simulated.

2.5.6. FDS

Fire Dynamic Simulator (FDS) model was developed by the National Institute of Standards and Technology (NIST) for low speed, thermally-driven flow, with an emphasis on heat and smoke transport from fires. This code has been modified by Parihar et al [71] for dispersion modelling capability. The main drawback of FDS lies in its discretization technique. Rather than employ a finite volume technique in the discretization of the governing equations, the FDS model employs Finite Difference which does not conserve flow properties. Moreover, there is no evident in the paper that the source term developed was validated or even incorporated in the dispersion model as the authors went ahead to adopt a constant evaporation rate to represent gas injection at the LNG inlet boundary. The results of their simulation showed substantial over prediction at most of the sensor locations simulated, compared to experiment.

2.6. Proposed model

Based on the foregoing, a robust dispersion model which takes into account transient pool spreading and evaporation model with a good compromise of computational cost and accuracy seems to be lacking. Moreover, most of the models presented in the previous section using commercial software require huge financial investment on licensing. Thus, this present study aims to achieve two objectives: (1) develop a comparatively fast model for LNG dispersion prediction which would account for transient pool spreading and evaporation and (2) provide a step by step guideline on how to develop such model from a freely available C++ toolbox, OpenFOAM. This will be particularly advantageous to industries in the oil and gas sector and environmental agencies wishing to predict wind flow in the built environment or atmospheric dispersion of flammable and toxic gases. It is therefore expected that an INTEGRAL- CFD dispersion model can provide the needed compromise and

therefore is proposed and developed in the next chapter of this study. This means creating a coupled code that would use an integral model for the source term and a CFD model for the dispersion. In order to develop the intended model, a critical consideration of the series of events following an LNG spill is required. Thus the next section presents a theory on source term. Key parameters affecting source term behaviour and which should be included in modelling transient pool spreading and evaporation are discussed.

2.7. Overview of source term

Accurate description of source term is critical in any consequence modelling, as results of such forms an input data for CFD dispersion modelling. This demands the engineer must have a good understanding of the underpinning physics of source behaviour. In the context of this study, source behaviour refers to the series of processes that occurs in the near field of a spill (from liquid release to pool formation, spreading and evaporation) up to LNG vapour generation. Releases at elevated pressures leads to the production of a flashing jet. In the case of an unobstructed jet, a large proportion of the jet might vapourize before any pool is formed as have been demonstrated in two different experimental studies carried out by Adventica [72] and Shell [73]. The fraction of LNG that may flash evaporate depends on the ambient temperature, the pressure and temperature of LNG within the containment, the size of breach, the initial velocity of the jet and the fluid trajectory [7]. A common practise in the modelling community has been to carry out a flash calculation (assuming isenthalpic expansion) to determine the fraction that flashed evaporated. When stored at atmospheric pressure which is typically the case during marine transportation, a breach in the containment will lead to a form of release in which by far most of the liquid will reach the substrate forming a liquid pool [18]. The predominant factor that can have significant effect on pool development is the temperature difference between the spilled LNG and the substrate (ground or water) upon which the liquid spills. This temperature difference significantly affects the heat transfer from the substrate to the spilled LNG. If the temperature is adequately high (above the Leidenfrost point), a thin layer of vapour film will form at the interphase separating the liquid pool from the substrate resulting in a form of boiling known as *film boling*. The existence of the film limits the rate of heat transfer to the pool and consequently the vapourization rate. At temperature difference below the

Leidenfrost temperature, the film may collapse bringing the liquid pool into direct contact with the surface thereby significantly increase heat transfer rate .This boiling regime is known as nucleate boiling. Somewhere between the film boiling and nucleate boiling regimes lies the transition regime which will be described in the modelling section (chapter 3) of this thesis. Aside the temperature difference, release scenario also affects pool development and vapour generation rate significantly as summarised in the PhD thesis of Benjamin Cormier [74]and a report prepared by UK HSE. Other key parameters depend on the release scenario as illustrated below:

For Onshore LNG Spill

1. State of the land surface
2. LNG Composition

For Offshore LNG Spill

1. Ice/hydrate formation
2. LNG-water turbulence
3. Breach location relative to water surface

State of the land surface

An important factor that plays a key role in source term development in an onshore scenario is the nature of the solid surface upon which LNG is spilled. Experimental studies have shown that the rate at which heat is transferred from the substrate to the spilled liquid is depends on the thermal properties of the solid material on which LNG is spilled (concrete, grass, sand) [75]. Such parameters as thermal conductivity, heat capacity and density play major role in heat transfer to the liquid pool and essentially differ for each material. For soil substrates, boiling rates are enhanced by percolation of LNG into the upper soil layers. This effect is most pronounced for dry soils. Moist soils tend to form a frozen barrier which limits the extent of percolation, although this may be compensated by the action of the heat of fusion of the moisture. Heat transfer rate are greatly reduced when a thin plastic barrier is used to reduce percolation

LNG Composition

The occurrence, or otherwise, of film boiling or nucleate boiling has been found to depend on the composition of LNG for laboratory scale spills [7].In a laboratory scale experimental work carried out by Boe [76], it was discovered that the boil-off rate for a mixture containing 97% of methane was twice as much as that of pure methane owing to the collapse of film boiling. A previous experiment, also of laboratory scale conducted by Boyle and Kneebone [77] showed a similar trend. However, in a field-scale test carried out by ESSO in which the fraction of methane was varied between 84-95 percent, composition had no significant effect on vapour generation rate[78].

Ice and hydrate formation

The spill of LNG on water is usually characterised by another physical process, ice formation. This occurs due to the exposure of the water surface to LNG at a very low temperature with a temperature difference in the order of 180K. Prolonged contact will substantially drop water temperature. Should the water temperature fall below the freezing point of water, an ice layer will begin to form whose thickness depends on the duration of contact of LNG and water. Ice formation has been observed in a number of laboratory scale experiments [75, 79]. However, Valencia and Reid [80] noted that it is difficult to notice any ice formation in open sea due to the effects of natural convection in the water. Drake, Jeje and Reid[81] made an interesting point that ice formation may be hydrates. Through a small scale experimental test, they noticed an immediate weight gain in the water following the evaporation of the LNG, and a subsequent weight loss when the temperature has normalised. On the basis of this observation, they then pointed out that this might indicate that some hydrocarbons were still present in the water, perhaps as hydrates, but they dissolve and disappear as the temperature increase and normalise. The presence of the layer of ice has been found to contribute significantly to the physics of pool spreading and evaporation through the process of heat transfer. Thus, the amount of vapour generated is substantially affected by ice formation. In spills on deep and unconfined water, no substantial ice has been observed [7, 82].

Breach location relative to water surface

Alike to the effect of ice /hydrate formation and operating turbulence between LNG pool and water, the effect of puncture location is applicable only to spills on water.

For spill on water, a hole in an LNG tanker storage vessel or any other offshore facility such as LNG FPSO and LNG FRSU can be caused by events such as grounding, collision or terrorist attack. In such a scenario, the location of the hole relative to the water surface will influence the dynamics of the spill process and eventually the source term (pool spreading and evaporation).The three locations of interest are highlighted in this study, see Figure 2-10.A spill from a significant elevation above the water surface (category I) will result to the penetration of LNG into the water in a manner that generates turbulence. The two liquids will swirl around, mixing vigorously, leading to rapid vaporization which further agitates the mixing region. This substantially enhances the transfer of heat between the liquids and hence the evaporation rate. This fact has been further authenticated by an experiment conducted by the Bureau of Mines and reported by Hissong [18] in which it was established that the penetration depth influences the turbulence generation, heat transfer and evaporation rate

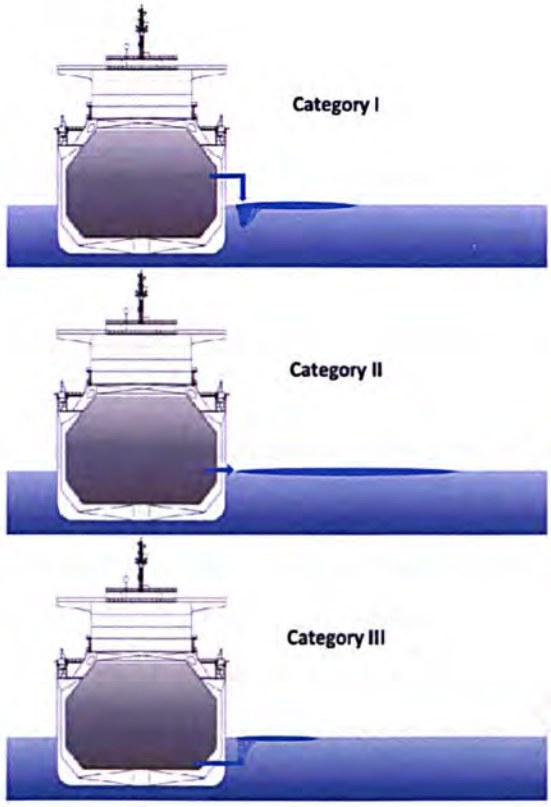

Figure 2-10: categories of marine leak locations

The first, albeit non-validated correlation to quantify the additional heat transfer due to penetration into water was proposed by Hissong through a non-dimensional parameter referred to as turbulent factor, defined as the ratio between turbulent heat transfer coefficient between LNG and water in the presence of turbulence to that based on quiescent boiling. It then follows that if the turbulence factor is known, the turbulent heat transfer coefficient can be calculated by multiplying the turbulent factor with the quiescent heat transfer coefficient. By simulating two of the ESSO tests, Hissong attempted, albeit inconclusively to derive an expression for turbulent factor, but categorically admitted that this is a topic warranting further study. For the simulations carried out in this current study, a quiescent release is assumed giving a turbulent factor of one. But, the influence will be analysed as part of parametric analysis to evaluate its possible influence, if any.

A hole at the water surface (category II) is more likely to lead to quiescent release onto water surface. Such a release will create a larger pool than a release in which the hole is located above the water line. There is also a possibility of water flowing into the containment thereby further complicate the physics of the problem. Underwater spills (category III) emanate from beneath the water surface and rises to the surface to form a pool. In such a release scenario, the released LNG absorbs heat and begins to evaporate before getting to the surface. This substantially reduces the amount of pool formed, if any.

2.7.1. Shallow layer models

Source term modelling entails quantification of the near field behaviour of the spilled. A CFD methodology based on the shallow water theory has been one of the most widely used and is treated in this section. Shallow layer models are based on the solution of the well-known shallow water equations and are justifiably applied when the thickness of the fluid in question is small compared to its horizontal dimensions [83]. The equations are obtained from depth integrating the Navier-Stokes equations, assuming the horizontal dimensions to be very much greater than the vertical dimensions. Thus they can be adapted to study a range of shallow layer fluid flows including pool spreading and vapourization (on both land and water), breaking waves on coastlines and dam break problems[84]. However, a common

drawbacks of the standard shallow water models is that they are strictly only applicable in the limit of negligible vertical acceleration.

2.7.1.1. Shallow layer equations

A system of non-linear partial differential equations that allows for characterisation of the pool height and velocity in time and space is given by the so-called "shallow layer" equations. As earlier mentioned, these equations are obtained from depth averaging the Navier-Stokes equations and hence are based on the conservation of mass and momentum. Considering the volume of an incremental pool element, the mass conservation equation is given by balancing the volume change in time with the sum of all volume fluxes passing the element's boundaries, resulting in:

$$\frac{\partial \varphi}{\partial t} + \frac{\partial(\varphi\, u_i)}{\partial x_i} = \frac{\dot{m}_L - \dot{m}_V}{\rho_l} \tag{2-94}$$

And the conservation of momentum equation takes a simplified form as expressed in equation (2-95).

$$\frac{\partial(u_i)}{\partial t} + u_j \frac{\partial(u_i)}{\partial x_j} = g\,\Delta \frac{\partial(\varphi + z)}{\partial x_i} + F_{\tau,i} \tag{2-95}$$

Where the parameter Δ equals one for onshore spills and $\Delta = (1 - \rho_l/\rho_w)$ for spills on water, φ is instantaneous pool thickness, the second term on the right is used to account for friction between the spill and the substrate, and is given by:

$$F_{\tau,i} = \frac{1}{8} f_f u_i |\vec{u}| \tag{2-96}$$

Heat transport is predicted via a transport equation for specific enthalpy which is expressed as:

$$\frac{\partial h_s}{\partial t} + u_i \frac{\partial h_s}{\partial x_i} = \frac{\dot{m}_L}{h_s}(\theta_L - \theta) + \dot{q}_c + \dot{q}_{rad} + \dot{q}_{sub} + \dot{q}_{evap} \tag{2-97}$$

Here, the first term on the right hand side represents heat gain due to leak, $\dot{q}_c$ is heat transfer by convection from wind to the pool to the pool, $\dot{q}_{rad}$ is heat transfer by

radiation to the pool, $\dot{q}_{sub}$ denote heat transfer from the underlying surface to the pool and $\dot{q}_{evap}$ is heat loss due to evaporation. Among these means of heat transfer, it has been widely established that heat transfer by conduction from the substrate to the LNG pool contributes most to vapourization of the LNG pool. Heat transfer from the substrate is approximated in FLACs as:

$$\dot{q}_{sub} = \begin{cases} \dfrac{\lambda_G(T_G^0 - T_l)\left(1.5 - 0.25(t - t')\right)}{\sqrt{\pi\alpha_G}} \text{ if } t < 4sec \\ \dfrac{\lambda_g(T_G^0 - T_l)}{\sqrt{\pi\alpha_G}(t - t')} if\ t \geq 0 \end{cases} \quad (2\text{-}98)$$

In Equation (2-98) above, λ_G and α_G are the substrate's thermal conductivity and diffusivity respectively,t' denotes the time at which the ground is first wetted at a point. Equations (2-94), (2-95)and (2-97) were discretised in FLACs in two dimensions using finite volume method. For cell face values of the convective term of the momentum equation, the upwind scheme was employed while a central difference scheme was used for the enthalpy convection term in the enthalpy equation. The equations are solved in time using the 3rd order accurate Runge-Kutta technique. The use of a computational grid and finite volume solution approach makes shallow layer models an expensive option compared to the semi-empirical similarity technique discussed below. Similarity type model will be employed for source term in the present study in order not to add significant computational expense to the CFD dispersion model.

2.7.1.2. Existing shallow layer models and their analysis

A number of models based on shallow layer principle have been developed for the prediction of cryogenic spills. Among the available models is the Spreading Liquid over Terrain (SPLOT) model which was developed at UK Health and Safety laboratory. A study by Ivings and Webber [85], and Ivings et al [86] considered the integrity of this model through comparison of SPLOT model results to analytical solution, and found a good agreement. Following this verification using analytical data, Webber et al [87] further validated this model against assorted experimental bund overtopping experiments in order to gain confidence in the model and expose any possible shortcomings. They found that the model results agree very well with

experimental bund overtopping data for vertical and horizontal walls, except cases where the liquid front hits the bund most violently relative to its height. In such situation, they suggested the use of an improved sub-model without interfering with cases in which predictions fit experimental data.

Another classical shallow layer model was developed by Hansen et al [88][89]and integrated into FLACS code for source term prediction. Effects of obstacle, sloping terrain and friction due to roughness of the substrate are accounted for. Spills on water can also be modelled. Even though, the model improved source model and accounts for a wide range of processes encountered in the vicinity of the source, there currently seems to be any record of its validation.

Also based on the shallow water equations, the Liquid Spill Modelling System (LSMS) model was developed by Cambridge Environmental Research Consultants (CERC) with support from HSE, British Gas, Gaz de France and US Gas Research Institute. LSMS is based on shallow water model for prediction of pool spreading and evaporation. It has the capability to account for the interaction of spills with vertical walls such as a bund overtopping scenario. Validation of LSMS for spills on land has been carried by Daish et al [90] through comparison with experimental data obtained from Moorhouse and Carpenter [91] and Reid [92].Additional validation has also been published by Clark and Savery [93]for spreading and bund overtopping of water in a planner channel and by Dienhart [94]for spreading and vapourization of liquid hydrogen on water.

2.7.2. Similarity models

This class of models rely on solving two equations simultaneously, an ordinary differential equation for spreading rate and a mass balance equation which relies heavily on heat transfer to the pool. However, information about the mass evaporating per-time step and mass spilled per time step is required to close the simultaneous equation. The spill rate is normally reported in experiment but can be determined using Bernoulli principle as reported by Cormier [74] if it is not known beforehand. For the mass evaporated, an energy balance approach is used as depicted by equation (2-101). With these masses determined, a mass balance equation is then established in which the mass in the pool at any time equals the mass remaining in

the previous time step plus the mass released minus mass evaporated. The full method will be described later on in this section.

In order to illustrate the mathematical basis of the similarity type models mentioned above, the Hissong model has been selected. In this model, the simultaneous equations for the spreading rate and the mass balance are of the form expressed by equation (2-99) and (2-100) respectively

$$\frac{dR}{dt} = S_K \sqrt{g\left(\frac{\rho_W - \rho_l}{\rho_W}\right)\varphi(t)} \tag{2-99}$$

The constant S_K is known as spreading constant for which Hissong reported a theoretical value of 1.16, but mentioned that experts agree that higher values must be used. Thus they used a value of 1.41 for the simulation of the ESSO Spill experiment. The densities ρ_W and ρ_l stand for the density of water and a cryogenic liquid such as LNG respectively. Integration of equation (2-99) for the radius of the pool at any time however requires information about pool thickness. Thus pool thickness $\varphi(t)$ is calculated at every time step by applying mass balance as follows:

$$M(t) = M(t-1) + \dot{M}(t) - M_{\text{evap}}(t) \tag{2-100}$$

Equation (2-100) reads thus: mass in the pool at the current time equals mass remaining in the previous time step plus mass released within the time step, minus mass evaporated within the time step. Mass released is calculated applying Bernoulli principle, while mass evaporated is calculated from energy balance and enthalpy of vapourization ΔH_{vap}.

$$\text{M}_{\text{evap}} = \frac{Q\,(t_i - t_{i-1})}{\Delta H_{\text{vap}}} \tag{2-101}$$

Here Q is the total heat transferred to the spill through conduction, convection and radiation. Formulations for calculating heat transfer to cryogenic spills can be found in Hissong. With the mass in the pool determined using equations (2-100) and (2-101) together with Bernoulli principle for outflow, the volume of LNG in the spool is calculated as:

$$V_i = \frac{M_i}{\rho_l} \tag{2-102}$$

The average instantaneous pool thickness φ_i is then calculated with the volume and the area as:

$$\varphi_i = \frac{V_i}{\pi[R(t)]^2} \tag{2-103}$$

This procedure is used until the pool thickness reaches a minimum value referred to as the stable pool thickness, which is 6.7 mm in one of the ESSO spill experiment

2.7.2.1. Analysis of existing similarity models

A number of similarity type models are currently available for source term quantification. These include the SPILL model which was developed in 1980 by Briscoe and Shaw [95]at the Safety and Reliability Directorate (SRD) for UK Health and Safety Executive (HSE).This is an integral model and derives a great deal from an earlier work by Raj and Kalelkar [96].It has the capability to model cryogenic spills on both land and water, and has been validated against experimental data on the release of $1000\,m^3$ of LNG on water and a number of other integral and empirical models. SPILL model was superseded by GASP.

Gas Accumulation over Spreading Pool (GASP) model builds on the previously developed SPILL model to describe the spreading of liquids on land or water. This model was developed by Webber [97] and Webber and Jones [98] at SRD for HSE. The governing equations are based on integral model and incorporate sub-models for the prediction of evaporation rate assuming that the substrate (water or land) is flat. Even though this model forms the basis of other spill models such as ABS Consulting model and LNGMAP model, it is not presently actively marketed by current owners [7]

Another model named FAY after the developer 'Professor Fay' of Massachusetts Institute of Technology (MIT) who also has written a number of papers over the past 30 years on the accidental release of LNG [7].After an extensive review of existing works in a recent paper [99], Fay opposed the common practise of extrapolating mathematical models and experiments for oil spills and adapting same for LNG spills i.e. the so-called shallow layer models. An alternative model was then proposed which was benchmarked by comparing predictions with China Lake experiments involving ignited LNG spills on water. Using the validated model, the effect of ocean

wave interaction on spreading pool was examined and this shows only a negligible effect on spreading. Fay referred to the alternative model developed as 'supercritical model [99]'.

Also ABS consulting incorporation, under contract with the Federal Energy Regulatory Commission (FERC), developed a model in 2004 for incidents involving accidental releases from LNG tankers [6]. The release rate of LNG from the tanker is calculated using the orifice model. Pool spreading is calculated using integral model based on Webber [7]in which frictional effect was taken into account using the shear stress in the vapour film. Heat transfer to the spreading pool was modelled assuming the temperature difference was high enough to result in formation of thin layer of film between the LNG pool and the underlying water surface. Thus they adopted the film boiling correlation of Klimenko [100]. Even though this model has been touted as reliable for the prediction of event following a large-scale spill [6], it has not been well validated against field experiment.

Following ABS Consulting, Hissong [18] developed a source model at ExxonMobil Upstream Research Company, for the simulation of LNG spill on water in October 2006. In this integral model, release rate as a function of time was obtained using Bernoulli equation. For the spreading rate calculation, a relationship previously used by Briscoe and Shaw [95]was employed. The spreading relationship was used until the pool thickness reaches a minimum value called the minimum stable pool thickness. At this point, the thickness is fixed at the minimum value and the radius is calculated using the pool volume. The model accounts for the effect of water turbulence and LNG composition, and was well validated using data from the ESSO LNG spill experiment [78].

It is also worthwhile to mention PHAST developed by Det Norske Veritas (DNV) due to its popularity in spill modelling community. PHAST accounts for whether the spill is continuous or instantaneous, whether the release is on land or water and whether the pool interacts with bund walls if confined. Further details of the model capabilities are available in Wiltox and Oke [101] and example calculations for LNG spills can be found in Pitblado [4]. The model has been well validation against GASP and experiment for spills of a wide range of materials such as LNG, butane, pentane, propane and toluene.

Another popular model is *source5 model*, developed by Attalah et al [102] for Gas Technology institute formerly known as the Gas Research institute. This integral type model is suitable for a wide range of scenarios including instantaneous and continuous releases, spills on land or water. For spills on water, two scenarios were considered i.e. one in which ice was formed on the surface of the water and another in which there was no ice formation. Further, the model allows for the presence of a sump, although nothing was mentioned as to how the model does this. Despite being able to cover a wide range of scenarios, Source5 model has a number of limitations which has been summarised elsewhere in Havens and Spicer [103].Moreover, the original developers did not validate the model against any experiment, instead they referred to other works that validated certain aspects of the model [104]

Last but not the least is Opschoor model [105] named after the developer 'Opschoor'. This is an integral model for the spreading and evaporation of LNG on land and water, based on an earlier work by Raj and Kalelka [96] . Validation studies showed that the model predictions found good agreement with the tests of Boyle and Kneebone[77], but relatively poorly with those of Feldbaeur et al [78].

Chapter 3: I-PSED model development

It has been the aim of this present study to develop an efficient integrated LNG pool spreading, evaporation and dispersion model within OpenFOAM, which will be called I-PSED in this study. Therefore this chapter starts off with a brief description of OpenFOAM toolbox and afterwards present the steps (including equations) which have been adopted to develop the intended model. The model development presented in this chapter has been undertaken in three steps. The first step is the modification of an existing combustion solver to a form suitable for dispersion simulation. This became necessary as OpenFOAM does not have any dedicated solver for dispersion simulation. A combustion solver has been chosen for modification as they are the only solvers which include species transport in addition to the Navier-Stokes equations, making it suitable for LNG dispersion modelling. Moreover, the chosen combustion solver includes full buoyancy model which is of particular importance in the dispersion of cryogenic spills as highlighted in the literature review section. Other sub models were also included at this stage to account for certain physical processes such as the turbulence generation due to buoyancy, the effect of atmospheric stratification and stability on the dispersing gas cloud etc. In the second step, a source term model was developed in MATLAB to simultaneously describe the spilling process, pool formation/spreading and the vaporization process. This is a critical step which has been ignored in most previous studies notwithstanding a number of HSE reports which stressed its importance. The third step integrates the two previous steps (1 and 2) in OpenFOAM through the creation of a new boundary condition which is capable of reading instantaneous pool radius and then create a circular inlet patch area corresponding to the radius, through which LNG vapour is injected into the dispersion calculation domain with an upward directed velocity corresponding to the instantaneous evaporation rate. The basic principle underlying this coupling is that during runtime, the location of every cell (on the LNG inlet boundary) from the pill centre is compared with the instantaneous pool radius obtained from the source term model. If the cell falls within the radius, an upward directed velocity calculated from the instantaneous evaporation rate is applied to the cell with a temperature corresponding to LNG boiling point (111K), otherwise the cell is treated as being on the substrate with upward velocity set to zero, temperature

set to ambient value and mass fraction turned off by setting to zero. Not setting the mass fraction to zero for a cell that falls outside the instantaneous radius causes the cell to inject LNG into the domain by diffusion even though the vapour injection (upward directed) velocity is set to zero. Therefore we strongly recommend that false diffusion be handled properly by adopting the velocity procedure for mass fraction as well. Considering that this transient methodology was implemented in OpenFOAM framework, the next section will briefly describe the OpenFOAM CFD toolbox

3.1. OpenFOAM Framework

OpenFOAM is an open source code originally developed at the Imperial College London for continuum mechanics problems especially CFD applications. OpenFOAM undoubtedly opens new horizon for the CFD modelling community for efficient model development, allowing industries to be updated with new models without delays on waiting for the new models to be implemented in commercial CFD codes. It is a C++ toolbox based on object oriented programming. This makes it flexible in terms of reuse and development by many users around the world, as opposed to single block programming codes. The OpenFOAM framework consists of enormous groups of libraries for different mathematical, numerical and physical models. Linking the mathematical/numerical tools with the physical models in a main C++ function produces different solvers and utilities. OpenFOAM currently incorporates a number of solvers for wide range of applications including buoyancy-driven flows, heat transfer, multiphase flows, combustion, compressible, incompressible flows and more. However, OpenFOAM does not incorporate any dedicated model for LNG dispersion but presents unlimited flexibility in developing one. After an extensive study and consideration of the available models, the rhoReactingBuoyantFoam available in version 2.2.1 as a combustion solver seems to be most appropriate for modification for LNG dispersion and hence has been adopted for modification in this study. This solver incorporates different species, heat transfer as well as buoyancy effect and hence the most suitable for LNG dispersion. The next section presents the governing equations of the rhoReactingBuoyantFoam solver highlighting their similarities and difference with the governing equations of LNG dispersion, hence introduce the first bit of modification to ensure the intended model solves the right set of equations.

3.2. Governing equations

RhoReactingBuoyantFoam is an OpenFOAM combustion solver derived from the previous rhoReactingFoam by the inclusion of a full buoyancy model. It serves as the base solver for the current model development. This model has been chosen for modification as the governing equations are same as those of LNG dispersion model, except that its species transport equation includes a reaction term as given in equation (3-1) below:

$$\frac{\partial(\rho\bar{Y}_k)}{\partial t} + \frac{\partial(\rho\bar{U}_j\bar{Y}_k)}{\partial x_j} = \frac{\partial}{\partial x_j}\left(D_{eff}\frac{\partial\bar{Y}_k}{\partial x_j}\right) + \rho\dot{\omega}_k \qquad (3\text{-}1)$$

Here $\rho\dot{\omega}_k$stands for the average reaction rate (for specie k). This reaction term is not required for a dispersion process and is deleted from the solver to obtain a non-reacting species transport solver appropriate for a dispersion process. This laid the foundation for the development of the proposed I-PSED model forming a small part of the first step in the model development process. Also, for the prescription of the turbulence associated with the vapour dispersion process, k-ε model seems more appropriate due to it being a high Reynolds formulation as described in the literature review section. But the k-ε model equations implemented in OpenFOAM is the standard form and therefore does not incorporate the term that accounts for turbulence generation due to buoyancy (G_b) which can be of immense importance in the dispersion of buoyant plume such as LNG vapour. This term has been implemented in the current study as described in what follows.

3.2.1. Buoyancy correction of standard k-ε model

Standard K-epsilon turbulence model as developed by Launder and Sharma [106] is one of the most common and widely used turbulence models. The original rationale for the development of this model was to serve as an improved alternative model to the mixing-length model as well as the algebraic models in moderate to high complexity flows. Notwithstanding the usefulness of this model and its wide use in certain industrial applications, accuracy has been reported to reduce in certain flow scenarios including buoyancy-driven flows [45, 107-108]. One would infer then, that the standard k-ε model would be inappropriate for atmospheric dispersion in which

buoyancy is known to play major role. A number of theoretical studies have been conducted to improve the standard k-ε model for different types of flows. Here, we focus on improving the standard k-ε model in OpenFOAM for buoyancy effect. For this purpose, we adopted the formulation used in Ansys Fluent in which an additional term has been added to the turbulent kinetic energy and dissipation rate to account for turbulence generation and dissipation due to buoyancy. This approach is extensively described in what follows. The term (G_b) has been added to the turbulent kinetic energy and its dissipation rate as follows:

$$\frac{\partial \rho k}{\partial t} + \frac{\partial(\rho \bar{U}_j k)}{\partial x_j} = \frac{\partial}{\partial x_j}\left[\left(\mu + \frac{\mu_t}{\sigma_k}\right)\frac{\partial k}{\partial x_j}\right] + G_k + G_b - \rho\varepsilon \tag{3-2}$$

$$\frac{\partial \rho \varepsilon}{\partial t} + \frac{\partial(\rho \bar{U}_j \varepsilon)}{\partial x_j} = \frac{\partial}{\partial x_j}\left[\left(\mu + \frac{\mu_t}{\sigma_\varepsilon}\right)\frac{\partial \varepsilon}{\partial x_j}\right] + c_{\varepsilon 1}\frac{\varepsilon}{K}(G_k + C_3.G_b) - c_{\varepsilon 2}\,\rho\,\frac{\varepsilon^2}{K} \tag{3-3}$$

$$G_b = -g_i \frac{\mu_t}{\rho \alpha_t}\frac{\partial \rho}{\partial x_i} \tag{3-4}$$

As it can be seen from equation (3-4), the buoyancy term is zero for neutral stability condition as there is no density gradient, while in Unstable condition, it evaluates to positive and hence acts to increase turbulence and in Stable condition it is negative and suppress turbulence

3.2.2. Modelling ABL stratification and stability

The profiles for wind velocity, temperature, turbulent kinetic energy and its dissipation rate have to be specified at the wind inlet boundary for LNG vapour dispersion simulation. These profiles should reflect the atmospheric stability conditions under which a given spill occurred. This is also important during model validation as a simulation test-case has to be calibrated to be a representative of the stability/stratification condition of the experimental trial adopted for benchmarking. A number of approaches have been adopted in previous studies to prescribe the inlet profiles of velocity, temperature and turbulent quantities under different stratification/stability conditions, with the most widely used being those that depend on Monin-Obukhov theory. This theory defines the turbulent viscosity based on mixing length relation, as given by equation (3-5):

$$\mu_t(z) = \frac{\rho k u_*}{\phi_m\left(\frac{z}{L}\right)} \tag{3-5}$$

Where z is the vertical height and ϕ_m is a function that depends on the vertical height and L, the Monin-Obukhov length. For neutral and stable stratification, the function is defined as:

$$\phi_m\left(\frac{z}{L}\right) = 1 + 5 * \left(\frac{z}{L}\right) \tag{3-6}$$

The Monin-Obukhov length is an estimate of the height where shear stress production of turbulence equals to the dissipation of turbulence by buoyancy; it can be expressed by the following relation derived from historical data:

$$L = \frac{u_*{}^2 T_w}{kgT_*} \tag{3-7}$$

And the friction temperature depends on the ground heat flux, $\dot{q}_w$ through:

$$T_* = \frac{\dot{q}_w}{\rho c_p u_*} \tag{3-8}$$

By assuming incompressibility, a constant shear stress and heat flux over the lower part of the ABL, modified logarithm velocity and temperature profiles can be obtained for stable stratification condition as [12]:

$$U(z) = \frac{u_*}{K_V}\left[\ln\left(\frac{z}{z_0}\right) - \phi_m\left(\frac{z}{L}\right)\right] \tag{3-9}$$

$$T(z) = T_w + \frac{T_*}{K_V}\left[\ln\left(\frac{z}{z_0}\right) - \phi_m\left(\frac{z}{L}\right)\right] \tag{3-10}$$

Applying the same assumption used for stable stratification to unstable condition yield:

$$U(z) = \frac{u_*}{K}\left[\ln\left(\frac{z}{z_0}\right) - \psi_m\left(\frac{z}{L}\right)\right] \tag{3-11}$$

$$T(z) = T_w + \frac{T_*}{K_V}\left[\ln\left(\frac{z}{z_0}\right) - \psi_h\left(\frac{z}{L}\right)\right] \tag{3-12}$$

Where ψ_m and ψ_h are functions of height and Monin-Obukhov length and has been parameterized in previous studied as:

$$\psi_m\left(\frac{z}{L}\right) = 2\ln\left(\frac{1+x}{2}\right) + \ln\left(\frac{1+x^2}{2}\right) - 2tan^{-1}(x) + \frac{\pi}{2} \tag{3-13}$$

$$\psi_h\left(\frac{z}{L}\right) = 2\ln\left(\frac{1+x^2}{2}\right) \tag{3-14}$$

$$x = \left(1 - \frac{16z}{L}\right)^{\frac{1}{4}} \tag{3-15}$$

For neutral condition, the temperature is constant along the vertical height since there is no stratification. Considering that the Monin-Obukhov length is infinite under this condition, the velocity profile reduces to:

$$U(z) = \frac{u_*}{K_V}\left[\ln\left(\frac{z}{z_0}\right)\right] \tag{3-16}$$

Notice that the values of friction velocity, u_* and friction temperature, T_* are required in order to evaluate the velocity and temperature profiles presented above for different stability conditions. These parameters depend on other variables which may not be possible to be determined beforehand. An alternative approach exist for the determination of the friction parameters (u_* and T_*) and has been employed in this study. This involves taking site specific measurements of mean velocity and temperature at two or more heights within the ABL. Information at one data point can be sufficient if the Monin-Obukhov length for the site in question is known. By substituting the site specific data into the corresponding temperature and velocity profiles, the friction velocity and friction temperature are obtained. With these parameters known, the site specific wind velocity and temperature profiles which accounts for stability and stratification can be obtained for the wind inlet boundary.

While velocity and temperature profiles can be directly imposed as boundary conditions, the turbulent viscosity is evaluated by k-ε model as function of turbulent

kinetic energy and its rate of dissipation; so proper profiles for k and ε must be obtained at the inlet in order to have consistency with values of μ_t computed in the domain interior [12]. The consistency between the k-ε model and Monin-Obukhov theory is very important in order to obtain fully developed profile.

3.2.2.1. Neutral stability condition

Under neutral stability condition, the temperature is constant with height so that the ground heat flux equals zero giving an infinite Monin-Obukhov length according to equations (3-7) and (3-8) above. With an infinite Monin-Obukhov length, the parameter ϕ_m will tend to unity (equation (3-6)). Rearranging the transport equation of the turbulent kinetic energy under steady state condition and assuming flat profile for the turbulent kinetic energy (no gradient in the windward and crosswind direction) as was the case for velocity and temperature profiles, one finds that [12] :

$$k(z) = \frac{{u_*}^2}{\sqrt{c_\mu}} \tag{3-17}$$

$$\varepsilon(z) = \frac{{u_*}^2}{K_V(z + z_0)} \tag{3-18}$$

The profiles described in equations (3-17) and (3-18) have been implemented in OpenFOAM in conjunction with equation (3-16) as part of the current model developed in this work and used for all simulations carried out under neutral condition of ABL. The ground roughness z_0 has been included here to avoid division by zero error at a vertical height of zero. Alternatively, the equation can be used without the adding the ground roughness and a conditional statement used to set $\varepsilon(z)$ to a known insignificant value at a height of zero in the solution algorithm. Equations (3-17) and (3-18) above are mathematically consistent with the transport equation of turbulent kinetic energy. In order to be consistent with the transport equation for dissipation rate as well, Alinot and Mason [45] suggested alternative values for k-ε model constants. Another approach was also reported by Pontigia [12] in which a source term that depends on elevation was added to the dissipation transport equation. The present study follows the approach suggested by Alinot and Mason. Thus, the values of the constants (c_μ, $c_{\varepsilon 1}$ and $c_{\varepsilon 2}$), have been changed from the default shown in Table 2-1 to (0.033, 1.17 and 1.92) in this study and $c_{\varepsilon 3}$ is set to unity to represent neutral stability.

3.2.2.2. Stable stratification condition

When the atmospheric boundary layer is stably stratified, the temperature is not constant and ϕ_m does not tend to unity as was the case under neutral stability, hence the formulation for the turbulent kinetic energy is expected to take a form different for those of neutral condition. Again, considering flat profile i.e. no gradient in the windward and crosswind direction, and rearranging the equation for turbulent kinetic energy, profiles are obtained for the turbulent quantities, k and ε as follows[12]:

$$k(z) = \frac{u_*^{\,2}}{\sqrt{c_\mu}}\sqrt{\frac{\phi_h\left(\frac{z}{L}\right)}{\phi_m\left(\frac{z}{L}\right)}} \tag{3-19}$$

$$\varepsilon(z) = \frac{u_*^{\,3}}{Kz}\phi_h\left(\frac{z}{L}\right) \tag{3-20}$$

Where ϕ_h is a function similar to ϕ_m equal to that proposed by Panofsky and Dutton[109]

$$\phi_h = 1 + 4\left(\frac{z}{L}\right) \tag{3-21}$$

Equations(3-19)and(3-20) above have been implemented in OpenFOAM in the present study as inlet conditions for the turbulent quantities in conjunction with the corresponding velocity and temperature profiles (equations (3-9) and (3-10)) and used for all simulations carried out under stable condition of atmosphere. As was the case in neutral stability condition, the equations are only consistent with the transport equation for turbulent kinetic energy and not the dissipation rate. Therefore the values of (c_μ, $c_{\varepsilon 1}$ and $c_{\varepsilon 2}$) suggested by Mason and Alinot has been used instead of default values and the $c_{\varepsilon 3}$ set to 3 for stable atmospheres.

3.2.2.3. Unstable stratification condition

Adopting the same argument i.e. no gradient in spanwise and crosswind direction, for an unstable atmosphere gives the profiles of turbulent kinetic energy and dissipation rate consistent with those reported by Cormier in a previous work [17]:

$$k(z) = 5.48\, u_*^2 \sqrt{\frac{\phi_\varepsilon\left(\frac{z}{L}\right)}{\phi_k\left(\frac{z}{L}\right)}} \tag{3-22}$$

$$\varepsilon(z) = \frac{u_*^3}{Kz}\phi_\varepsilon\left(\frac{z}{L}\right) \tag{3-23}$$

Where $\phi_\varepsilon$and $\phi_k$are functions of the vertical height above ground and Monin-Obukhov length:

$$\phi_\varepsilon\left(\frac{z}{L}\right) = \frac{1}{x^2} \tag{3-24}$$

$$\phi_k\left(\frac{z}{L}\right) = \frac{1}{x} \tag{3-25}$$

Note that x retains its form as a function of height as previously described in equation (3-15) above. Equations (3-22) and (3-23) have been implemented in OpenFOAM for the turbulent variables together with the profiles of temperature and velocity (equations (3-11) and (3-12)) and used for all simulations conducted under unstable condition. Again, the equations are only consistent with the transport equation for turbulent kinetic energy and not the dissipation rate, hence the values ofc_μ, $c_{\varepsilon 1}$ and $c_{\varepsilon 2}$ have been changed accordingly, and $c_{\varepsilon 3}$set to -4.4 as suggested by Mason and Alinot.

3.3. Source term model development

This section presents the development of source term model to provide input to the dispersion model, hence constituting the second step in the developmental process of the integrated model proposed in this work. Here, certain aspects of an original work by Hissong (Exxon Mobil Research group) and another work by ABS Consulting Limited will be combined to develop a robust and fast numerical procedure to predict accidental release, pool spreading and evaporation. Therefore, the resulting model

will be referred to as pool spreading and evaporation (PSE) model. PSE is organised as a discrete set of algorithms that represent the fate of LNG as it is released into the ambient environment. At minimum, the system models the rate of release i.e. blowdown from a reservoir, spreading on water or land surface and subsequent evaporation of the released cryogenic liquid due to heat transfer by conduction from substrate, convection from ambient wind and radiation from the sun. The model does not currently include effect of ice formation or water-LNG turbulence as previous studies have suggested that ice/hydrate formation is limited to laboratory scale spills and has not been observed in large scale spills on deep unconfined water [4].A quiescent release from an LNG membrane tank used in modern day marine transportation is considered. Finally, LNG is assumed to be purely Methane and the properties of methane is relied upon for thermophysical and other properties. This is reasonable as methane is the major constituent and most volatile constituent i.e. the vapour generated will comprise mostly of methane.

In general, source term modelling in the context of LNG spill involves the following steps:

- Predict the mass released from the vessel within the chosen time-step
- Predict the mass evaporated from the pool within the time step
- Apply a mass balance to determine the mass remaining in the pool at current time
- By using the mass of the pool at current time, work out the average pool thickness using the latest pool radius available and LNG liquid density
- Update the pool radius by integrating the spreading relationship.

The models adopted in this study for the steps presented above are described in the following subsections.

3.3.1. Outflow (Blowdown) model

Blowdown simply refers to the transient release of LNG liquid from containment. In order to calculate the mass outflow rate of LNG from a punctured cargo tank, ABS consulting Limited suggested the use of the orifice formula i.e. equation (3-26) which relates the mass outflow from an LNG containment to the discharge coefficient, orifice area and decreasing head. This formula is the result of direct invocation of Bernoulli principle on a subcooled liquid and has been presented in

many references on consequence assessment such as AICHE [82] and TNO [110] as well as most basic textbooks on fluid Mechanics [6]

$$\dot{M}(t) = c_D \, \pi \rho_l r_b^2 \sqrt{2gH_L}(t) \tag{3-26}$$

Here, H_L is the liquid height above the breach of radius r_b, and C_D is discharge coefficient. The discharge coefficient is used to account for the fact that friction retards the flow. In this present study, the discharge coefficient is set to unity implying a frictionless smooth-edged circular orifice. Thus, this model is utilised here as a rough estimate of the rate of release as the breach would likely not be circular or smooth-edged and the actual breach geometry cannot be definitely determined in advance. As additional guidance, Federal Energy Regulatory Commission (FERC) reported Lee's [111] recommendations that for a sharp-edged orifice, the discharge coefficient approaches 0.61 for Reynolds number greater than 30,000: for a well-rounded orifice the value approaches unity and for short pipe section with length-diameter ratio not less than 3, the discharge coefficient is roughly 0.81.

3.3.2. Vapourization model

In cases where the spilled liquid is not ignited, vapourization will be majorly controlled by the rate of heat transfer to the pool. For any liquid, vapourization will in effect consist of the contribution due to evaporation and boiling, hence the overall energy balance can be expressed as [7],

$$Q = mC\frac{dT}{dt} + \frac{M_{vap}}{\Delta t}H_v$$

Where m is the mass in the pool, C is the pool specific heat capacity, and, H_v, is the latent heat of vapourization. The first term on the right hand side represents evaporation i.e. a time when the temperature of the pool is increasing and the pool is evaporating without boiling (due to the boiling point having not been reached or the partial pressure not being equal to the saturation vapour pressure at the prevailing temperature).The second term represents the part of the heat causing a phase change i.e. vapourization. For a volatile liquid such as LNG, the temperature stays fairly constant at the boiling the vapourization dominates. Under such condition, it can be

justifiably assumed that the total heat transferred to the pool results to vapourization of the pool and the evaporation part is neglected, leading to

$$M_{\text{vap}}(t) = \frac{Q(t)\Delta t}{H_{\text{v}}} \tag{3-27}$$

It then follows that if the total heat transferred within a time step Δt is known, the mass evaporated during the period can be obtained using the Methane heat of vapourization. The total heat Q(t) transfer to the pool is a contribution from conduction, convection and radiation. Heat transfer calculation is treated later on in section 3.3.4

3.3.3. Pool spreading model

Upon release, LNG will fall under gravity on the underlying surface such as land or water thereby forming a pool that simultaneously spreads and evaporates. Gravity is the dominant driving force in the spreading process. A number of equations exist for the calculation of instantaneous pool radius depending on the spill scenario i.e. whether the spill is on land or on water and whether it is a continuous or instantaneous release.For spills on land, the time history of the pool radius can be calculated by the integration of a spreading rate equation proposed by Opschoor [105]:

$$\frac{dR_p}{dt} = \sqrt{2g\,(\varphi - \varphi_{min})} \tag{3-28}$$

In which φ_{min} is a minimum pool thickness dependent on the characteristics of the substrate. The methodology presented above assumes that the hydrostatic difference between the instantaneous (actual) liquid thickness and the minimum thickness constitutes the driving force for the spreading. This results in the rate of spreading decreasing as the pool approaches the minimum pool thickness.

For spreading on water, equation (3-28) breaks down as it does not account for the partial submerging of the pool into the water. A number of spreading models have been proposed for spreading on water. Here, a gravity-inertia model reported by Cormier, as well as used in a previous work by Hissong is adopted. This approach neglects the effect of friction which is justifiable considering that friction is not expected to be important for spills on water, except for relatively rough water such as

in the presence of ice. In cases where friction is important, its effect can be incorporated using spreading relationship proposed by Webber et al [7]. In gravity-inertia spreading, gravity force pushes horizontally on the pool to spread it sideways while inertia tends to constitute resistance to counterbalance gravitational force. The gravity spreading force is given as [74]:

$$F_G = \rho_l \pi R_p{}^2 \varphi \left(\frac{g\varphi\Delta}{R_p}\right) \tag{3-29}$$

And the resistance to spreading due to the inertia of the pool is expressed as

$$F_I = \frac{1}{\chi} \rho_l \, \pi R_p{}^2 \varphi \frac{d^2R}{dt^2} \tag{3-30}$$

Following Cormier, momentum balance is then applied here by equating (3-29) and (3-30) to obtain the rate of spreading equation below:

$$\frac{dR}{dt} = S_K \sqrt{\Delta \, g\varphi(t, R_p)} \tag{3-31}$$

$$S_K = \chi^{\frac{1}{2}} \tag{3-32}$$

Recall Δ is a dimensionless relative density factor $(\rho_W - \rho_L/\rho_W)$ and notice that it can be substituted into equation (3-31) to obtain the spreading equation previously reported by Hissong as presented in section 2.7.2 . There is a theoretical value of 1.16 for S_K. But Hissong reported that higher values must be used in order to match experimental data. Experience gathered in this study further proves this notion, as spreading rates obtained using this value are significantly less than the experimentally reported values of 1-3ms^{-1} for spreading on water [72]. Thus we recommend that value of spreading constant be chosen such that the spreading rate stays within experimental range as much as possible during the duration of spreading.

To predict the instantaneous pool radius for spills on water, the spreading rate relationship is then integrated using numerical integration as follows:

$$R_p(t) = R_p(t - \Delta t) + \left(\frac{dR_p}{dt}\right)\Delta t \tag{3-33}$$

The differential term on the right-hand side represents the original expression for the spreading rate and is evaluated from equation (3-28) for spills on land or (3-31) for spill on water. But considering that this term involves the pool thickness, information about the instantaneous pool thickness is required in order to close the pool radius equation above. For the cylindrically shaped pool of uniform thickness $\varphi(t, R_p)$ considered in this study, it has been possible to deduce the instantaneous pool thickness through a number of steps. First a mass balance is invoked based on equation (2-100) to determine the mass remaining in the pool during a given time step from which the volume in the pool is calculated as follows:

$$V(t) = \frac{\rho_l}{M(t)} \tag{3-34}$$

And the pool thickness is calculated from the volume and the pool cross sectional area as follows,

$$\varphi(t, R_p) = \frac{V(t)}{\pi\left[R_p(t)\right]^2} \tag{3-35}$$

It is therefore clear that the equations above can be solved iteratively to predict the instantaneous pool radius and evaporation rate if the heat transfer is known. Thus, heat transfer is treated in the next section to close the equation set.

3.3.4. Heat transfer to the pool

Spreading of LNG on a substrate, land or water, occurs with a simultaneous vaporization of the liquid due to heat transfer.

$$Q = Q_{con} + Q_{conv} + Q_{rad} \tag{3-36}$$

The instantaneous total heat transferred to the pool i.e. Q (t) as used in the vaporization model equation (2-101) arises from several mechanisms, namely heat transfer from substrate and heat convection from wind. Thus the total heat transfer is summation of contributions from these mechanisms.

3.3.4.1. Conduction

In the calculation of heat transfer from substrates, one dimensional heat conduction equation can be used. By implication this means that the transfer of heat by conduction to the liquid pool is driven by the temperature gradient, the larger the temperature gradient, the greater the heat flux. While the use of Fourier's law can provide an estimate of the heat flux to the boiling liquid, it can only be applied if the LNG is in direct contact with the substrate. However, this is rarely the case as previous research [4, 18] have shown that there will not always be contact as superheating of the pool would lead to formation of bubbles which can coalesce into a vapour film and thereby prevent direct contact. This complex phenomenon makes it a challenging task to predict the heat transfer process during boiling

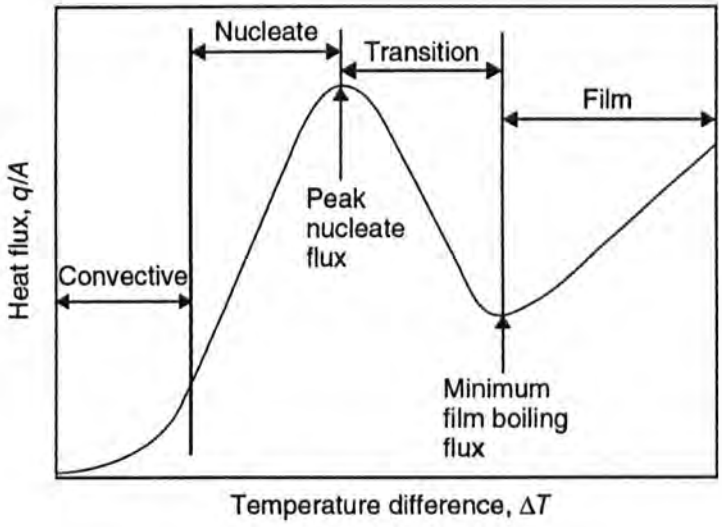

Figure 3-1: Typical film boiling heat flux curve [4]

Figure 3-1 is a classical liquid boiling curve which indicates that as the value of superheat temperature increases, the boiling process transverses four distinct regimes:

1. **Natural convection**: the superheating level (ΔT) is very low and heat transfer is solely due to internal natural convection within the heated pool, hence there

is perfect contact between the substrate and the pool as no bubble is formed. Hot liquid from the heated bottom rise to the surface and are replaced by cold liquids from the top. On getting to the top, the superheated liquid which is in metastable condition will evaporate. The minimum temperature difference required for bubble formation is called the Onset of Nucleate Boiling (ONB)

2. **Nucleate boiling regime**: The pool is in direct contact with the substrate and bubbles form but only at distinct intervals. Due to the direct contact, at higher temperature difference, a maximum or critical heat flux (q_{crit}) occurs at a temperature known as the critical excess temperature (ΔT_{crit}) marking the onset of vigorous bubble formation at which time the nucleate boiling ceases.
3. **Transition boiling regime**: In this regime, there is sufficient superheat to support vigorous formation of bubbles, but not enough for the bubbles to coalesce into a stable vapour film. Therefore, boiling takes place in both nucleate boiling and film boiling regimes.
4. **Film boiling regime:** Here, the bubbles can form so quickly to maintain a stable vapour film at the interface between the substrate and the pool. This film forms a protective coating, limiting heat transfer to the LNG pool due to its lower thermal conductivity compared to the liquid pool. The heat flux to the pool decreases until a certain temperature called the minimum point temperature (ΔT_{min}) is reached at which time the heat flux goes through a minimum (q_{min}).For a saturated liquid, this temperature is equal to the Leidenfrost temperature, T_{LF}.

The Leidenfrost temperature (ΔT_{min}) is given in terms of the pseudo-critical temperature of LNG T_C, the liquid temperature T_L, the specific heat capacity C_P, and the thermal conductivity of LNG (subscript L) and water (subscript w) as [4] :

$$\Delta T_{min} = (T_C - T_L)\left[0.16 + 0.24\left(\frac{\rho_L C_{PL} K_L}{\rho_w C_{Pw} K_w}\right)\right]^{\frac{1}{4}} \qquad (3\text{-}37)$$

Based on equation (3-37) above, the superheat temperature for boiling of LNG on 10° C water has been estimated in previous studies to be around (283 – 111) ° K or 172 ° C, which is well above the Leidenfrost temperature of methane at 161 ° K [4].Therefore heat transfer from the substrate to the boiling pool is considered to be from film boiling in this study. In the case of spill on water, mixing by natural

convection keeps the water surface at approximately constant temperature and surface cooling is not expected.

Film boiling heat transfer correlation

In the absence of ice formation, heat conduction from water is a function of film boiling heat transfer coefficient ,h_f the instantaneous pool area, and the superheat temperature as [18]:

$$Q_{\text{con}} = h_f\, \pi[R_p(t)]^2 (T_W - T_L) \tag{3-38}$$

The heat transfer coefficient can be expressed in terms of the film boiling Nusselt number N_{uf} , the thermal conductivity of LNG vapour evaluated at film boiling temperature (taken as boiling temperature of LNG) K_{VF} , and a characteristic length, known as the critical length as:

$$h_f = \frac{Nu_f K_{VF}}{L_c} \tag{3-39}$$

$$L_c = 2\pi \sqrt{\frac{\sigma_s}{g(\rho_L - \rho_V)}} \tag{3-40}$$

Here, σ_s is the interfacial surface tension between LNG liquid and the vapour. The film boiling Nusselt number is given by

$$Nu_f = 0.19\,(A_r Pr_V)^{\frac{1}{3}} F_1 + 0.0086\sqrt{A_r}\, Pr_V^{\frac{1}{3}} F_2 \tag{3-41}$$

In which A_r and Pr_V are the Archimedes number and LNG vapour Prandtl number respectively and are expressed as:

$$A_r = (2\pi)^3 \frac{\sigma^{1.5}\rho_V}{\mu_V{}^2\sqrt{g(\rho_L - \rho_V)}} \tag{3-42}$$

$$Pr_V = \frac{c_V \mu_V}{K_V} \tag{3-43}$$

And the dimensionless functions F_1 and F_2 are given by Klimenko[100] in terms of heat of vaporization, the specific heat capacity of the liquid LNG pool and the temperature difference between the cryogenic pool and water surface :

$$F_1 = \begin{cases} 1 & if \left(\frac{H_v}{C_{PL}\Delta T}\right) > 1.4 \\ 0.89\left(\frac{H_v}{C_{PL}\Delta T}\right)^{1/3} & if \left(\frac{H_v}{C_{PL}\Delta T}\right) \leq 1.4 \end{cases} \quad (3\text{-}44)$$

$$F_2 = \begin{cases} 1 & if \left(\frac{H_v}{C_{PL}\Delta T}\right) \leq 2 \\ 0.71\left(\frac{H_v}{C_{PL}\Delta T}\right)^{1/2} & if \left(\frac{H_v}{C_{PL}\Delta T}\right) > 2 \end{cases} \quad (3\text{-}45)$$

3.3.4.2. Convection heat transfer to the pool

When bulk fluid motion is present, it mixes the warm and cooler part together thereby replacing regions of warm fluid with cooler ones. The fluid motion can be natural due to density stratification and buoyancy effects (free convection) or induced by an external device (forced convection). Examples of free convection are the air near a burning candle rising or lake water circulating due to density stratification. Forced convection is of particular important in process equipment like boiler and heat exchanger or in heating, ventilation and air-conditioning systems (HVAC).In the case of LNG boiling on water surface, convection of heat from the ambient wind to the pool is very likely. The equation that governs convection process is a result of Newton's law of cooling, written as[112].

$$Q_{conv} = h_{air}\, \pi\left[R_p(t)\right]^2 (T_{air} - T_L) \quad (3\text{-}46)$$

Equation (3-46) shows that the driving force for heat convection is temperature difference which was also the case for heat transfer from the substrate. Similar to the film boiling heat transfer coefficient, h_{air} is the convective heat transfer coefficient.

In the current model, the convective heat transfer coefficient has been described following Hissong model:

$$h_{\text{air}} = \frac{N_u K_a}{D_p(t)} \tag{3-47}$$

Where K_a denote the air thermal conductivity evaluated at film temperature, D_p(t) the instantaneous pool diameter which is just twice the radius and N_u denote the Nusselt number for which Hissong reported a standard correlation, written as

$$N_u = 0.037\, Re^{0.8} Pr^{\frac{1}{3}} \tag{3-48}$$

The reported formulation for Reynold number and the air vapour Prandtl number (at film temperature) is as expressed below

$$Re = \frac{D_p(t) u_a\, \rho_a}{\mu_a} \tag{3-49}$$

And the Prandtl number is a function of wind velocity and air density as given below:

$$Pr = \frac{c_{Pa} \mu_a}{K_a} \tag{3-50}$$

In Equations (3-49) and (3-50), u_a is the wind speed, ρ_a the density of air, μ_a the dynamic viscosity of air and c_{Pa} is the heat capacity of air. All thermophysical properties are have been evaluated at film conditions.

3.3.4.3. Radiative heat transfer to the pool

Heat transfer by radiation can also be included. It is fundamentally different from those of convection and conduction. If a hot object is suspended in evacuated box whose walls are at lower temperatures, heat will be transferred to the walls notwithstanding the non-existence of a transfer medium. Heat transfer in his case is made possible by energetic waves or particle. In the case of an LNG pool boiling on a water surface, two radiative sources are possible, namely, radiation from sun and radiation from pool fire if any. With focus on unignited pools, the primary source is then limited to solar radiation. The heat transfer from above the pool due to solar radiation is given as:

$$Q_{rad} = \pi [R_p(t)]^2 S \tag{3-51}$$

Where S is the solar heat flux which is approximately 1000 W/m^2 in cloudless daytime sky [4]. For long wave radiation, the rate of heat transfer to the pool is evaluated as:

$$Q_{rad} = \pi[R_p(t)]^2 \epsilon B_K \tag{3-52}$$

Where ϵ stands for the surface emissivity and B_K (5.667 x 10^{-8}) is the radiative Stefan Boltzmann's constant [112].However, heat transfer to the pool by solar radiation is negligible compared to other heat transfer mechanisms, but might become important with insulated impoundment basins [4].

3.4. Source term- dispersion model coupling

The coupling technique presented in this section consists of the creation of a new boundary condition in OpenFOAM. The newly developed boundary condition (poolInletTempFixedValue) has the capability to read instantaneous pool radius and LNG vapour injection velocity supplied from the source term model. Thus, the source term model provides a look-up file from which newly developed boundary reads radius and injection velocity at every calculation step. These values are then used to inject appropriate mass flow rate of LNG vapour into the domain through the boundary cells that fall within the radius at every step of the calculation process. It then follows that poolInletTempFixedValue serves as a link between the source term model and the vapour dispersion model and therefore incorporates the pool spreading and evaporation processes into the vapour dispersion calculation. The flowchart for the implementation of the coupling algorithm is as shown in Figure **3-2**. At the beginning of every time step, the distance of every cell on the boundary from the spill centre (r) is determined. Afterwards, the instantaneous radius and LNG vapour injection velocity are read from a data file provided by the source term model. Note that the velocity is obtained from the evaporation rate, pool area A (calculated from current radius assuming circular shape) and LNG vapour density evaluated at film boiling temperature as expressed in equation (3-53).

$$V(t) = \frac{\dot{m}(t)}{\rho A_p} \tag{3-53}$$

The linear interpolation capability of OpenFOAM makes it possible to use time-step different from that used in source term model calculations.

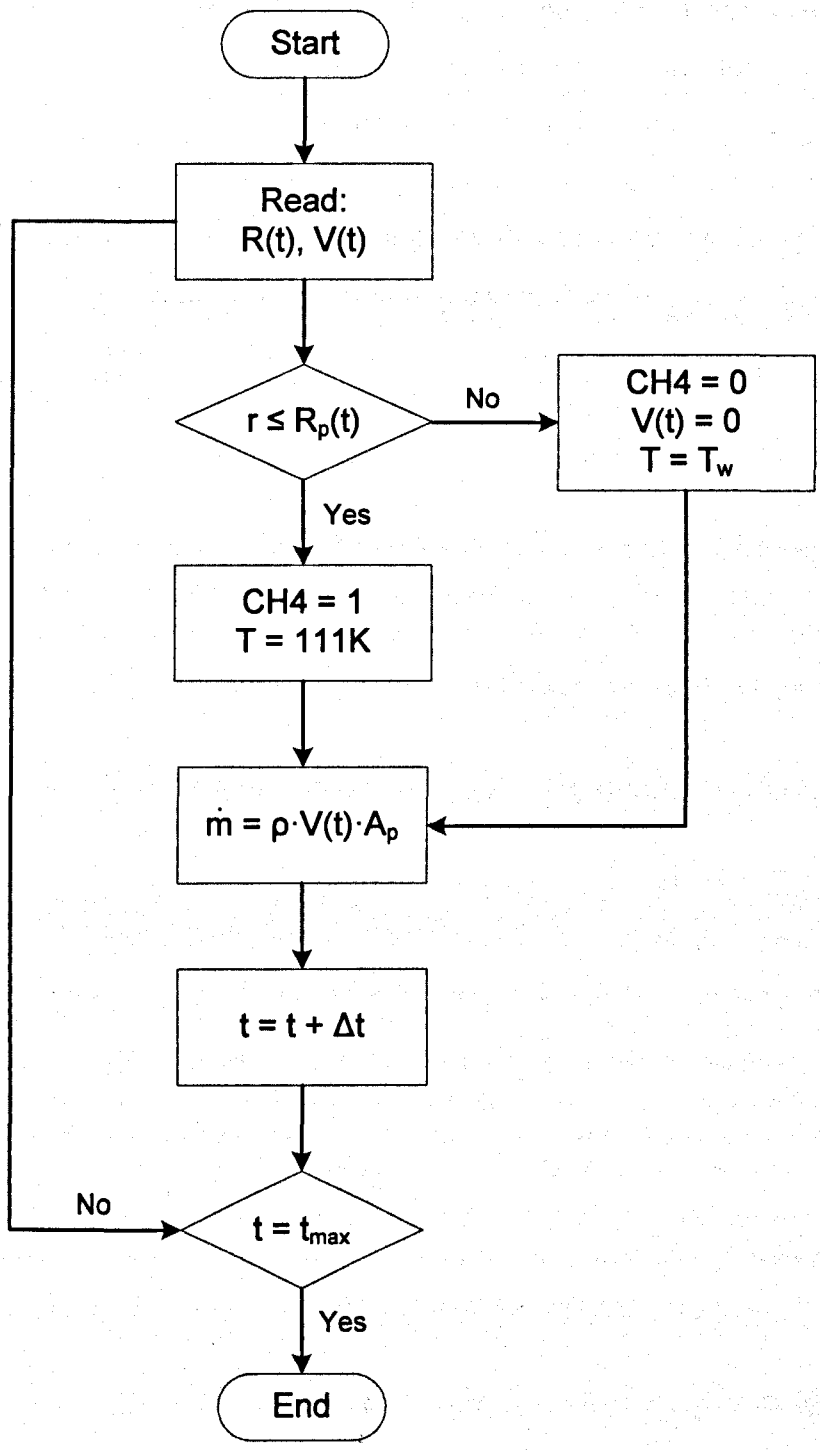

Figure 3-2: Flowchart for the coupling algorithm

With known distance of all boundary cells (r), instantaneous radius R (t) and velocity V (t), poolInletTempFixedValue applies this velocity value to all the cells that fall within the radius. Cells outside the radius i.e. unwetted cells are assigned an injection velocity of zero. LNG mass fraction is set to unity in the wetted area and zero outside

to ensure that mass is injected into the domain only from the cells which are already in contact with the spreading pool. Also, temperature of the cells within the instantaneous radius is set to boiling temperature of LNG. Cells not bounded by the radius are assigned temperature corresponding to the substrate temperature. This process is iterative and therefore is repeated at every time step, hence the newly developed boundary condition acts as a proxy that provides pseudo- pool spreading and vapourization data to the dispersion to the OpenFOAM Navier-Stokes dispersion solver. Thus, the coupled model developed is hereby referred to as integrated pool spreading, evaporation and dispersion (I-PSED) model and will be validated later on.

Chapter 4: Validation and parametric study

In this chapter, the integrated model (I-PSED) developed in Chapter 3 is validated with focus to establish the suitability of the current approach. LNG dispersion model must be valid before it can be applied for risk assessment of accidental spills. Recognising the importance of proper assessment of LNG dispersion models in the risk assessment community, Health and Safety Laboratory (HSL) carried out a research project in 2006 to develop guidelines for the evaluation of LNG dispersion models. This led to the development of a Model Evaluation Protocol (MEP) which includes a checklist of model assessment criteria and a structure for complete model evaluation. MEP identified a number of field test experiments as suitable for LNG dispersion model validation purposes, namely, the Burro [113], Coyote [114], Falcon [115] and the Maplin Sands [116]experiments. These experiments involved releases of large quantities of LNG either on water or Land. A full description of these experiments is available in Koopman et al [117]. MEP also recognised the importance of the source term model stressing the need to validate such models before it can be used in a dispersion simulation, although it acknowledged the lack of source data for the experiments included in the MEP database.

Another key aspect of the MEP is the definition of physical comparison parameters [118]. The guideline requires that both point-wise and arc-wise comparison be carried out. The former involves comparison between model predictions and experimental measurements paired at specific points/sensor locations. The latter involves comparison between measured data and model prediction along an arc at specific radius from the spill centre. In arc-wise comparison, vapour concentration data recorded by sensors along an arc are time-averaged over a time interval. The maximum time-averaged concentration recorded in the experiment across an arc at specified radius is then compared with predicted values. The essence of arc-wise comparison is to circumvent possible uncertainties which may result from wind meandering. Thus, it is most appropriate in the presence of medium to strong wind level during which plume motion is determined primarily by wind direction.

The remaining sections of this chapter are dedicated to a validation exercise carried out to determine the integrity of I-PSED model relative to the conventional

modelling approach. In particular, a simulation of the Coyote series of experiments as well as the Maplin Sands experiments is carried out using the current model and the conventional approach, and results compared with experimental data. In the immediate next section, validation of the source term model is first carried out. This includes a description of the experimental test-case used. The simulation procedure is discussed and results compared with experimental data. Section 4.2 then focuses on the validation of the coupled LNG dispersion model (I-PSED) and the investigation of certain key parameters.

4.1. Source term model Validation

Source term model validation involves comparison of model predictions of the time histories of pool area (radius) and evaporation rate against experimental measurements. Even though MEP contains a number of LNG spill tests for validation purposes, source term validation data are not available for these since they were conducted for other purposes other than to provide source term validation data. For instance, the Falcon series trials were conducted to investigate the effect of impoundment walls on a dispersing gas cloud, Coyote experiments were conducted to provide data for dispersion model validation and to study rapid phase transition, Shell Maplin sand trial was conducted to study combustion and dispersion. Thus the critical instrumentation to capture pool area and other parameters of interest for source term model validation were absent or given poor attention. A common approach therefore is to rely on other experiments (not included in the MEP) for which there exist adequate data for model assessment. Earlier research[119, 120] summarised a total of eleven LNG spills on water and six spills on land conducted up to 1983, but acknowledged that data for land spills are lacking. This includes all of the major large scale releases including the US Bureau of Mines test, Lawrence Livermore test and the Esso spill test. Notwithstanding that a substantial number of experiments have been performed, data on instantaneous pool radius and evaporation rate is rare [7]. The only data available appear to be that of Esso experiment. Therefore the Esso field trial has been adopted here for source model validation. A full description of the experiment is as provided in what follows.

4.1.1. The ESSO/API test

A series of LNG spill tests were performed by ESSO Research and Engineering Company at Matagorda Bay, Texas, under contract with the American Petroleum Institute in (API) in 1971.

Table 4-1: Summary of the ESSO experiments

Test no	Spilled Volume (m^3)	Ambient Temperature(K)	Spill duration (s)
1	0.78	24	-
2	0.73	24	5.6
3	0.84	25	5.8
4	0.93	26	5.2
5	0.93	29	-
6	0.79	29	-
7	0.79	28	7.0
8	7.12	29	25.0
9	7.42	24	25.0
10	5.22	20	21.0
11	10.22	27	35.0
12	0.93	25	6.2
13	0.93	25	6.3
14	0.93	25	6.7
15	2.50	25	12.0
16	7.57	18	28.0
17	8.36	17-18	31.0

The series consists of a total of seventeen experiments in which varying quantities of LNG were discharged into the Bay in order to measure downwind concentration profiles and determine the distance to the lower flammability limit. Full information about the conditions of the release, the spilled volume and release rate is as summarised in Table 4-1.Based on HSE report [7], data on the size of the pool were limited and attempts to measure it using thermistors were abandoned . As a result, the spreading rate on water was determined only from test 11, being the largest test as depicted in Table 4-1. For this test, the pool reached a stable diameter of 29m at about 24 seconds into the spill [7]. By assuming the pool diameter increases linearly with time, the UK HSE [7] fitted the pool diameter as a function of time as shown in equation(4-1):

$$d = kt \tag{4-1}$$

With k= 1.27mls. However, it is noteworthy to mention that the formulation above is only a curve fit to the spreading trend observed in test 11, hence it cannot be justifiably used as a source term model for other experimental scenarios.

4.1.2. Numerical Simulation in MATLAB

In the modelling process, the spreading relationship i.e. Equation (3-31) is used until the pool reaches a minimum stable pool thickness for which Hissong reported a value in the range 4.4mm to 6.7mm. Afterwards, the pool thickness is fixed to this minimum value and the pool radius is evaluated from the instantaneous pool volume. This process is continued until the volume remaining in the pool goes to zero, meaning that spillage has stopped and the pool has completely evaporated. To run the model, a number of input values are needed as initial conditions. This includes the total volume spilled, the height of the containment, the breach size and the simulation time step. For the present simulation, values of all the parameters (except the breach size) are obtained directly or derived from information summarised for Esso Experiments in Table 4-1. To obtain the breach size, a very intelligent technique is employed. This involves adjusting the breach size progressively until the reported spilled volume is released exactly within the reported spilled duration. The breach size at which this happens must be same as the experimental orifice size. This procedure has been found to be effective based on a blind trial performed for Coyote experiments in this study. For the time step, it has been observed that as the time-step is decreased progressively up to 0.1 seconds, the solution remains unchanging with further decrease in time step. With a time-step of 0.1 seconds, the complete execution of the code took approximately 5 seconds for ESSO (trial 11). This is a major breakthrough with similarity models compared to the more computationally tasking shallow layer models. It is also worthwhile to mention that the Euler first order scheme has been used for time integration of the spreading relationship as evident in equation (3-33). The second order Adams-Bashforth scheme was tested but it did not have any effect on the solution.

4.1.3. Result and discussion

Figure 4-1 compares ESSO data and the present model prediction of pool radius versus time for test 11.At the beginning and in the early stages of the spill, the pool radius increases rapidly as the cryogenic liquid spreads on the water surface.

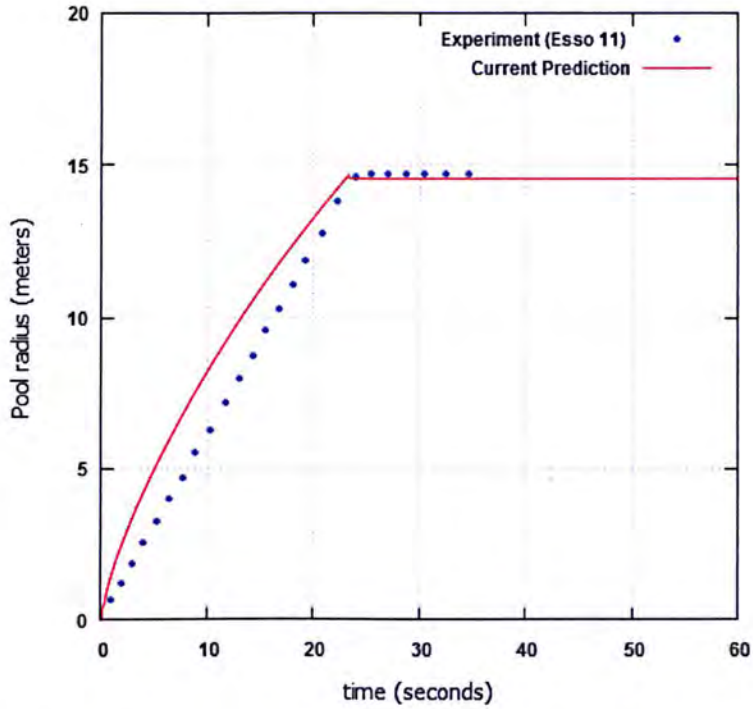

Figure 4-1:Esso test 11 radius data compared with current predictions

As the rapid spread continues, the pool size reaches a point where the spill rate balances out with the mass loss due to evaporation and the pool radius becomes fixed. The maximum pool radius was predicted as 14.9m, which is exactly the value estimated by the experiment. Predicted lifetime of the pool is about 60 seconds at which time the pool vanishes without shrinking. The reason being that inasmuch as the pool is still at its maximum size, the pool thickness and consequently the volume in the pool was decreasing and suddenly goes to zero. This immediately brings the pool size to zero as there is no volume to spread. Thus the present model captures the trend of the pool development and is in good agreement with experimental data. The slight discrepancy in the pool size in the early stage of the spreading is most likely due to friction between the spreading cryogen and the underlying water surface, the nature of which has been studied by Webber who derived a formulation for it. This aspect was not included in the present simulation, but it can potentially delay spreading and thereby bridge the slight discrepancy.

It is worthwhile to acknowledge that the integrity of the model need to be further assessed in some sense notwithstanding the paucity of source validation data. Thus, to compliment the validation study carried out in this section (based on Esso experiment), further assessment of the source term model will be performed as part

of the actual dispersion model validation in the immediate next section (section 4.2). This indirect validation will compare the experimental concentration profiles against those obtained using a model that incoporates a source term model (I-PSED) and one without source term model (conventional). The idea is to evaluate the effect of the inclusion and non-inclusion of the source term model and hence assess the integrity of the source term model developed. This assessment will be carried out in the case of point-wise and arc-wise concentration comparison of experiemental data against model predictions. For the achievement of this purpose, two different field scale experiments will be simulated (with and without source term model) and results compared against experiment as described in the section that follows.

4.2. Validation of the coupled (I-PSED) Model

The source term model developed in this study and validated in the proceeding section has been coupled to a dispersion model within the framework of OpenFOAM as described in chapter 3.This section presents a validation study aimed at assessing the integrity of the coupled model (I-PSED) model. The rationale behind I-PSED is to employ MATLAB to simulate the source term providing an input file which is fed into the dispersion model through the LNG inlet boundary. Thus the mass flow injected into the domain changes per time step to reflect the mass evaporation and pool radius supplied by the source term model.

4.2.1. Test-Case 1: Coyote LNG Spill experiments

Coyote series of experiments were conducted at China Lake, California in 1981 by Lawrence Livermore National Laboratory and the United States Naval Weapon Centre (NWC).The aim was to investigate vapour cloud dispersion, in addition to assess the extent of vapour cloud fires which could result from ignition of vapour clouds. The series consists of a total of ten experiments some of which involved the spill of LNG on water surface mimicking potential spill from large LNG ship tankers. During the LNG spill experiments, large quantities of LNG were spilled in a 58m diameter water test basin onto an immersed splash plate at shallow depth, aiming to limit the penetration of LNG into the water. The water surface was 1.5m below ground level. The experiment was heavily instrumented with sensors placed at downwind locations to measure LNG vapour concentration. Table 4-2 summarizes important data about the wind and LNG release conditions during the experiments.

Extensive details of the experiment including recorded data are available in the Goldwire et al[114], Koopman et al[117], and US Federal energy regulatory council (FERC) report [121].

Table 4-2: Summary of experimental conditions of Coyote trials

Test number	Wind speed (ms^{-1})	Temperature (^0C)	Spilled volume (m^3)	Spill rate (m^3/min)	Spill duration (s)
3	6.0	38.3	14.6	13.5	65
5	9.7	28.3	28.0	17.1	98
6	4.6	24.1	22.8	16.6	82

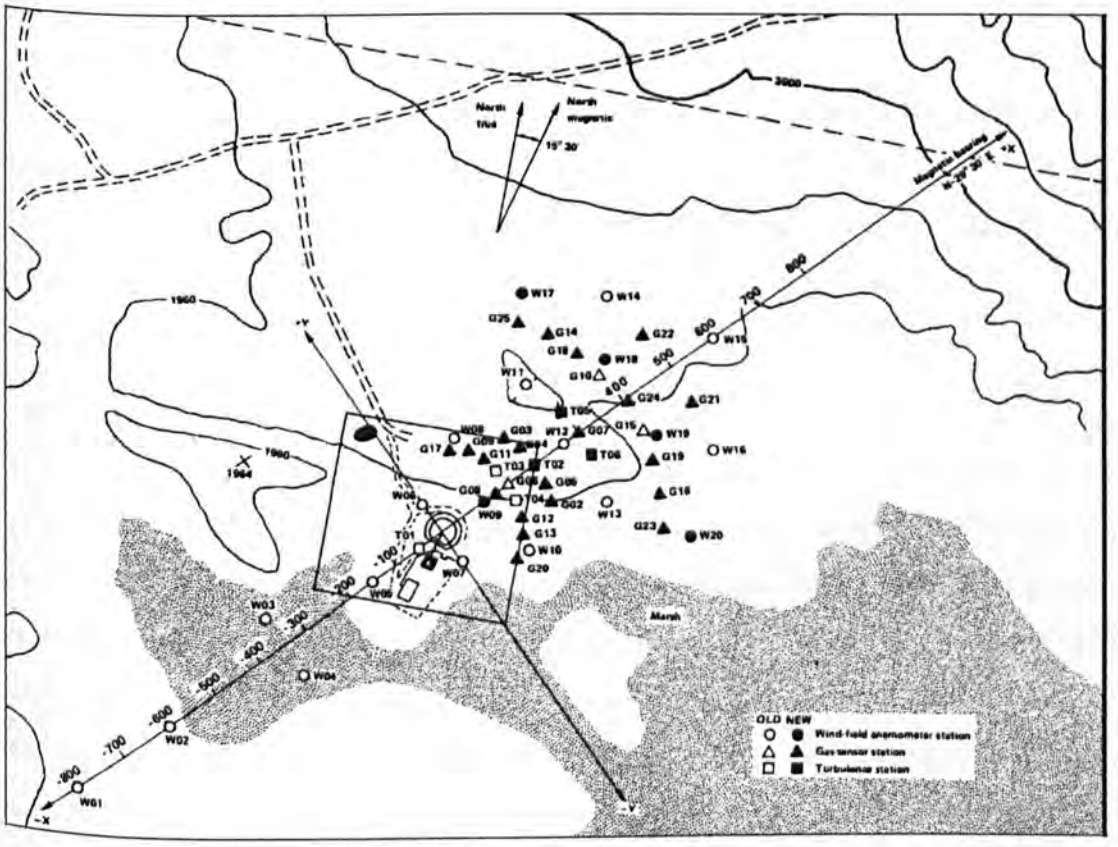

Figure 4-2: Coyote series test site[122]

The test was heavily instrumented to collect ambient data as well as gas concentration data. Gas concentration sensors were arrayed in arcs at downwind distances of approximately 140m, 200m, 300m, 400m and 500m from the spill center, see Figure 4-2 above. Extensive information about the precise location of all

the sensors measuring concentration is available in Goldwire et al [114].Other instruments used comprises of wind anemometers for wind field measurements and heat flux sensors. Wind field measurements were taken with the aid of a two-axis cup and vane anemometers located at 11 stations and at a height 2m above ground level. These were positioned both upwind and downwind unlike the gas sensors which were located only downwind of the spill center. Bi-vane anemometers were also installed to measure atmospheric turbulence, but the data captured was not provided by LLNL to the DoE for the database.

Coyote trial 3was performed under the most unstable atmospheric conditions of all the Coyote series of experiments, with average wind speed of 6.0m/s measured at 2m above the ground level, and category B-C stability condition .The total volume of LNG spilled was 14.6 m^3 at a spilled rate of13.5 m^3/min so that the spill lasted for approximately one minute and five seconds. The wind direction was 205 degrees from the true north giving a domain wind angle of +20°(see Figure 4-2). The ambient temperature during the test had an average value of 38.3 degree Celsius with just little fluctuations and the relative humidity was measured having a value of 11.3%. The ground surface roughness was 0.0002, and the Monin-Obukhov length was reported as -6.32. Coyote 3 was ignited at 99.7 seconds, hence all dispersion simulations must be terminated around this time.

Coyote trial 5 presents a unique scenario as it combine the highest wind speed, maximum volume spilled and the maximum spill duration of all the series as shown inTable 4-1. The test was conducted under a slightly unstable atmospheric condition (category C-D) and the wind speed was 9.7m/s at a height of 2m above the ground level. The spilled volume was 28m^3 at a spill rate of 17.1 m^3/min so that the spill lasted for about one minute and thirty eight seconds. The wind direction was 229 degrees from the true north giving a domain wind angle of -4° (see Figure 4-2). The ambient temperature during the test had an average value of 28.3 degree Celsius. The ground surface roughness was same as in Coyote 3 trial i.e. 0.0002 with a Monin-Obukhov length of -26.7. During the test, a large rapid phase transition occurred about 101 seconds into the test, followed by one of two smaller RPTs [117]. The cloud was ignited around 132.7 seconds.

Coyote trial 6was performed under the lowest wind speed of all the Coyote series, 4.6m/s, and the atmospheric condition was class D, indicting neutral condition. It involves a spill of a total of 22.8 m^3 of LNG at the rate of 16.6m^3/min so that the spill duration was about one minute and twenty two seconds. The wind direction was 220 degrees from the true north giving a domain wind angle of +5° (see Figure 4-2). The ambient temperature during the test had an average value of 24.1 degree Celsius. The roughness of the ground was 0.0002 and the Monin-Obukhov length was 73.6. The visible LNG vapour cloud, corresponding to 0.11 volume concentration was significantly wider than those of Coyote trials 3 and 5 and extended up to 60 m downwind of the spill. The cloud was ignited 108 seconds into the test at a distance of 79 m downwind of the spill center.

4.2.1.1. Simulation set-up in OpenFOAM

Simulation set-up in OpenFOAM follows the basic CFD procedure which consists of three major steps – creating the geometry and mesh, pre-processing (specification of boundary conditions etc) and solving (running the simulation).However, OpenFOAM is different in certain areas, hence OpenFOAM set up is described in more detail here before moving on to case set up for the Coyote experiments. In OpenFOAM, a simulation case must be enclosed in a folder called 'a case directory' which stores all the data required for a particular simulation in a number of subdirectories as shown in Figure 4-3 below.

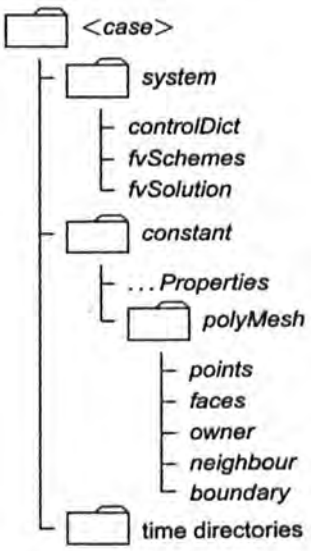

Figure 4-3: Schematic of case-set up in OpenFOAM

1) **System directory**: This directory holds files and folders in which parameters associated with the solution procedure are specified. It contains a file called *controldict* where run control parameter are specified, including simulation start/end time, time step and parameters for result data output. *FvSchemes* i.e. finite volume schemes where discretization schemes used in the solution are specified; and *FvSolution* i.e. finite volume solution where appropriate scheme and tolerances for solving the linear equations resulting from the discretization process is specified

2) **Constant directory**: This contains the full information about the case mesh in a subdirectory called *Polymesh,* but the mesh has to be created in OpenFOAM, or in third party package and then converted to OpenFOAM format as would be described later on for the Coyote series of experiments. Apart from the Polymesh directory, other subdirectories are present in the constant folder including the *transportProperties* which holds information about the thermophysical properties for the case in question and *turbulenceProperties* which holds information about the turbulence model.

3) **Time directories**: This directory contains subdirectories holding the data for the field variables involved in a simulation test case. The data that exist at this level include, a zero folder (corresponding to time zero) where the initial conditions and the boundary conditions must be specified and results written for subsequent time by OpenFOAM as the calculation progresses. It is worthwhile to mention that OpenFOAM field variables must always be initialized, even when the solution process does not strictly require it, as in steady-state problems. A name will be given to each time directory depending on the simulated time at which the data is written. For example before the start of the simulation (at zero time), the velocity and pressure fields are named 0/U and 0/p respectively and subsequent results for these variables are named as time/U and time/p (e.g. 20/U and 20/p).

4.2.1.2. Domain and mesh for simulating Coyote experiments

As mentioned earlier, OpenFOAM toolbox contains utilities for construction of geometry and mesh, and also allows the importation of mesh from other CAD tools. For the present study, the geometry was constructed and meshed in Gambit, and then converted into OpenFOAM format using the 'FluentMeshToFoam' command.

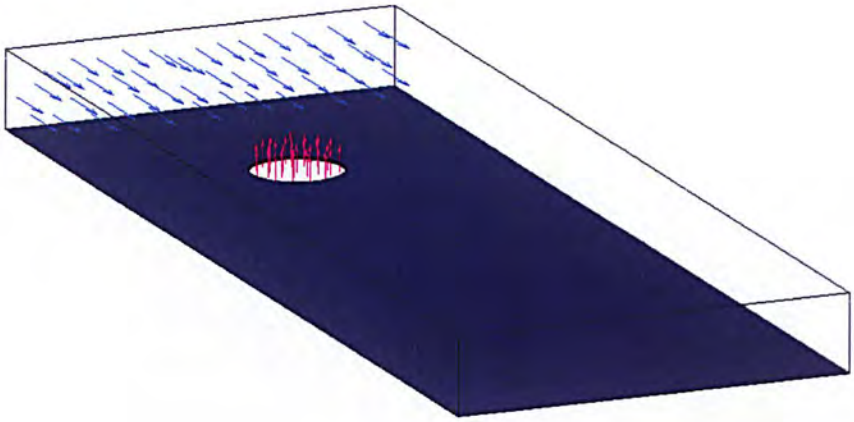

Figure 4-4: the Computational domain

The computational domain extended from -130 to 600m in the windward direction, from -200 to 200m in the crosswind direction and from -1.5 to 50m along the vertical height. The domain was discretized using hexahedral cells for optimal computational efficiency. The mesh was selectively refined in the region of the spill and close to the ground as shown in Figure 4-5, in order to improve accuracy in the region where mixing of air and LNG vapour initiates and in the near ground region where the heavy vapour cloud is expected to disperse. The minimum horizontal cell size was 0.1m and minimum vertical cell size of 0.45m .In the horizontal plane, the grid expands away from the spill area but in a systematic manner in order to maintain aspect ratio within reasonable limit($0.2 \leq$ aspect ratio ≤ 1).The mesh for the entire domain consisted of 706917 cells selected based on a sensitivity study carried out on four different grids which showed that the above mentioned number of grids represents a good compromise between accuracy and computational cost. Details of the grid sensitivity analysis are presented in the results section.

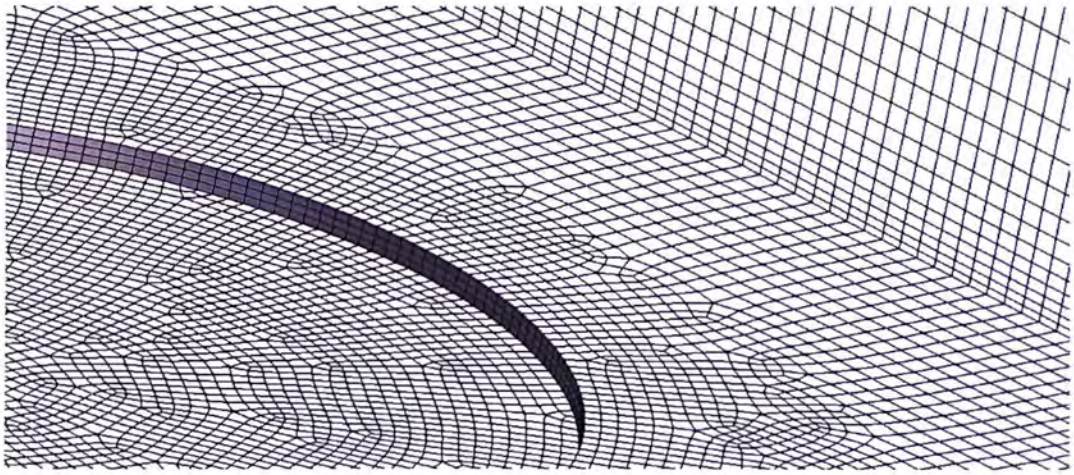

Figure 4-5: cut section of the computational grid for simulation of Coyote tests

4.2.1.3. Boundary Conditions

The boundary faces are illustrated in Figure 4-6 and consists of the ground, the LNG inlet, top, a wind inlet and the two side boundaries (side 1 and side 2). The side boundaries can be inlet or outlet depending on the wind angle. Therefore, in what follows, boundary conditions are discussed in general sense for all test cases apart from the side boundaries which depend on wind angle and the Wind inlet conditions which depend on stratification condition, hence vary between different cases and are therefore discussed separately for the three experimental trials (Coyote 3, 5 and 6).

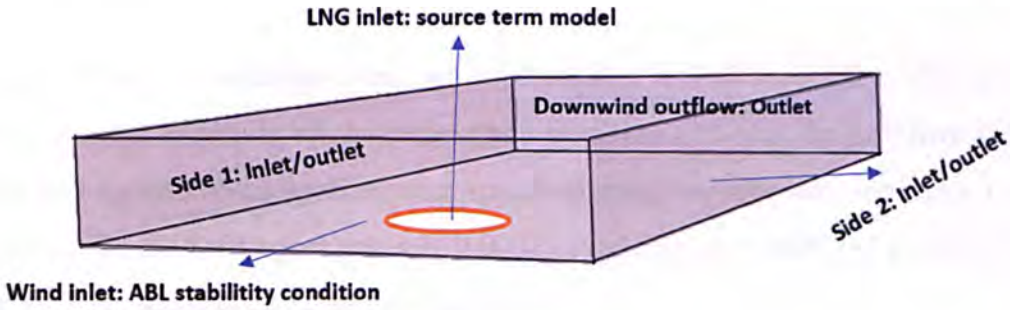

Figure 4-6: computational domain and boundary conditions

In OpenFOAM, a dirichlet or Von-Neumann's boundary condition must be specified on every boundary face for each field variable associated with a simulation case. One cannot specify for instance, a velocity inlet condition and expect OpenFOAM to work out the condition for pressure. Therefore, conditions have been placed on all

field variables in this present work to comply with OpenFOAM case set-up requirement as summarised in in what follows.

Top: the top boundary was specified with a typical outflow condition in which the pressure was set to ambient/atmospheric pressure (101325 Pa) and other variables are set to zero gradient

Downwind outlet boundary: at this boundary, fixed value was set for pressure (equal to atmospheric pressure) and other variables are specified as zero gradient.

LNG inlet: Here, the field variables were set to represent an inflow of LNG vapour into the domain. The source term model developed in Chapter 3 was calibrated with spill data from Coyote experiments and used to predict transient pool spreading and evaporation, providing two input files for upward directed velocity and radius in terms of time. At every time step, OpenFOAM reads the radius from the input data file (radius.dat) supplied by the source term model and compare it with the location of the cell faces on the LNG inlet boundary. If the cell face is wetted already, the CH4 mass fraction is set to unity, the temperature is set to 111K and an upward directed velocity is read from a data file (velocity.dat) provided by the source term model and specified over the corresponding instantaneous radius. Otherwise if the cell is not wetted, OpenFOAM sets the upward directed velocity to zero and CH4 mass fraction is set to zero and temperature is set to water surface temperature to indicate no LNG.

Ground: Here all variables were set to represent a wall boundary. This means velocity was set to zero in all three directions implying non-slip, the turbulent kinetic energy and its rate of dissipation were specified using smooth wall functions (since ground roughness for Coyote trials is 0.0002) available in OpenFOAM .Other field variables were then specified as zero gradient.

Wind inlet boundary: For this boundary, all of the field variables are specified to represent wind inflow into the domain. Therefore, an atmospheric boundary layer (ABL) profile was implemented for velocity, temperature, turbulent kinetic energy and its dissipation rate has been implemented based on Monin-Obukhov similarity theorem as discussed in chapter 3.Pressure has been set to zero-gradient at this boundary.

Side 1: For Coyote 3 and 6 where the wind angles are positive, this boundary is considered to be an outlet boundary, hence pressure was set to ambient value and all other variable set as zero gradient. For *Coyote 5*, this boundary is treated as an inlet due to the positive wind angle, hence an atmospheric boundary layer (ABL) profile based Monin-Obukhov theory was implemented for velocity, temperature, turbulent kinetic energy and its dissipation for unstable stratification condition under which the experiment was performed. Pressure was specified as zero gradient.

Side 2: For *Coyote 3*, this boundary is treated as an inlet due to the positive wind angle, hence an atmospheric boundary layer (ABL) profile based Monin-Obukhov theory was implemented for velocity, temperature, turbulent kinetic energy and its dissipation for unstable stratification condition under which the experiment was performed. For *Coyote 6*, the boundary is again treated as an inlet due to the positive wind angle, but the stability condition was neutral. Therefore, atmospheric boundary layer (ABL) profile based Monin-Obukhov theory was implemented for velocity, turbulent kinetic energy and its dissipation rate; but not temperature. A constant value was set for the temperature equal to the ambient conditions and pressure is specified as zero gradient. For Coyote 5 where the wind angle is negative, this boundary is considered to be an outlet boundary, hence pressure was set to ambient value and all other variable set as zero gradient.

4.2.1.4. Solver set up

As mentioned earlier, setting up of the solver is done within the *fvScheme* and *fvSolution* which are subdirectories of the system directory in OpenFOAM. The fvScheme holds information about the settings for integration of the time derivative, the divergence (convective) terms, the gradient terms and the laplacian (diffusive) terms. In all simulation runs carried out in this study, the transient terms are treated using the Euler Implicit scheme which guarantees bounded solution and is not susceptible to instabilities due to Courant Fredrick Lewis Condition. For all convection terms, the total variation diminishing (TVD) has been used and for the laplacian (diffusion) and gradient terms, the second order accurate central differencing scheme has been used.

FvSolution is the subdirectory where information about the solution method for the linear equations resulting from discretization as well as the pressure-velocity

coupling method is specified. Here, the preconditioned conjugate gradient (PCG) scheme preconditioned with diagonal incomplete-Cholesky (DIC) was specified for the pressure and density equation. For velocity, sensible enthalpy, turbulent kinetic energy and its dissipation rate, the preconditioned bi-conjugate gradient (PBiCG) solver preconditioned with diagonal incomplete-Cholesky (DIC) has been used. Pressure-velocity coupling has been achieved using the PIMPLE algorithm.

4.2.1.5. Running the simulation

Simulation of each test case was carried out in two interconnected steps. First the source term model is calibrated using the spill data reported for the experimental case being simulated, in order to determine the source term to be input into I-PSED model. The second step in the simulation, process involves the prediction of the actual atmospheric turbulent dispersion. In the actual simulation, the simulation proceeds for hundreds of seconds with the pool radius set to zero so that no LNG is being released into the domain. This is intended to achieve a fully developed wind profile which serves as the initial condition for the simulation, hence guarantee that the LNG will be released into the right kind of environment. After the wind flow field has been established, the actual LNG dispersion simulation begins hence instantaneous pool radius and upward directed velocities supplied from the source term model are read from an input file to define the source term. The time-step for all transient run was set to depend on the courant number which was maintained below unity for all simulations. Due to high computing requirement of the simulations in terms of computational time, the execution was done in parallel on the HPC cluster of the Kingston University London. The complete execution for the transient dispersion simulation required about 5.5 hours real time using 64 cores on the HPC cluster. The validation process starts with a grid sensitivity study as presented in the section that follows.

4.2.1.6. Grid sensitivity Analysis

In order to ensure the solution is independent of the grid, simulations have been performed starting with a coarse grid and refining progressively until further refinement does not have significant effect. Four different grids of number of cells: 176205, 460485, 706917 and 1192077 cells were tested.

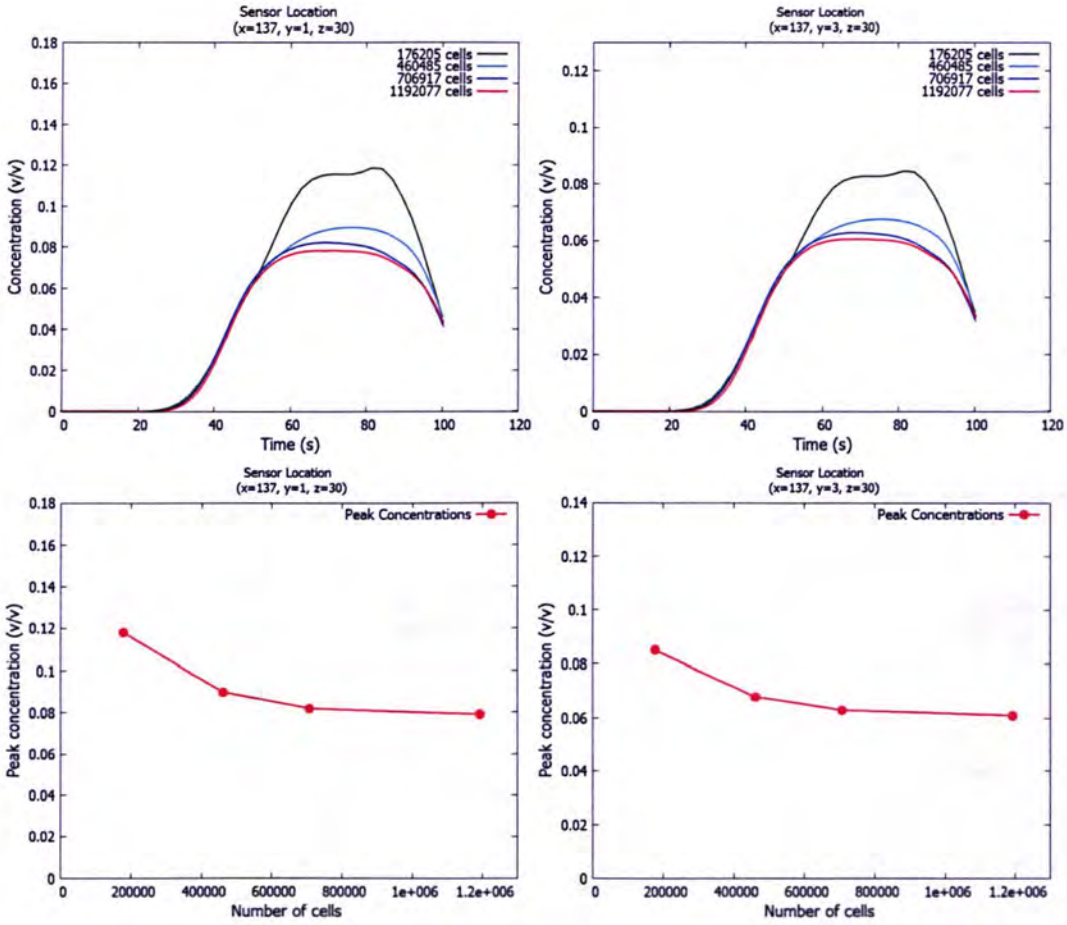

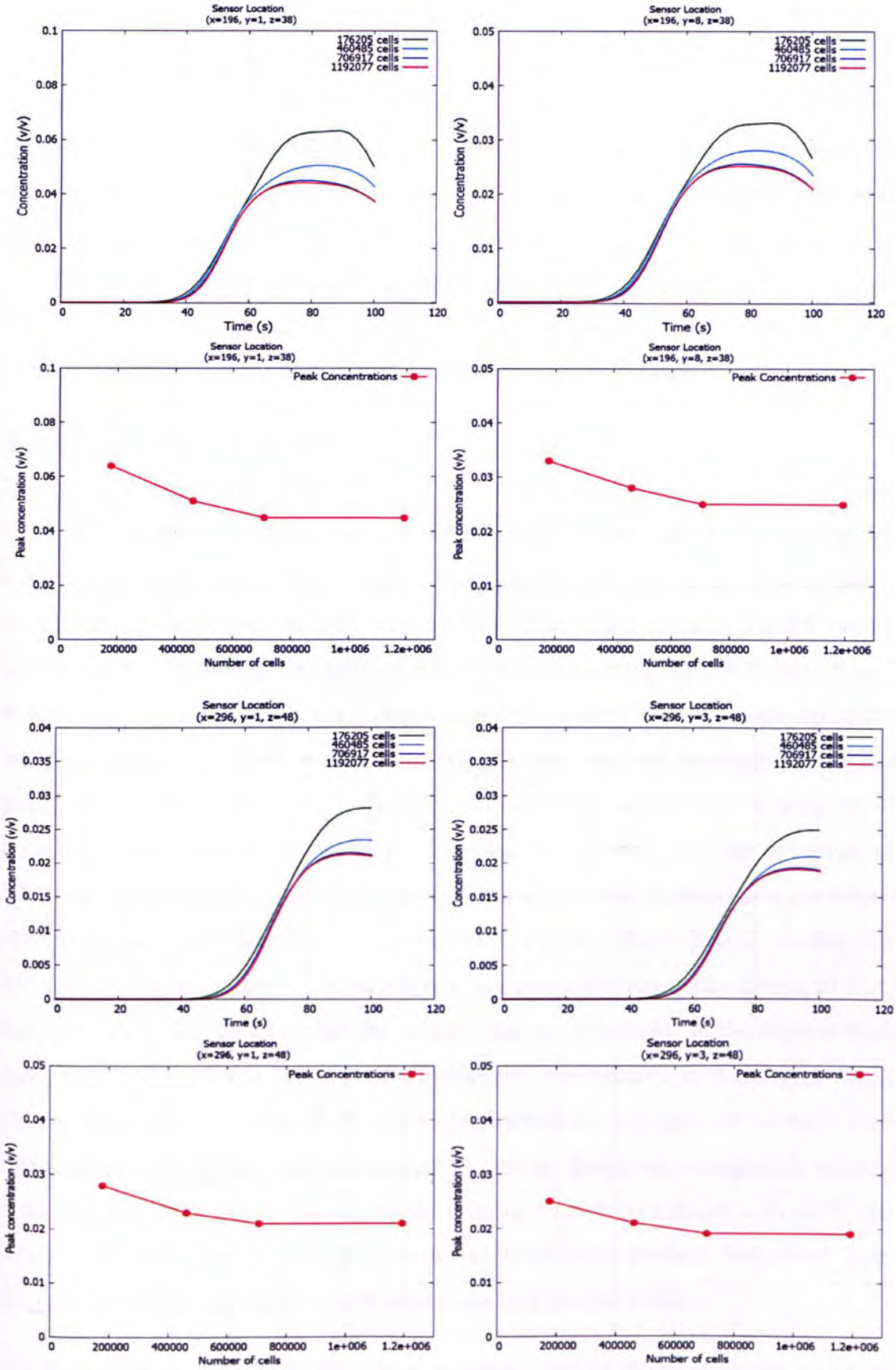

Figure 4-7: Concentration time histories and corresponding peak concentrations obtained by progressively increasing the number of cells

The concentration profiles and the corresponding maximum (peak) concentrations presented in Figure 4-7 above for different cell sizes shows how the solution responds to increase in the number of cells. As it is evident from the plots, increasing the number of cell from 706917 to 1192077 does not introduce significant change in the time histories of the concentration. In fact, the maximum change recorded was less than 4% at sensor location (137, 1, 30).Thus, the increase from 706917 to 1192077 is not worth the additional computational expense, prompting the choice of 706917 cells for the actual simulations. Further details about the chosen grid has been presented elsewhere in section 5.2.1.2 i.e. Simulation set-up.

4.2.1.7. Simulation results

Using the optimum grid obtained from the mesh sensitivity analysis, the Coyote LNG spill experiments have been simulated. The Coyote series consists of ten experiments out of which four involves the release of LNG. However, data for model set-up and validation are available only for three of the trials (trials 3, 5 and 6) which are included in the Model Evaluation Protocol for validation purposes. Coyote trial 7 is not included in the MEP. The Coyote series of experiments have been simulated using the current (I-PSED) model and using the conventional approach i.e. a fixed pool radius and evaporation rate. This is to critically evaluate the relative integrity of both approaches in predicting events following the release of large quantities of LNG. In compliance to MEP, both point-wise and arc-wise comparisons have been carried out and results obtained are as presented in what follows. In trial number 3 as well as all other tests, sensors were arrayed in arcs at different radius measured from the spill centre. By including all the sensors that were included in the experimental trial, it has been possible to predict the maximum concentration over each arc radius (140m, 200m, 300m, 400m and 500m). Experimental arc wise data are normally time averaged by applying long time averaging as well as short time averaging in order to smoothen out fluctuations, hence obtain a more reliable maximum over each arc. Thus, a common practise during arc-wise validation is to perform both short time-averaged and long-averaged comparisons as recommended in MEP.

An illustration of I-PSED prediction of arc-wise concentrations is shown in Figure 4-8 which is a steady state plume for test Coyote 3 at time 80 seconds from the beginning of the spill on a horizontal plane at 1 meter elevation.

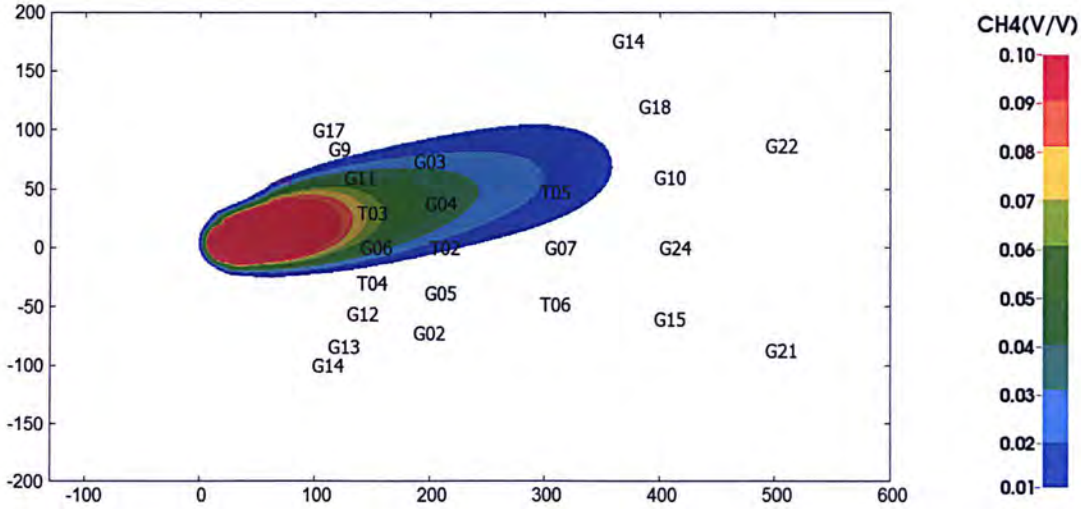

Figure 4-8: Steady state plume for test Coyote 3 showing cloud encounter with the sensors at time 80 seconds from the start of the spill and at 1m elevation

The sensors are located and annotated same as in the experiment [121].As one would expect, the concentrations are higher in the near field and reduces as the cloud proceeds downwind due to mixing with fresh air. The concentration levels in the near field region are within the flammability range of LNG vapour suggesting that a source of ignition in this region would result to fire and possibly explosion. The region of concern extends from the spill centre to a distance of about 200 meters beyond which the concentration has dropped well below the flammability limit. Also, it can be seen that the direction of motion of the cloud reflects wind direction. This is not unusual considering that the experiment and hence the simulation was carried out under medium to high wind speed condition.

Figure 4-9 gives time averaged maximum arc-wise concentration predicted using current (I-PSED) model and those predicted using conventional approach compared against experimental data. As can be readily seen in the short-time averaged plot , the maximum arc-wise concentrations predicted using I-PSED model and those of conventional model are comparable at most downwind locations. However the long time-averaged comparison clearly puts the current model (I-PSED) ahead of the conventional approach as using the conventional approach led to over-priction of maximum concentrations at most downwind locations.

In addition to the visual correlations between the predicted and measured maximum arc-wise concentrations, the percentage errors associated with the two models (I-PSED model and Conventional model) have been evaluated based on equation (4-2). In the equation,X_p stands for the predicted maximum arc-wise concentration at a specific arc radius (downwind distance) and X_M stands for the corresponding measured maximum arc-wise concentration.

$$\frac{X_P - X_M}{X_M} \times 100 \qquad (4\text{-}2)$$

The analysis shows that the I-PSED predictions are within 27% at most of the arc-radius evaluated (for 7 out of all 10 arc radii) while the predictions with the conventional model are within 36% spread around the measured values for most of the arcs considered (6 out of all 10 arc radii). The ten arcs comprises of five arcs each for long time-averaged and short time-averaged concentrations. Full calculation results have been included appendix B.

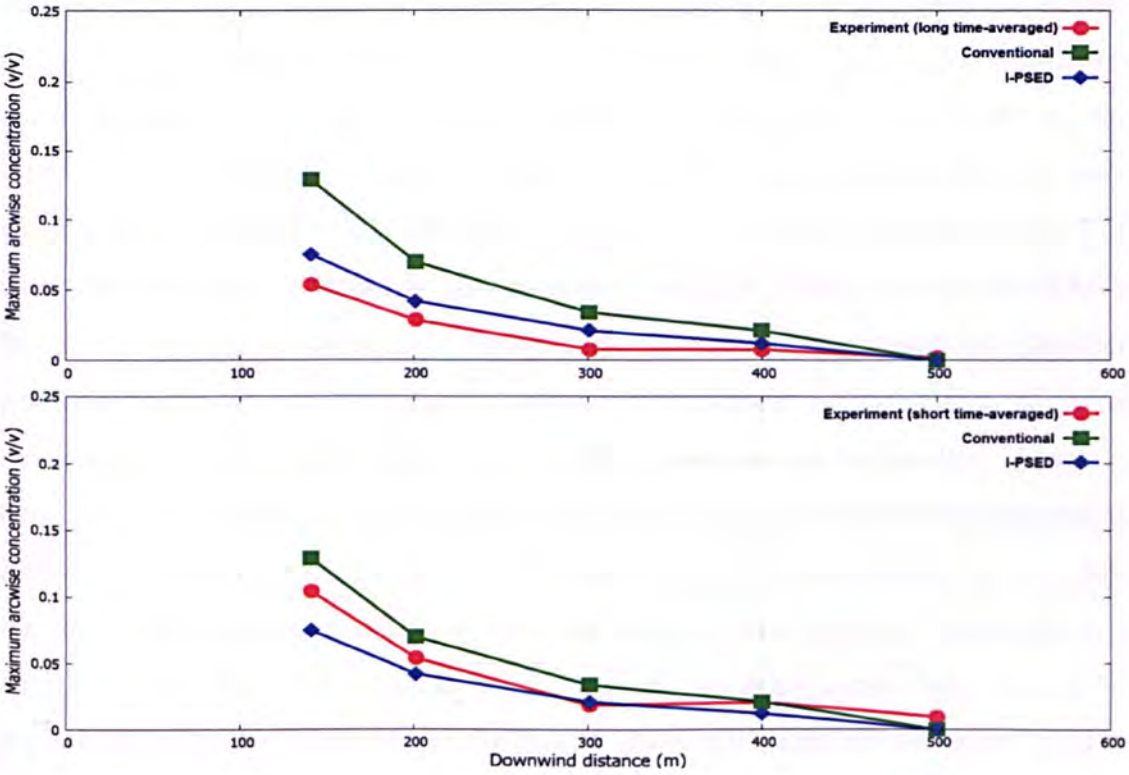

Figure 4-9: Time-averaged maximum concentration for Coyote trial 3 compared with predicted maximums over each arc.

Figure 4-10 to Figure 4-23 show point-wise comparison of the concentration profiles predicted using current approach (I-PSED) and those predicted using conventional approach at several sensor locations for test Coyote 3. While both models can be said to be conservative in predicting the concentration profiles, the current approach yielded results which are in better agreement with experimental data. As one can readily see, the conventional approach over-predicted concentrations during most of the dispersion period. The plots also reveal the integrity of the current approach in predicting the arrival time of the cloud. At all sensor locations, the arrival time predicted using I-PSED model is very close to the experimental values. With conventional approach, much earlier arrival time is predicted at all sensor locations. This is most likely due to the comparatively large mass flow rates released from the outset of the dispersion process following the assumption of spill rate being equal to the evaporation rate which underlies the conventional model.

From a quantitative standpoint, both models performed relatively well as evident from the plots. However, there exist a level of qualitative difference between predictions and experimental records as the wiggles (fluctuations) in concentration are not captured in current predictions. This is a typical problem with the RANS turbulence model which has been utilised in the present study. Large-eddy simulation (LES) approach is expected to capture fluctuations in concentrations. However, the large domain associated with atmospheric dispesion makes the use of LES non-plausible as this will result in incredibly large number of cells requiring a level of computational power which is not currently available. Thus, the use of RANS turbulence modelling approch is unavoidable in dispersion simulations. Another possible cause of the non-capture of the fluctuations is the effect of wind meandering. In real situations, wind changes direction intermittently. However, simulations rely on field measurements of wind direction which is mostly reported as an average value as was the case in this present study. Even in situations where time-varying wind direction data is available, the data is taken from an instrument at a location where the wind inlet can not be realistically positioned. Thus, the use of reported average wind direction in the present study is thought to have contributed to the qualitatitive descrepancy between predicted results and experimental data

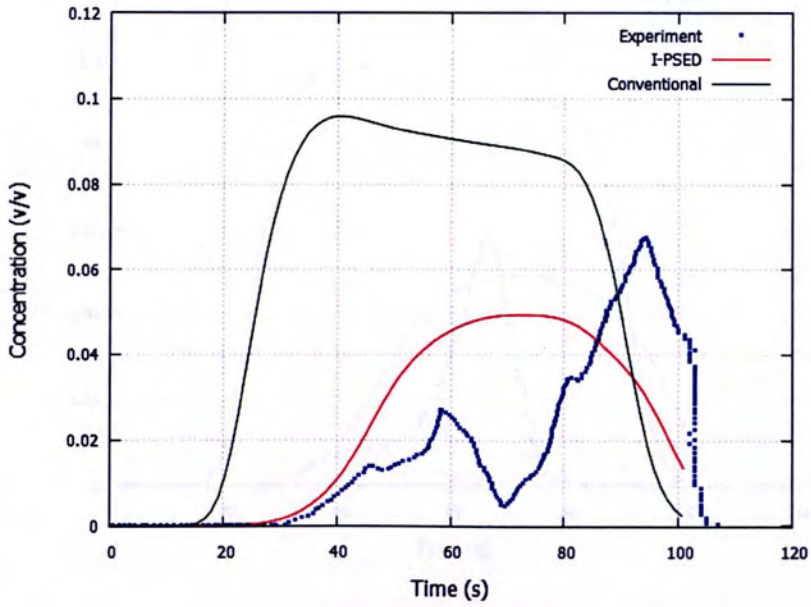

Figure 4-10: Current (I-PSED) model prediction of concentration profile compared with predictions using conventional approach and with experimental data for test coyote 3 for sensor G11 at location x=126m, y=1m and z=60m

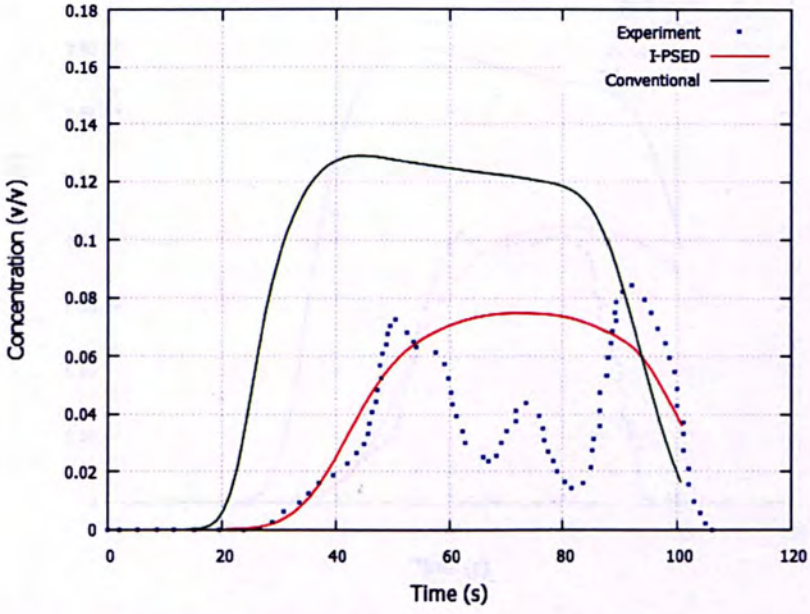

Figure 4-11: Current (I-PSED) model prediction of concentration profile compared with predictions using conventional approach and with experimental data for test coyote 3 for sensor T03 at location x= 137m, y=1m and z=30m

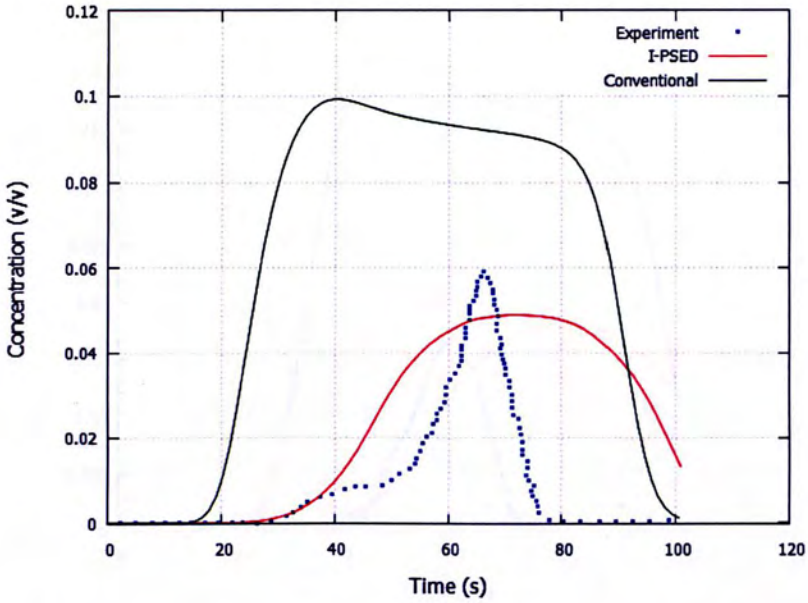

Figure 4-12:Current (I-PSED) model prediction of concentration profile compared with predictions using conventional approach and with experimental data for test coyote 3 for sensor G06 at location x=140m, y=1m and z= 0m

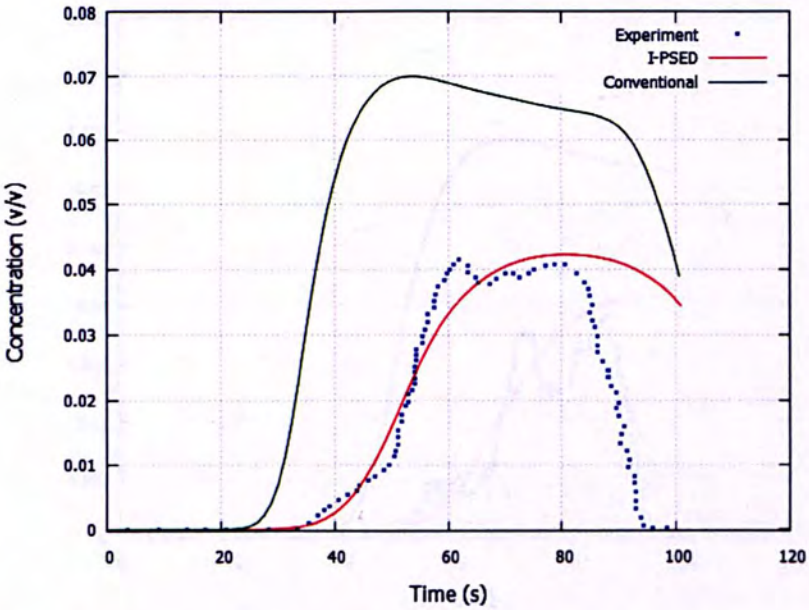

Figure 4-13: Current (I-PSED) model prediction of concentration profile compared with predictions using conventional approach and with experimental data for test coyote 3 for sensor G04 at location x=196m, y=1m and z= 38m

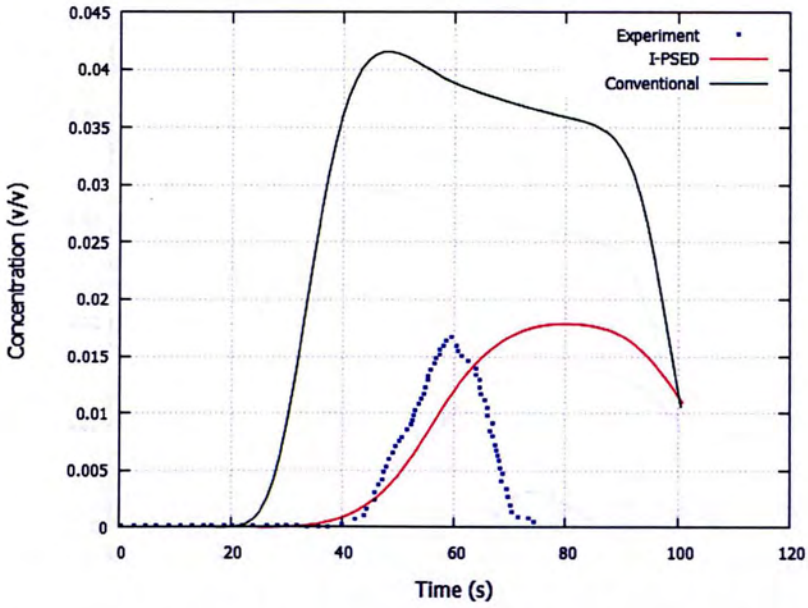

Figure 4-14: Current (I-PSED) model prediction of concentration profile compared with predictions using conventional approach and with experimental data for test coyote 3 for sensor T02 at location x=200m, y=1m and z= 0m

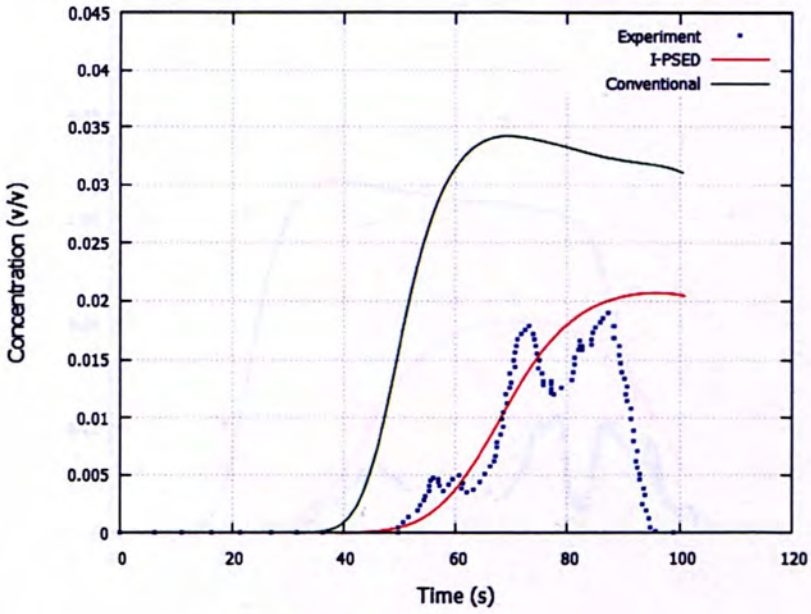

Figure 4-15:Current (I-PSED) model prediction of concentration profile compared with predictions using conventional approach and with experimental data for test coyote 3 for sensor T05 at location x=296m, y=1m and z= 48m

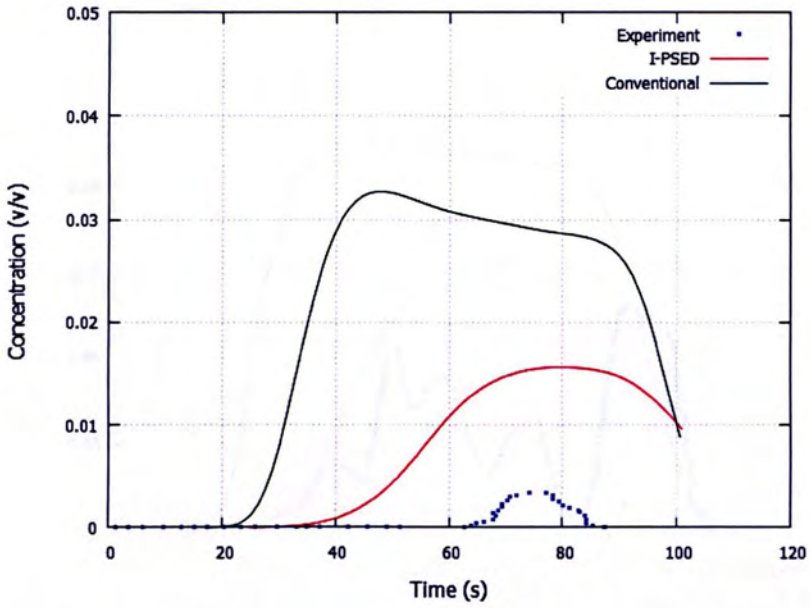

Figure 4-16: Current (I-PSED) model prediction of concentration profile compared with predictions using conventional approach and with experimental data for test coyote 3 for sensor G07 at location x=300m, y=3m and z= 0m

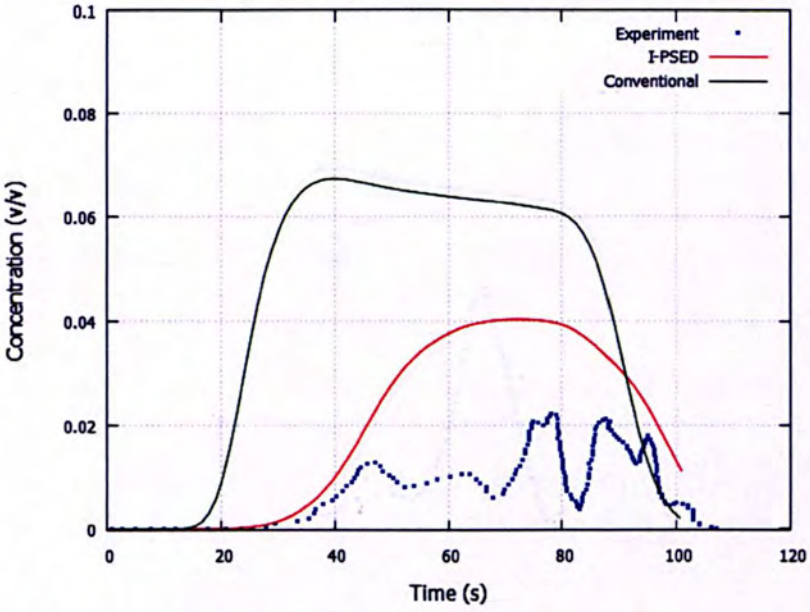

Figure 4-17:Current (I-PSED) model prediction of concentration profile compared with predictions using conventional approach and with experimental data for test coyote 3 for sensor G11 at location x=126m, y=3m and z= 60m

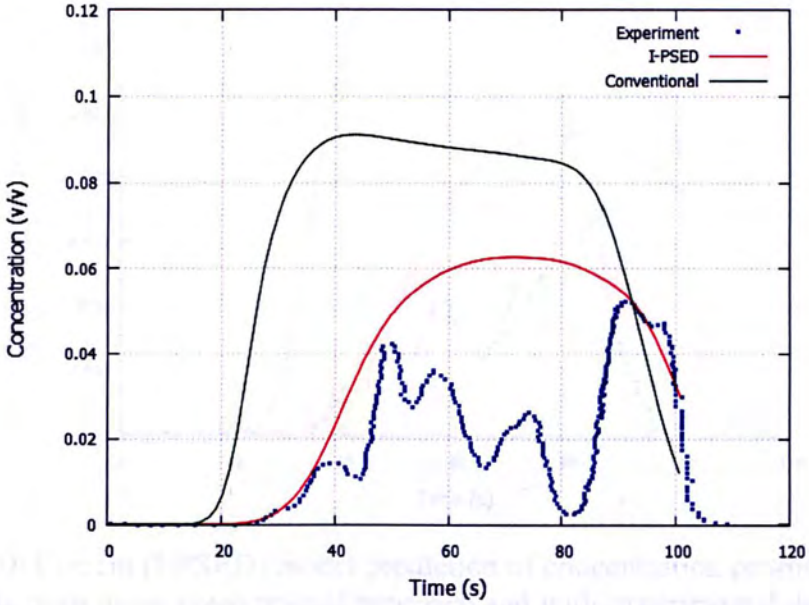

Figure 4-18: Current (I-PSED) model prediction of concentration profile compared with predictions using conventional approach and with experimental data for test coyote 3 for sensor T03 at location x=137m, y=3m and z= 30m

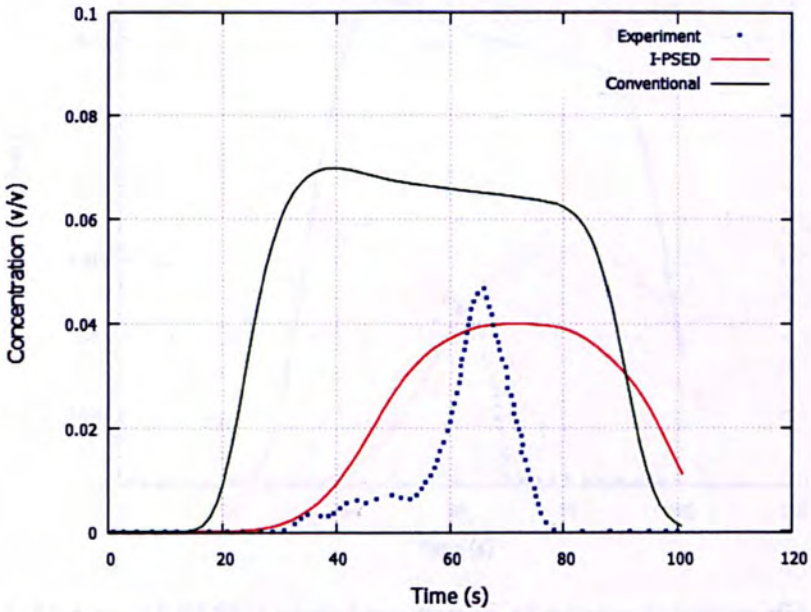

Figure 4-19: Current (I-PSED) model prediction of concentration profile compared with predictions using conventional approach and with experimental data for test coyote 3 for sensor G06 at location x=140m, y=3m and z= 0m

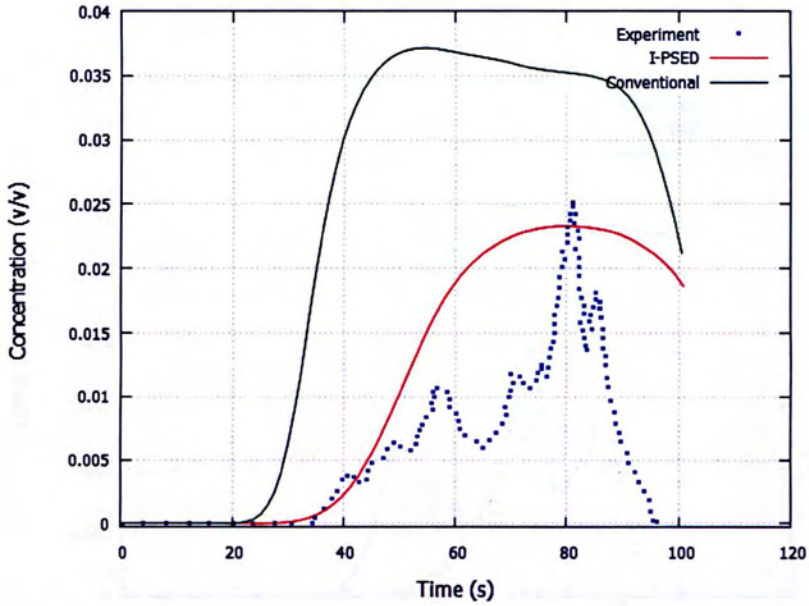

Figure 4-20: Current (I-PSED) model prediction of concentration profile compared with predictions using conventional approach and with experimental data for test coyote 3 for sensor G04 at location x=196m, y=8m and z= 38m

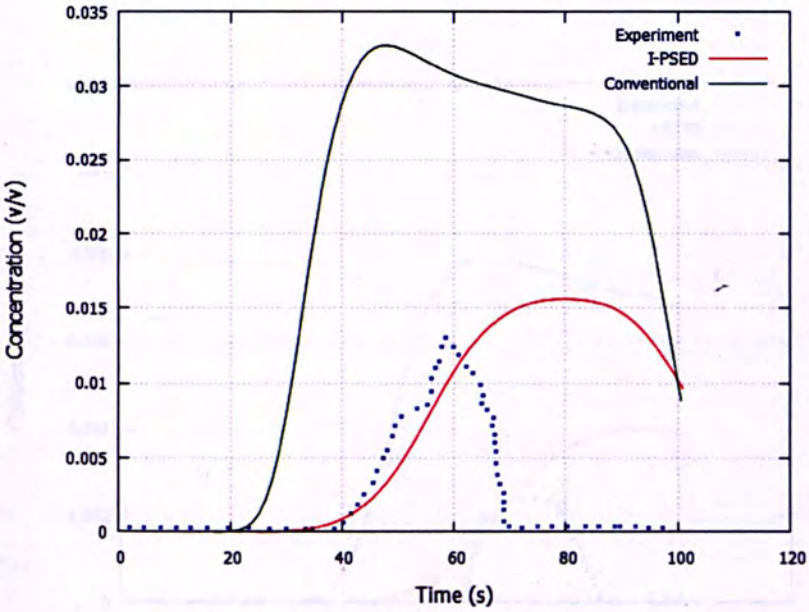

Figure 4-21: Current (I-PSED) model prediction of concentration profile compared with predictions using conventional approach and with experimental data for test coyote 3 for sensor T02 at location x=200m, y=3m and z= 0m

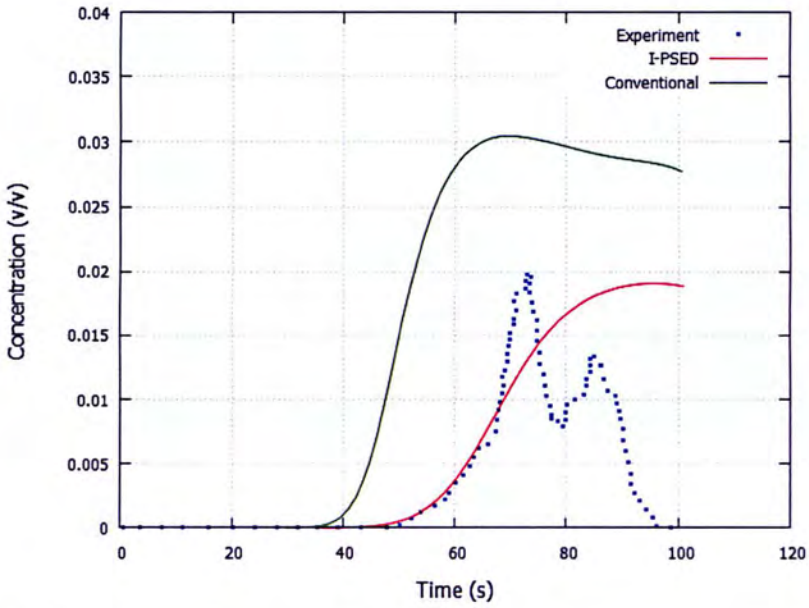

Figure 4-22: Current (I-PSED) model prediction of concentration profile compared with predictions using conventional approach and with experimental data for test coyote 3 for sensor T05 at location x=296m, y=3m and z= 48m

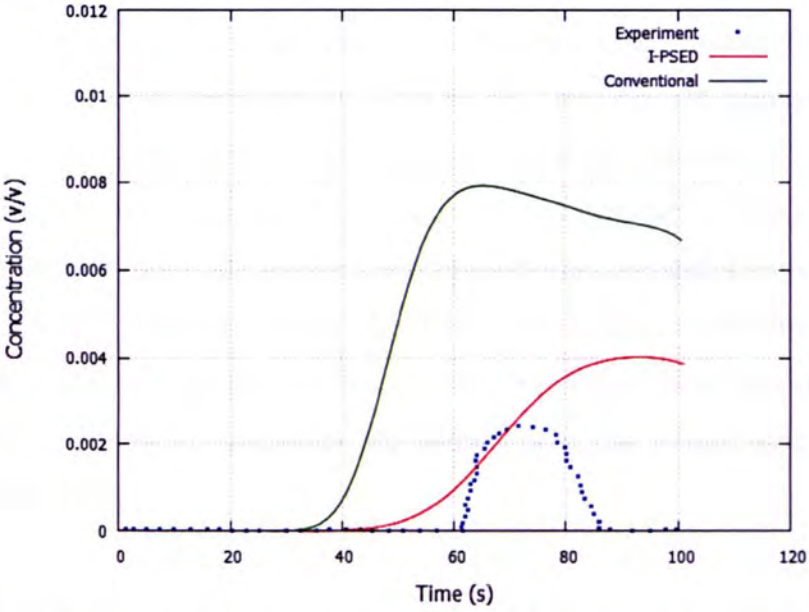

Figure 4-23: Current (I-PSED) model prediction of concentration profile compared with predictions using conventional approach and with experimental data for test coyote 3 for sensor G07 at location x=300m, y=8m and z= 0m

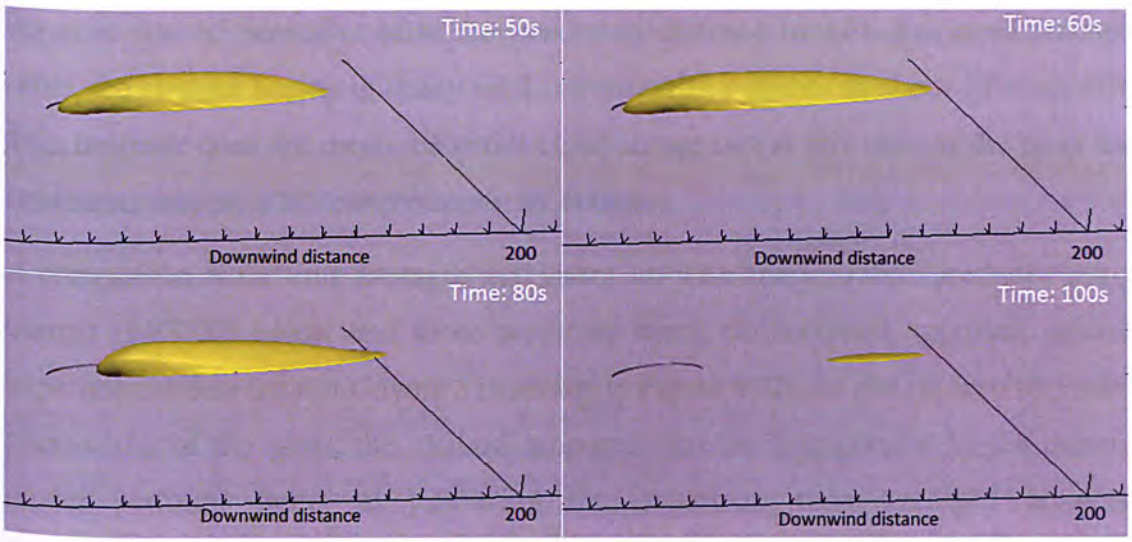

Figure 4-24: Snapshots of LFL contours at different moments for test Coyote 3.

In addition to the point-wise and arc-wise validation recommended by MEP, the maximum distance to the lower flammability limit has become a critical parameter in the LNG vapour dispersion modelling community for the evaluation of model performance. This is generally referred to as the exclusion distance or exclusion zone. Simply put, it is the area within which the gas concentrations are up to the lower flammability limit of LNG vapour (5%) and therefore ignition could lead to catastrophic events like fire and explosion. Federal Regulations (49 CFR 193) require that applications for onshore facilities demonstrate that hazards created in event of spill will not span beyond the area under the control of the terminal operator. Thus, the maximum distance to the LFL has become an important element of risk assessment in the LNG industry and in model assessment. Figure 4-24 shows snapshots of plots contoured using the LFL (5% concentration by volume) at different times, highlighting the maximum distance to the LFL, as obtained using the current model. Only four snapshots are shown here but a full time history has included appendix B.

As can be readily seen in the snapshots, the predicted maximum distance to LFL is about 203m from the centre of the spill. This is in very good agreement with the experimental value (210m) for this trial as reported by FERC[121].Also, it can be readily seen that this maximum distance was reached at about 80 seconds from the start of release which entails 15seconds after the release has stopped, note the release

duration was 65 seconds. After the maximum distance to LFL has been reached (80s), the contour begins to decay until it eventually vanishes at about 110 seconds. This however does not mean the entire cloud disappears at this time as the plots are contoured only with 5% concentration by volume.

A comparison of the time averaged maximum arc-wise concentration predicted using current (I-PSED) model and those predicted using conventional approach against experimental data for test Coyote 5 is shown in Figure 4-25. As can be seen by visual comparison of the plots, the method proposed here as incorporated in the current model performs better at predicting the maximum time averaged arc-wise concentrations compared to the conventional approach.As in test Coyote 3, the error associated with the predictions of the maximum arc wise concentrations have been evaluated. Based on the results of the evaluation, errors associated with I-PSED predictions are within 25% at most of the arc-radius evaluated (for 7 out of all 10 arcs) while the predictions with the conventional model is within 75% for most of the arcs (for 7 out of all 10 arcs).Full calculation results have been included in Appendix B.

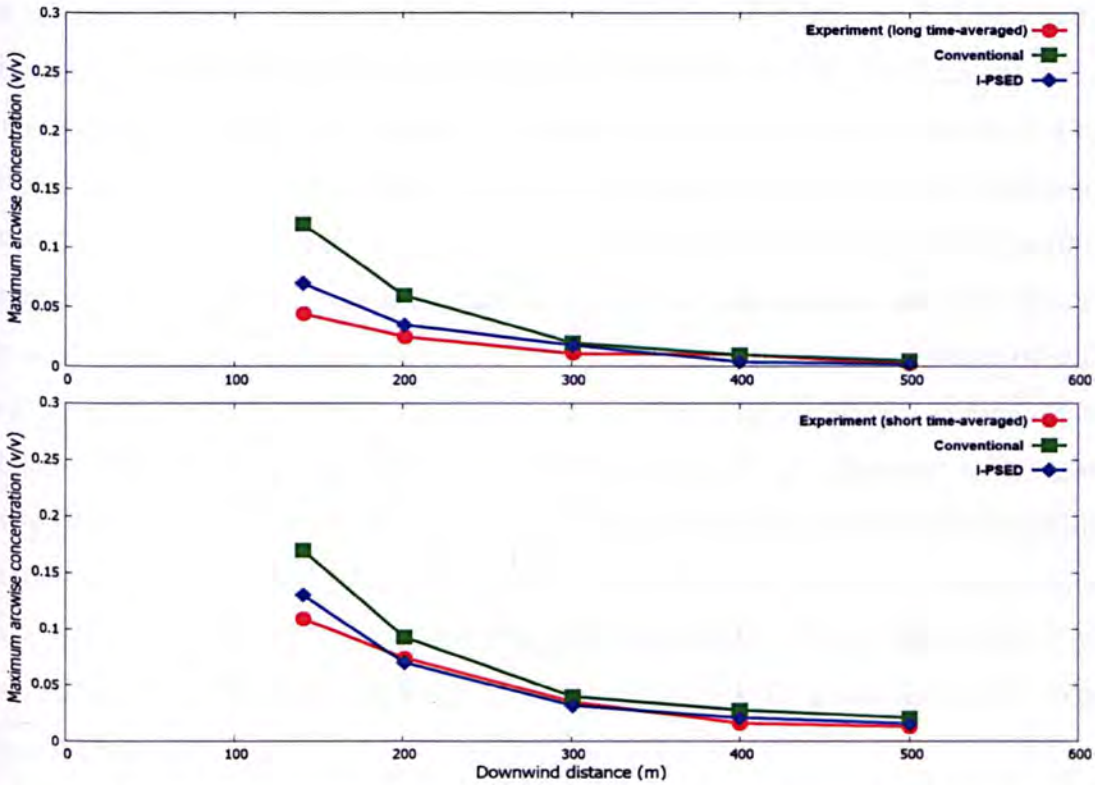

Figure 4-25: Time-averaged maximum concentration for Coyote trial 5 compared with predicted maximums

Figure 4-26 to Figure 4-32 present point-wise comparison of the concentration profiles predicted using current approach (I-PSED) and those predicted using conventional approach for test Coyote 5. It can be seen that both models are quantitatively conservative in predicting the concentration time histories, but similar to what was observed in trial 3, the current approach provides a better prediction of the cloud arrival time. Furthermore, the conventional approach over-predicted concentrations at most of the monitoring points as evident in the plots. The models are able to reproduce experimental data for most of the sensor positions simulated. However, for sensors located at large crosswind distances such as G04 and T05, the curent model underpredicted concentrations. Clearly, the plume did not hit these sensors since average wind direction has been used for the simulations in the absence of adequate detail to incioporate time varying wind direction changes. Predictions could be improved for these locations through a better representation of the meandering wind.

Similar to the trend observed for Coyote trial 3, the models (I-PSED and conventional) failed to capture the fluctuations in concentration as observed in the experiment. Instead, average concentreation profiles are predicted at all times during the period simulated. This is a typical problem with RANS model as the governing equations are time averaged thereby smoothen out any fluctuations. The use of LES model will obviously better reproduce these fluctuations. However, LES turbulence model is not suitable for such simulations as atmospheric dispersion which requires large domain. For large domains used in dispersion simulation, the level of cell resolution required for LES simulation will mean incredibly large number of cells which can not be handled using currently available computational power. Even though there exist super computers for such simulation, the additional information (wiggles) captured does not justify the computational expense. Based on the ongoing, RANS models provide a good compromise in terms of accuracy and computaional cost and hence are widely adopted in dispersion simulation. This curent study is not an exception as predicted average concentrations are in good agreement with experimental data.

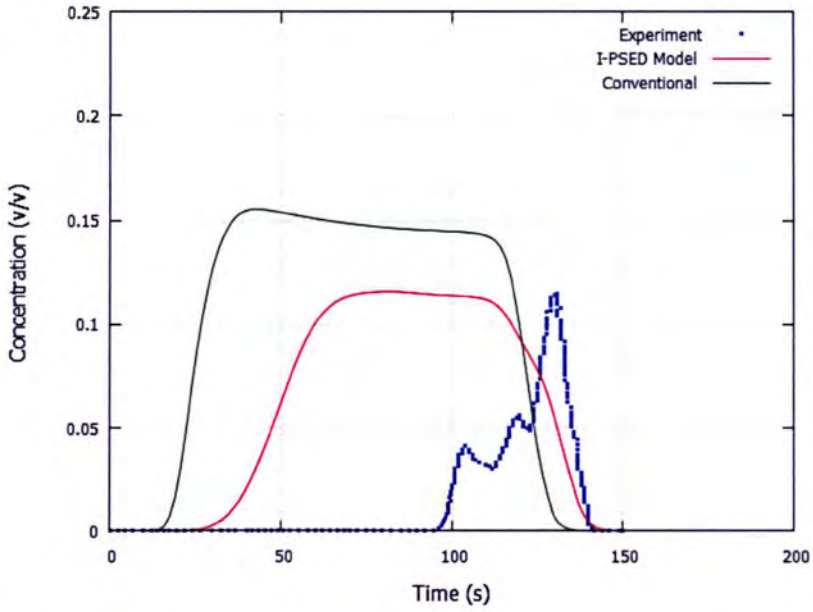

Figure 4-26: Current (I-PSED) model prediction of concentration profile compared with predictions using conventional approach and with experimental data for test coyote 5 for sensor T04 at location x=137m, y=1m and z= -30m

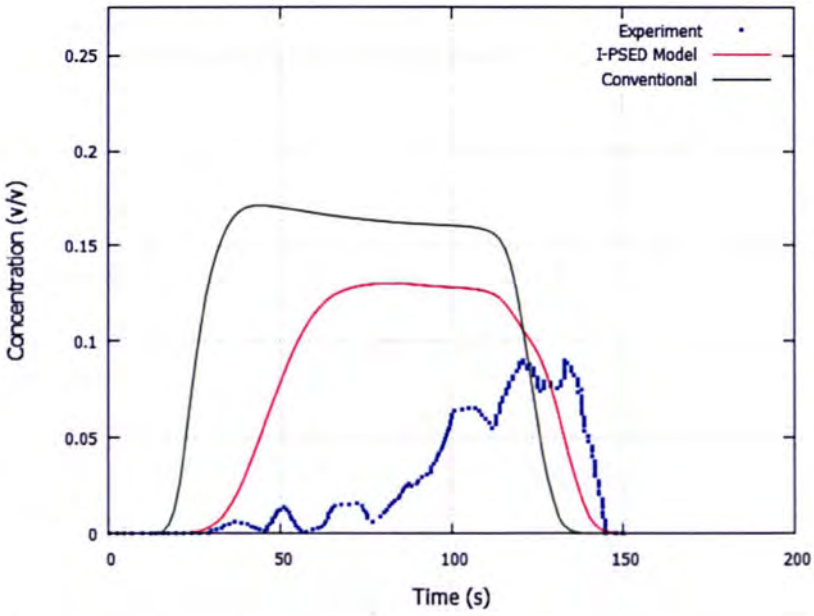

Figure 4-27: Current (I-PSED) model prediction of concentration profile compared with predictions using conventional approach and with experimental data for test coyote 5 for sensor G06 at location x=140m, y=1m and z= 0m

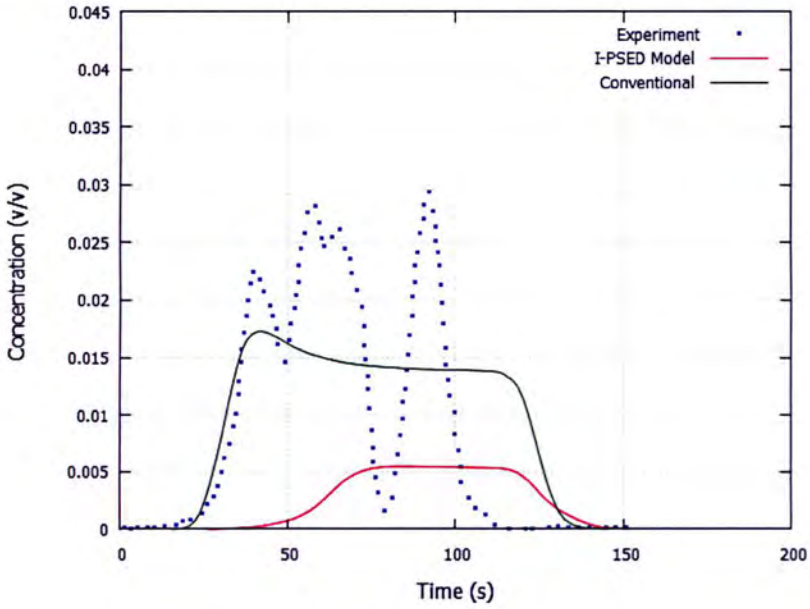

Figure 4-28: Current (I-PSED) model prediction of concentration profile compared with predictions using conventional approach and with experimental data for test coyote 5 for sensor G04 at location x=196m, y=1m and z= 38m

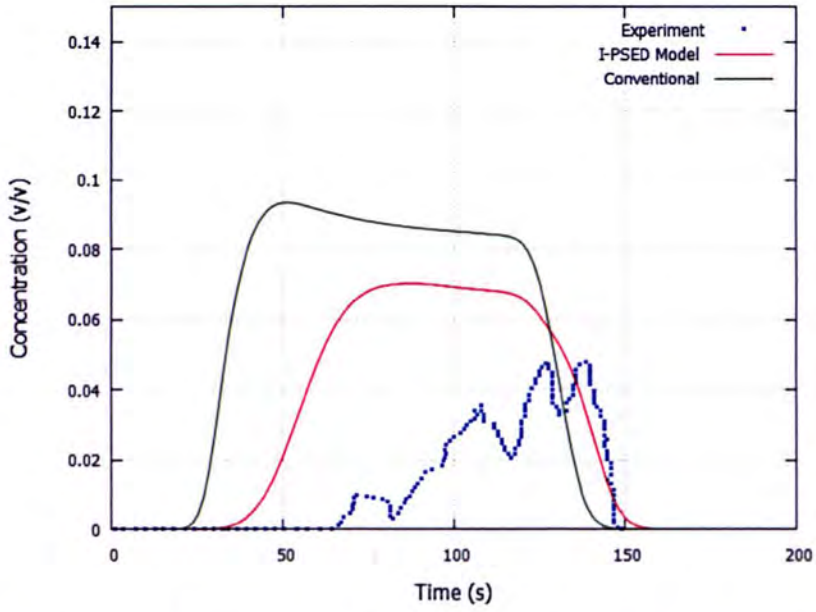

Figure 4-29: Current (I-PSED) model prediction of concentration profile compared with predictions using conventional approach and with experimental data for test coyote 5 for sensor T02 at location x=200m, y=1m and z= 0m

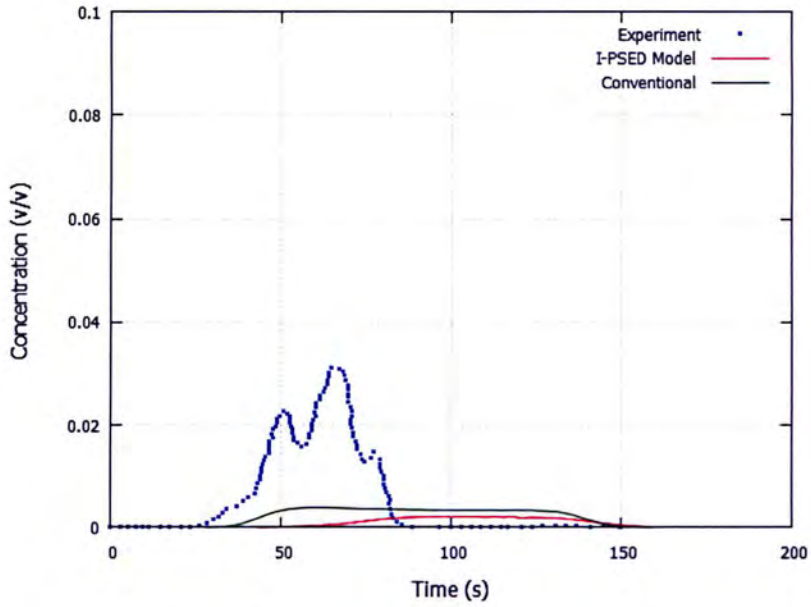

Figure 4-30: Current (I-PSED) model prediction of concentration profile compared with predictions using conventional approach and with experimental data for test coyote 5 for sensor T05 at location x=296m, y=1m and z= 48m

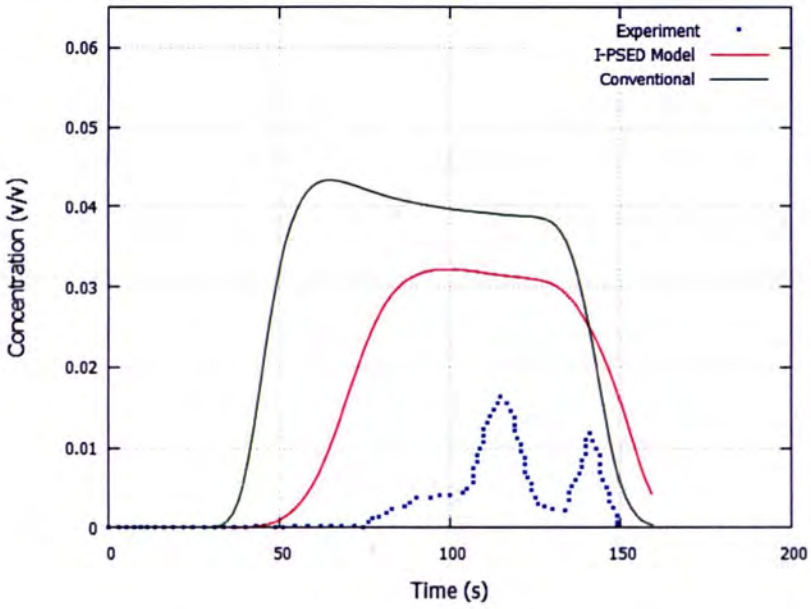

Figure 4-31: Current (I-PSED) model prediction of concentration profile compared with predictions using conventional approach and with experimental data for test coyote 5 for sensor G07 at location x=300m, y=1m and z= 0m

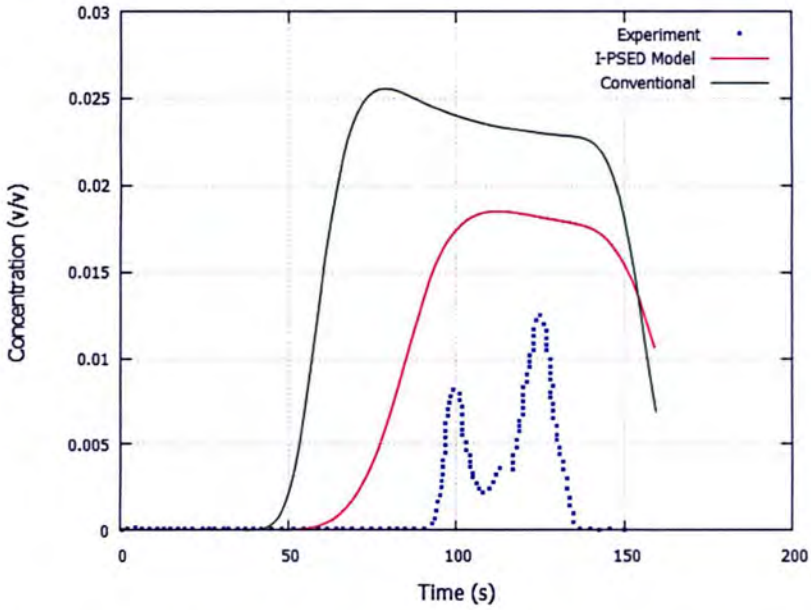

Figure 4-32:Current (I-PSED) model prediction of concentration profile compared with predictions using conventional approach and with experimental data for test coyote 5 for sensor G24 at location x=400m, y=1m and z= 0m

Again, snapshots of time evolution of the lower flammability limit has been plotted to estimate the maximum distance to the LFL for trial 5.As shown in Figure 4-33, the hazard distance grew reaching a maximum at about 100 seconds. The predicted maximum distance to the lower flammability was roughly 300m.This is comparable to the value (273m) measured during the experiment[121].Thus the current model provides a reasonably good prediction of the exclusion distance for Coyote 5 trial. Only four snapshots are shown here but a full time history has included appended in appendix B.

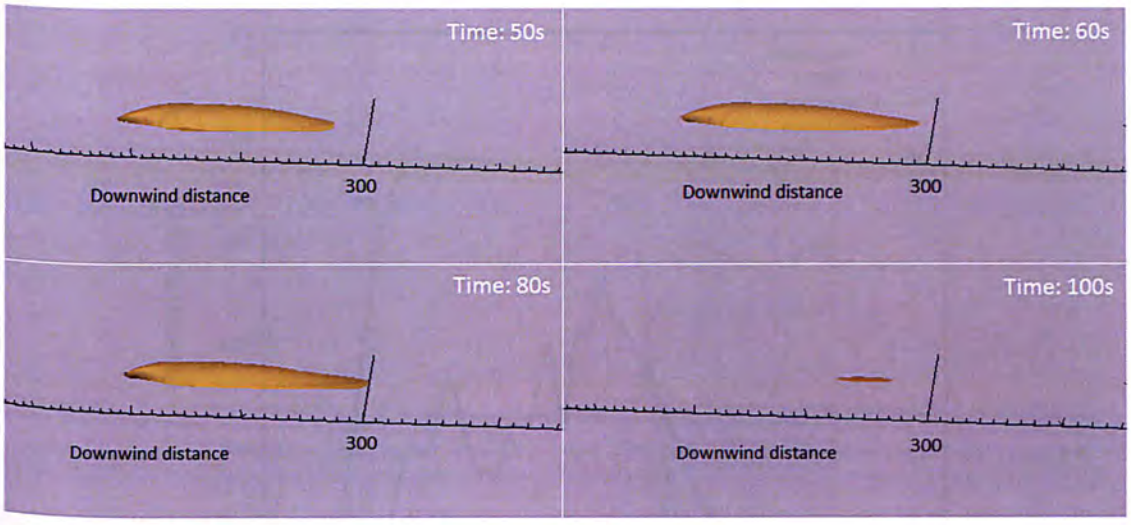

Figure 4-33: Snapshots of LFL contours at different moments showing the maximum distance to lower flammability limit for Coyote trial 5.

For Coyote trial 6, the maximum concentrations were recorded after the cloud has been ignited. Considering that the model developed in this study is purely a dispersion model and does not include the effect of burning, arc-wise comparison is not appropriate for this case. Therefore, only point by point model evaluation is carried out for this case. Figure 4-34 to Figure **4-39**) show point wise concentration profiles obtained using I-PSED and those obtained using the conventional fixed source approach compared with experimental data for Coyote trial 6. As it can be seen by reviewing the plots, I-PSED model prediction of the concentration profiles are in better agreement with the experiment at most of the sensor points compared to predictions using conventional approach.

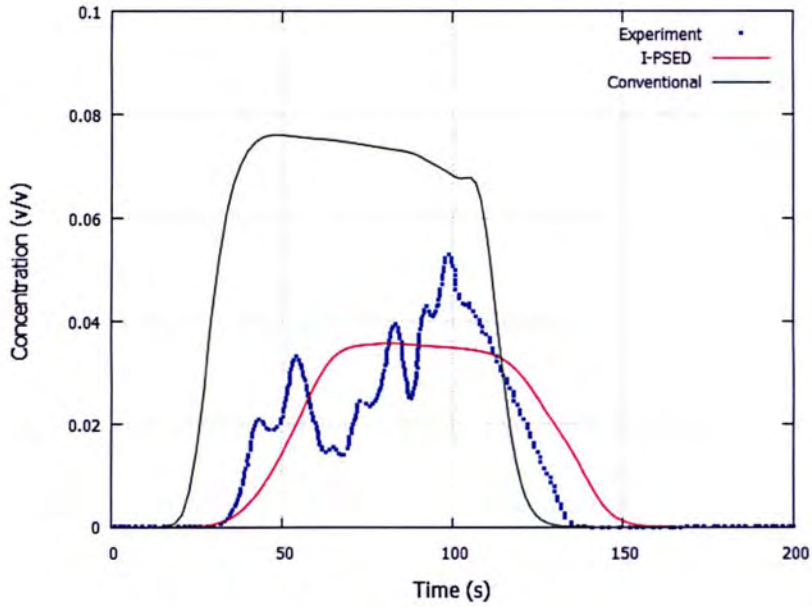

Figure 4-34:Current (I-PSED) model prediction of concentration profile compared with predictions using conventional approach and with experimental data for test coyote 5 for sensor T03 at location x=137m, y=1m and z= 30m

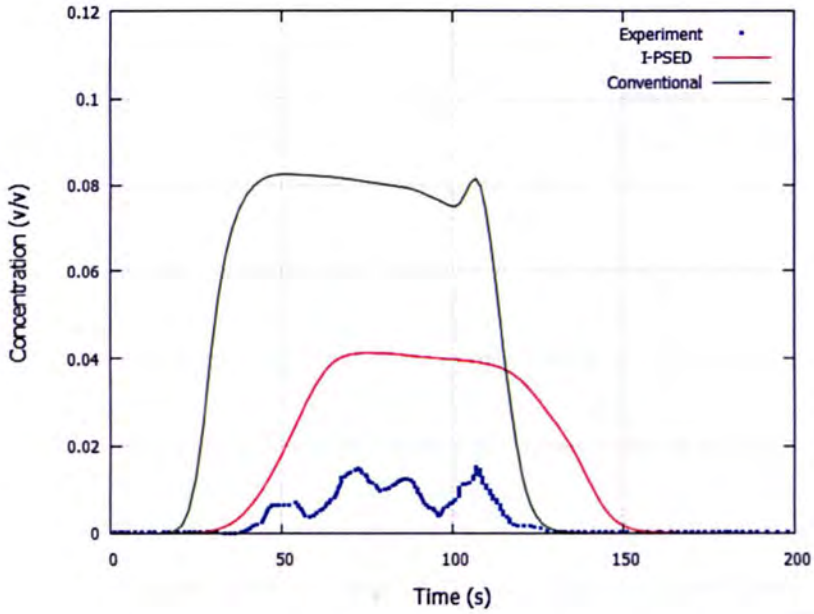

Figure 4-35: Current (I-PSED) model prediction of concentration profile compared with predictions using conventional approach and with experimental data for test coyote 5 for sensor G06 at location x=140m, y=1m and z= 0m

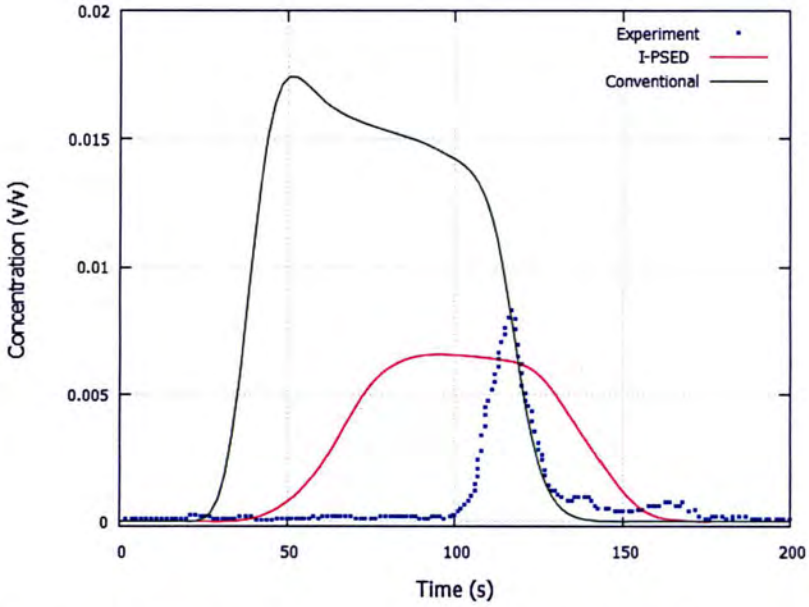

Figure 4-36: Current (I-PSED) model prediction of concentration profile compared with predictions using conventional approach and with experimental data for test coyote 5 for sensor G05 at location x=196m, y=1m and z= 36m

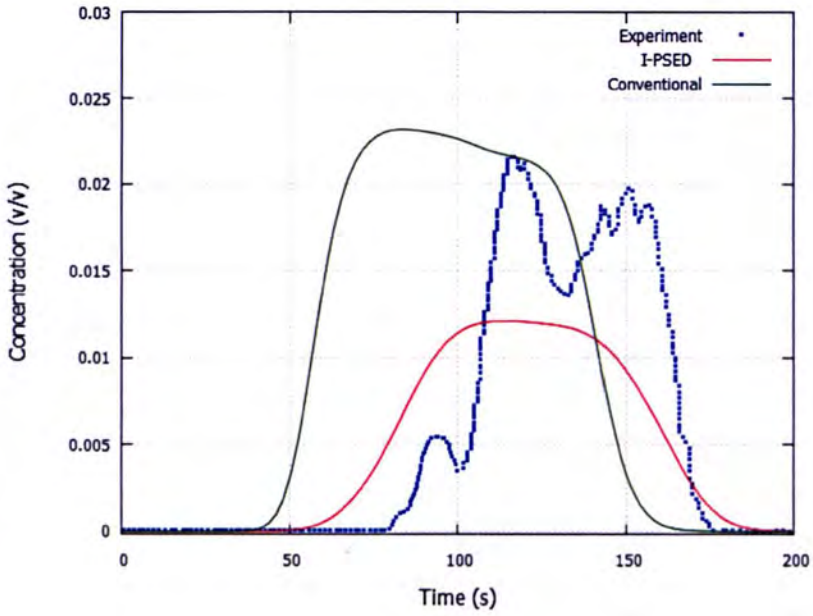

Figure 4-37: Current (I-PSED) model prediction of concentration profile compared with predictions using conventional approach and with experimental data for test coyote 5 for sensor G07 at location x=300m, y=1m and z= 0m

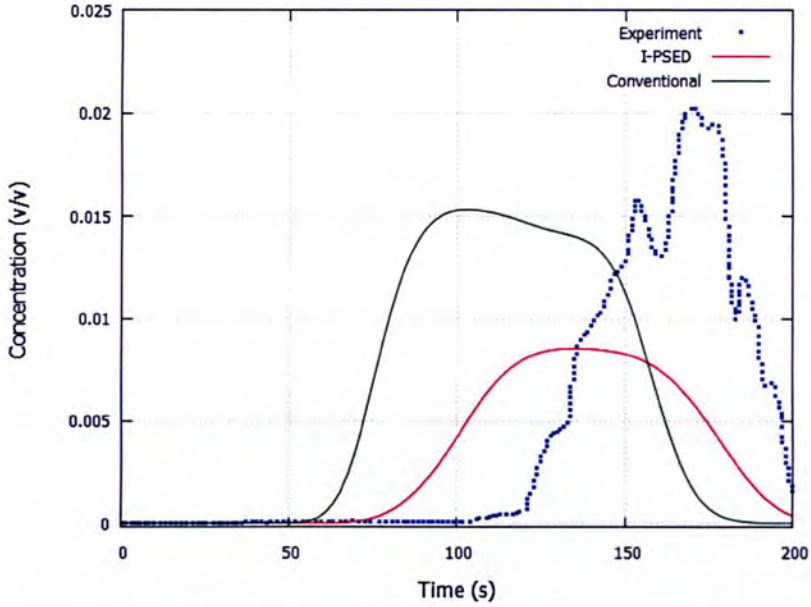

Figure 4-38: Current (I-PSED) model prediction of concentration profile compared with predictions using conventional approach and with experimental data for test coyote 5 for sensor G24 at location x=400m, y=1m and z= 0m

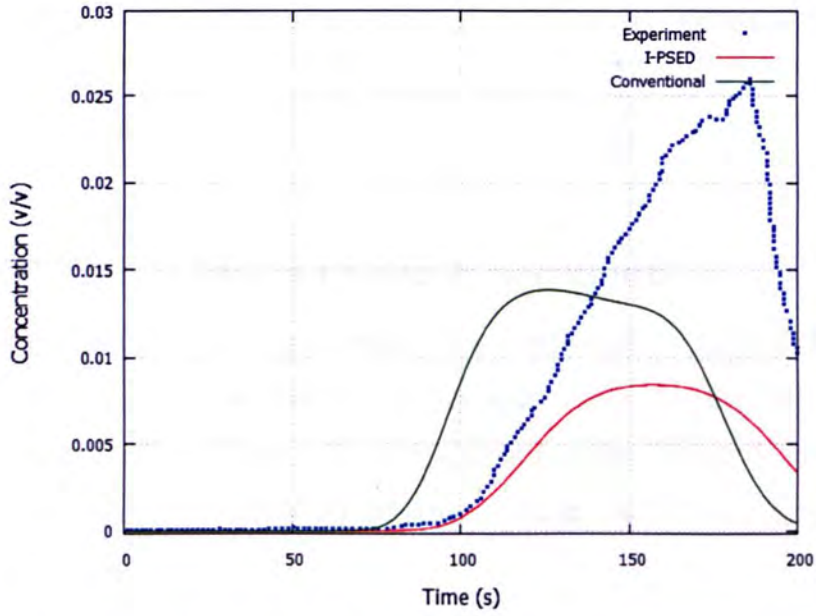

Figure 4-39: Current (I-PSED) model prediction of concentration profile compared with predictions using conventional approach and with experimental data for test coyote 5 for sensor G22 at location x=495m, y=1m and z= 70m

Also, a number of snapshots of the LFL contours have been taken from predicted flow field for this trial as shown in Figure 4-40. For this case, the exclusion distance grew reaching a maximum at 100 seconds after which it begins to decay and finally vanishes at about 120 seconds. The predicted maximum distance to the lower flammability was roughly 170m which compares well with the experimental value (277m) reported by FERC[121].See appendix B for more snapshots

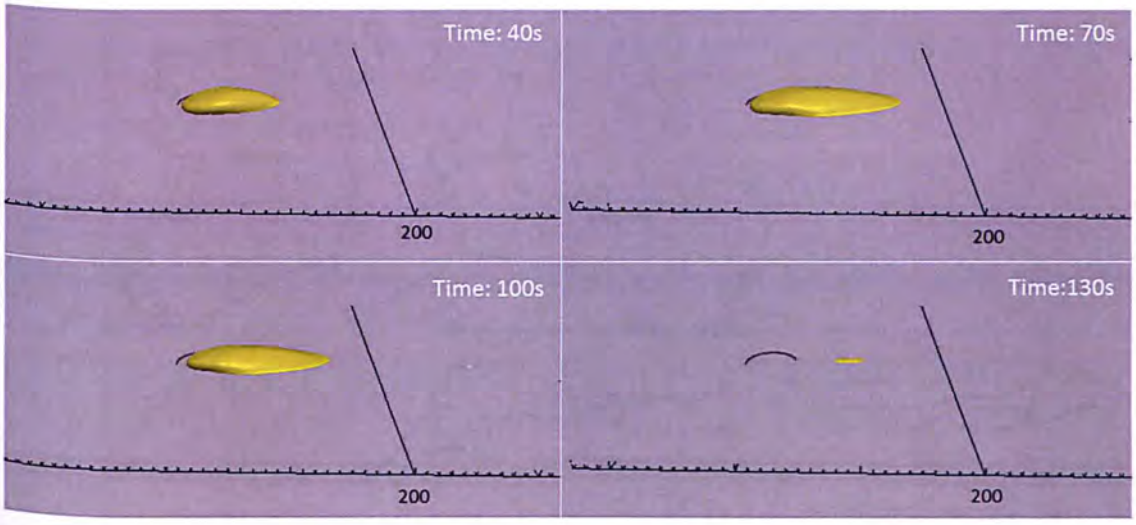

Figure 4-40: Snapshots of LFL contours at different moments showing the maximum distance to lower flammability limit for Coyote trial 6

4.2.2. Test case 2: Maplin Sand experiments

The Maplin Sands series of experiments were conducted by Shell [116] Research Limited in 1980 at an experimental facility established by the UK Ministry of Defence located near Essex, about 43 miles east of London, England. The aim was to study the dispersion and combustion processes which could result from the spill of dense flammable gas.

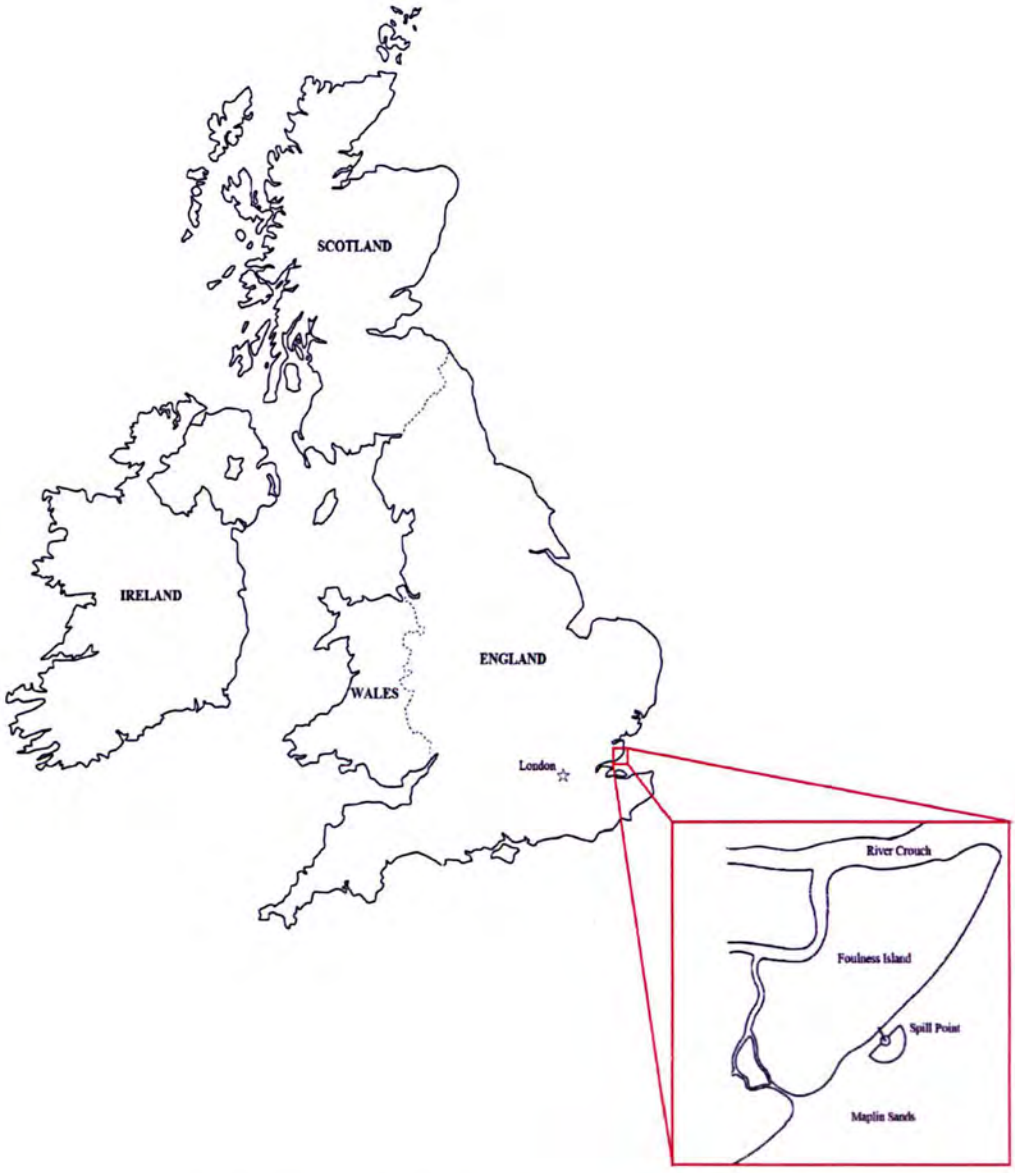

Figure 4-41: Maplin Sands (experimentation Location)

The series consisted of a total of 34 spill trials in which varying quantities of Liquefied Natural Gas and Liquefied Propane gas were released onto water. Both instantaneous and continuous release methods were employed. The continuous spills were released through a 335m long and 8-inch pipe connected to a 6-inch diameter line directed vertically downwards terminating above the water surface.

Instruments were deployed in arcs around the spill point. The instrument array consisted of approximately 360 sensors mounted on masts atop standard aluminium pontoons collecting meteorological data as well as temperature and gas concentration

data. The masts for the gas concentration sensors are about 4m high with the sensors mounted along different heights at elevations of approximately 0.5m, 1m, 1.5m and 2.5m. Wind speeds measurements were taken at height of 10m using wind wanes, ultrasonic anemometers and cup anemometers. Sea and ambient temperatures were measured at different heights using platinum resistance thermometers. The height at which temperature and wind data were taken varied for each of the 34 trials and will be stated in subsequent sections for each of the cases simulated. The sensors were set in arcs (concentrically) around the spill point in the layout shown in Figure 4-42. For the purpose of model validation carried out here, the spill information and meteorological data summarised above have been used to calibrate I-PSED model for simulation of Maplin Sand 27, 34 and 35.

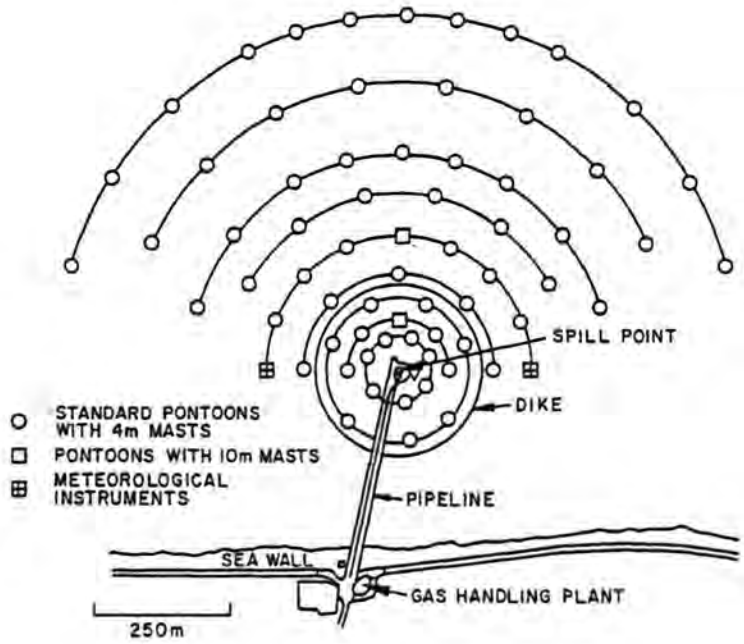

Figure 4-42: Maplin Sand sensor locations[116]

Gas concentration measurements were taken from the specified sensors and reported for all 34 trials carried out. However, only Maplin 27, 34 and 35 are included in MEP for the purpose of model validation.

Table 4-3: Summary of Maplin Sands experiments [123-125]

Parameter	Maplin 27	Maplin 34	Maplin 35
Spilled volume (m^3)	12.6	10.2	18.3
Spill rate($m^3 min^{-1}$)	3.2	3	4.7
Spill duration (s)	240	205	230
Ambient temperature (K)	288	288	289
Wind speed (ms^{-1})	5.6	8.5	9.8

By calibrating I-PSED model using the information summarised in Table 4-3, the Maplin Sand experiment has been simulated. The computational domain for the simulation stretched from -150m to 600m in the windward direction, -150m to 150m in the crosswind direction and from 0 to 50m in the vertical direction with a near field grid resolution being 1m, 0.45m and 1m in the windward, vertical and crosswind directions respectively. This is consistent with the grid resolution previously employed by Hansen et al [126]and has been found to provide a mesh independent solution. The boundary conditions were as previously described for the Coyote series, except that symmetry boundary conditions are employed at the side boundaries for all Maplin Sand simulations. The use of symmetry boundary condition is acceptable for this case as wind was aligned parallel to the x-direction and the sensor positions defined along the given wind direction so there is no need to apply wind meandering.

Similar to the experiment, the sensors are placed at several measurement stations located in arcs downwind of the spill centre at 58m, 88m, 129m 181m, 250m, 322m and 399m as shown in Figure 4-43.This arc-wise arrangement was specified at different heights ranging from 0.5 to 2.5m in the computational domain consistent with the experiment, and the representative maximum arc-wise concentration is sought at the different downwind locations. As has been acknowledged in the Model Evaluation Protocol (MEP)[127], point-wise comparison data is rare for Maplin tests, hence arc-wise comparison has been carried out here using experimental data from the same source as those used for the Coyote series i.e. data from the US Federal Energy Regulation Council (FERC) as documented by the Department of Energy [121].

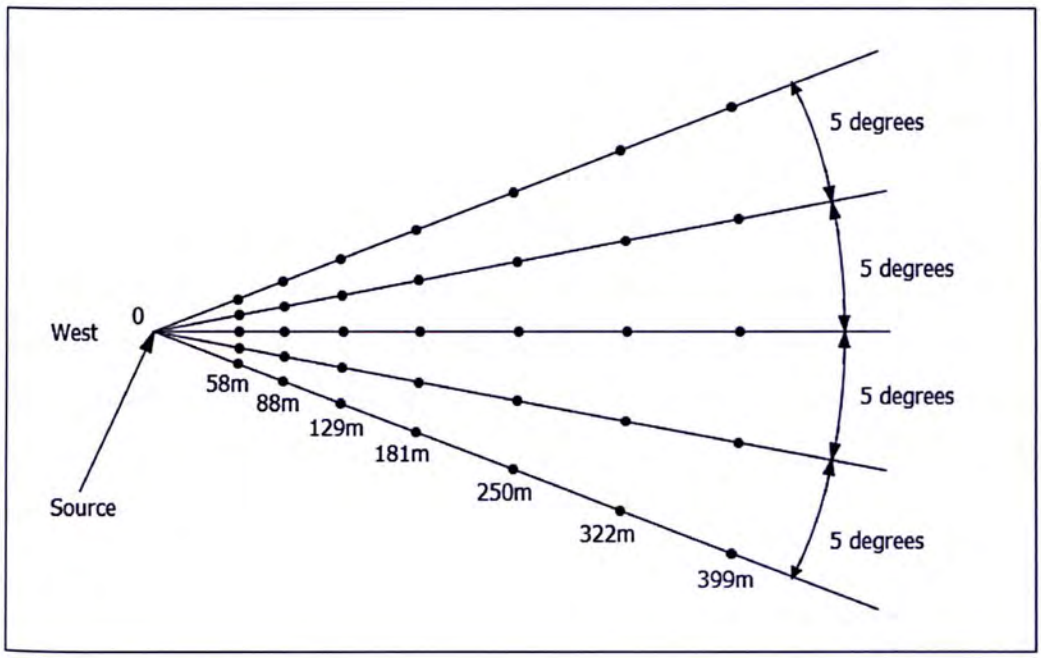

Figure 4-43: The monitoring points for vapour concentrations

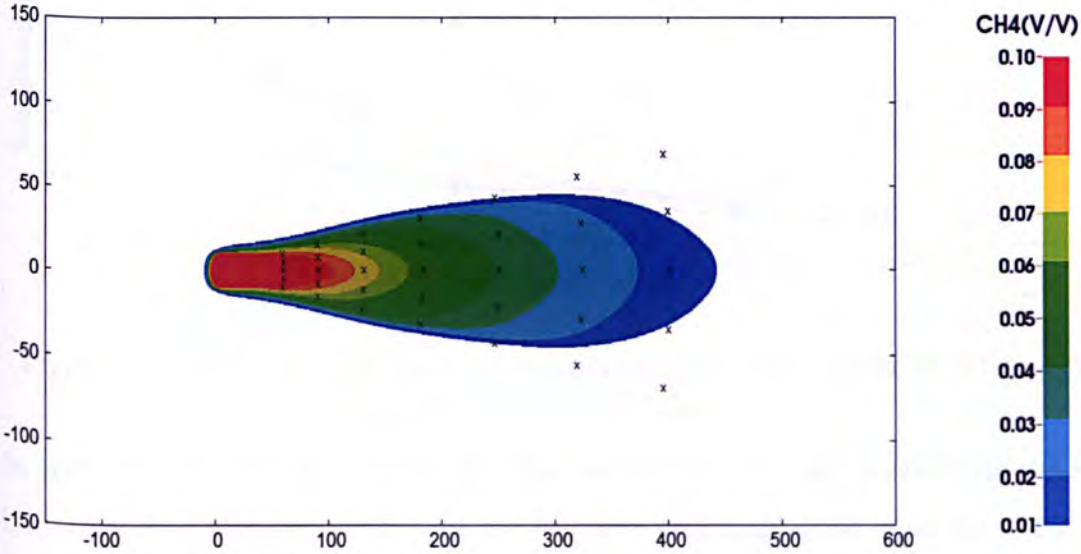

Figure 4-44: Steady state plume for test Maplin 27

A steady state plume predicted using I-PSED model for test Maplin 27 is as presented in Figure 4-44 showing the interaction of the cloud with the arc-wise sensors at time 80 seconds from the start of the spill and at a height of 1m. The long and somewhat narrow cloud shape is typical of heavy gas dispersion under medium-to-high wind speeds. As expected, the concentration levels decreases downwind as

the plume mixes with fresh ambient air and drops to within 1% around a downwind distance of 450m. Beyond this location, the concentration levels are less than one percent by volume. For the same test i.e. Maplin 27, Figure 4-45 compares the measured and predicted peak short-time averaged concentrations at several downwind locations. The results show that predictions using I-PSED and those obtained using the conventional approach correlates very well with the experiment and are within a factor of two of the experiments, hence are deemed acceptable based on MEP criteria. Predicted results clearly puts the current (I-PSED) model ahead of the conventional approach as the conventional approach under-predicted concentrations in the near-field region.

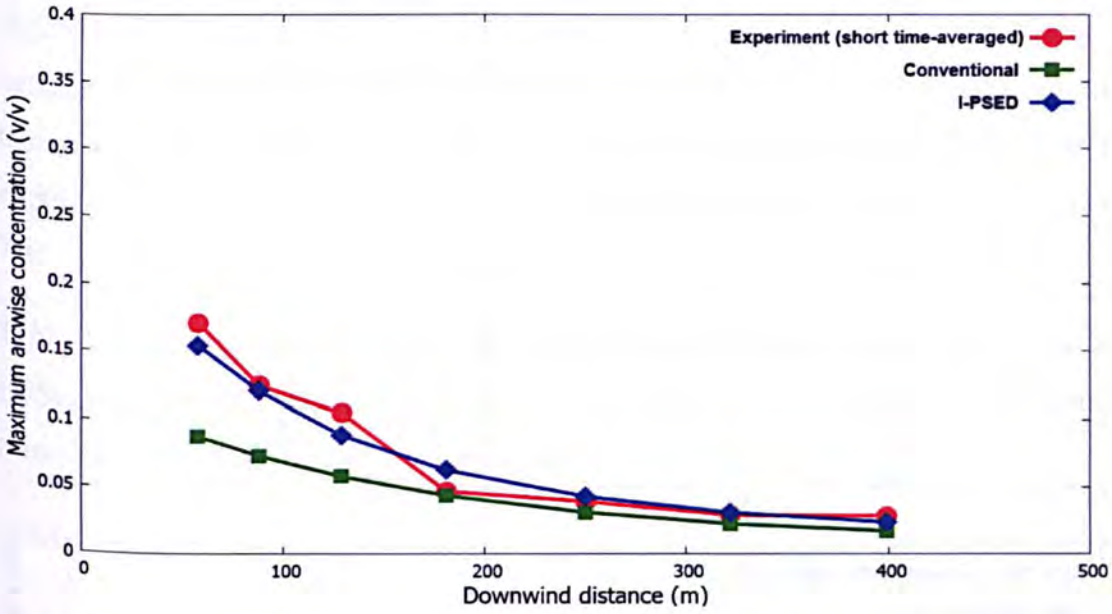

Figure 4-45: Predicted maximum arc-wise concentrations for Maplin 27 compared with experimental data

In addition to the visual evaluation of the performance of both models, the level of bias associated with each of the models has been evaluated using equation (4-2). The evaluation results as tabulated in

Table **4-4** clearly put the I-PSED model ahead of the conventional model with the errors associated with I-PSED predictions being below 16% at almost all the arc radii for which experimental data is available, except at one radius i.e. 181m. However, the same cannot be said of conventional approach as predictions using this model produced error which is above 39% at most of the arc radii predicted.

Table 4-4: Percentage errors associated with the CFD Predictions of arc-wise concentrations at different arc radius for Maplin 27

Arc radius(m)	Experiment	I-PSED	Conventional	% error (I-PSED)	% error (Conventional)
58	0.1710	0.1544	0.0877	-9.71	-48.70
88	0.1250	0.1212	0.0733	-3.04	-41.36
129	0.1050	0.0885	0.0579	-15.71	-44.86
181	0.0464	0.0624	0.0435	34.48	-6.25
250	0.0390	0.0428	0.0308	9.74	-21.03
322	0.0286	0.0306	0.0222	6.99	-22.38
399	0.0282	0.0235	0.0171	-16.67	-39.36

Figure 4-46 shows a comparison of the predicted maximum arc-wise concentrations against experimental data for test Maplin 34.For this test case, both models grossly under-predicted concentrations, but still meet the factor of two (FA2) criteria stipulated in MEP since at least 50% of model predictions are within a factor of two. The error calculations are summarised in

Table 4-5. It shows that the overall percentage under-prediction is less in the case of I-PSED model than for the conventional approach. But both models performed relatively poorly especially in the near field.

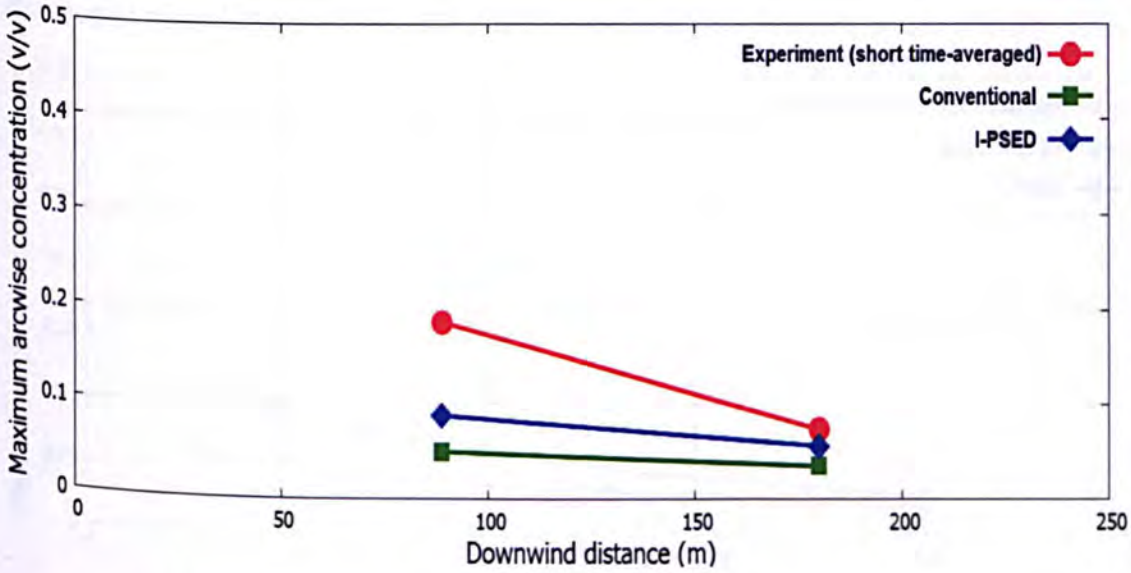

Figure 4-46: Predicted maximum arc-wise concentrations for Maplin 34 compared with experimental data

Table 4-5: Percentage errors associated with the CFD Predictions of arc-wise concentrations at different arc radius for Maplin 34

Arc radius(m)	Experiment	I-PSED	Conventional	% Bias (I-PSED)	% Bias (Conventional)
89	0.187	0.0883	0.0505	-52.78	-72.99
181	0.0738	0.0567	0.0360	-23.17	-51.22

In Figure 4-47 , the predicted short time averaged maximum gas concentrations over each arc radius are plotted alongside corresponding experimental data for test Maplin 35 for comparison. The plot shows that both models produced results which are in good agreement with experimental data with I-PSED model performing better at most of the arc radii. The conventional model under-predicted results in the near-field but performed relatively well in the far-field region. This is not the case with the I-PSED model as predictions agree very well with experiment in both the near-filed and far-field region. In order to critically assess the performance of both models, the error associated with the prediction of test Maplin 34 has also been evaluated and the results are as summarised in Appendix B. It can be readily seen from the tabulated results that the error associated with I-PSED predictions is less than 20 % at most of the points predicted as opposed to about 40 % for the conventional model. Thus, the error analysis for this test case clearly puts the newly developed model ahead of the conventional approach.

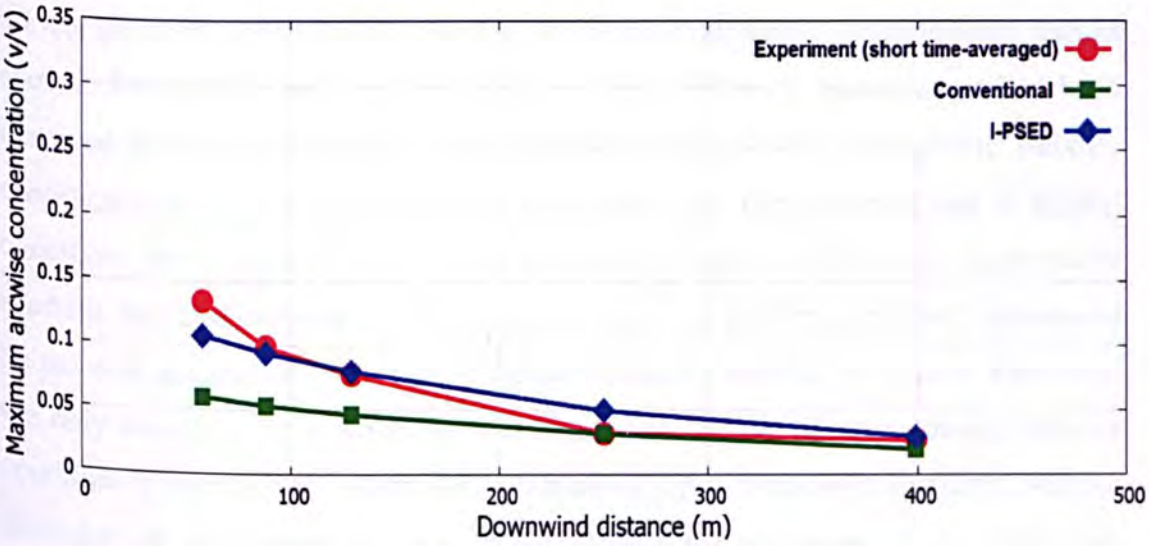

Figure 4-47: Predicted maximum arc-wise concentrations for Maplin 35 compared with experimental data

4.3. Parametric study

To understand and mitigate the effect of flammable vapour cloud, it is important to know the role of the parameters associated with the dispersion process. With a good understanding of the effect of the key parameters, appropriate measures can be taken in form of introduction of new regulations regarding the general handling of LNG. This section focuses on identifying the effect of certain source and atmospheric parameters on the dispersing gas cloud. The parametric study is carried out in two key areas, namely: turbulence models and source term. For the turbulence models, the effect of the buoyancy term in the K-εmodel on downwind concentrations is investigated by conducting simulations with and without this term. For source term, we focus on understanding the effect of the size of breach on the downwind concentrations.

4.3.1. Effect of buoyancy turbulence production

Here the effect of the added buoyancy term on LNG vapour dispersion is analysed through a simulation of Coyote trial 3. Figure 4-48 to Figure **4-50**) present the effect of using different two equation turbulence models, including the currently implemented correction to the K-epsilon model for LNG vapour dispersion simulation at different sensor locations. As it can be readily seen from the plots, the buoyancy-corrected **K-ε** model performed far better than both the K-Omega SST and the standard **K-ε**model. Both K-Omega SST and the standard **K-ε**model predictions are comparably close to each other but too large compared to experimental data as shown. The same trend was observed for test Coyote 5. However, it has been observed that the correction is not appropriate for neutral atmospheric stability condition under which Coyote trial 6 was performed. The reason is that in neutral condition, the buoyancy term should evaluate to zero as there is no temperature gradient. For LNG vapour dispersion, the temperature gradient inherently introduced by the cold gas makes it impossible for the buoyancy term to go to zero. Therefore, the only remedy is to avoid using it in simulations where the atmospheric stability condition is neutral. This explains why test case Coyote 6 has been simulated without inclusion of the buoyancy term. Even though the inclusion of the buoyancy production term is optional in CFX as indicated in the theory guide, we recommend that this term be included in LNG vapour dispersion simulations under unstable

conditions of the atmosphere. Not only is it appropriate from the physical point of view, it makes a huge difference as evident in the plots below.

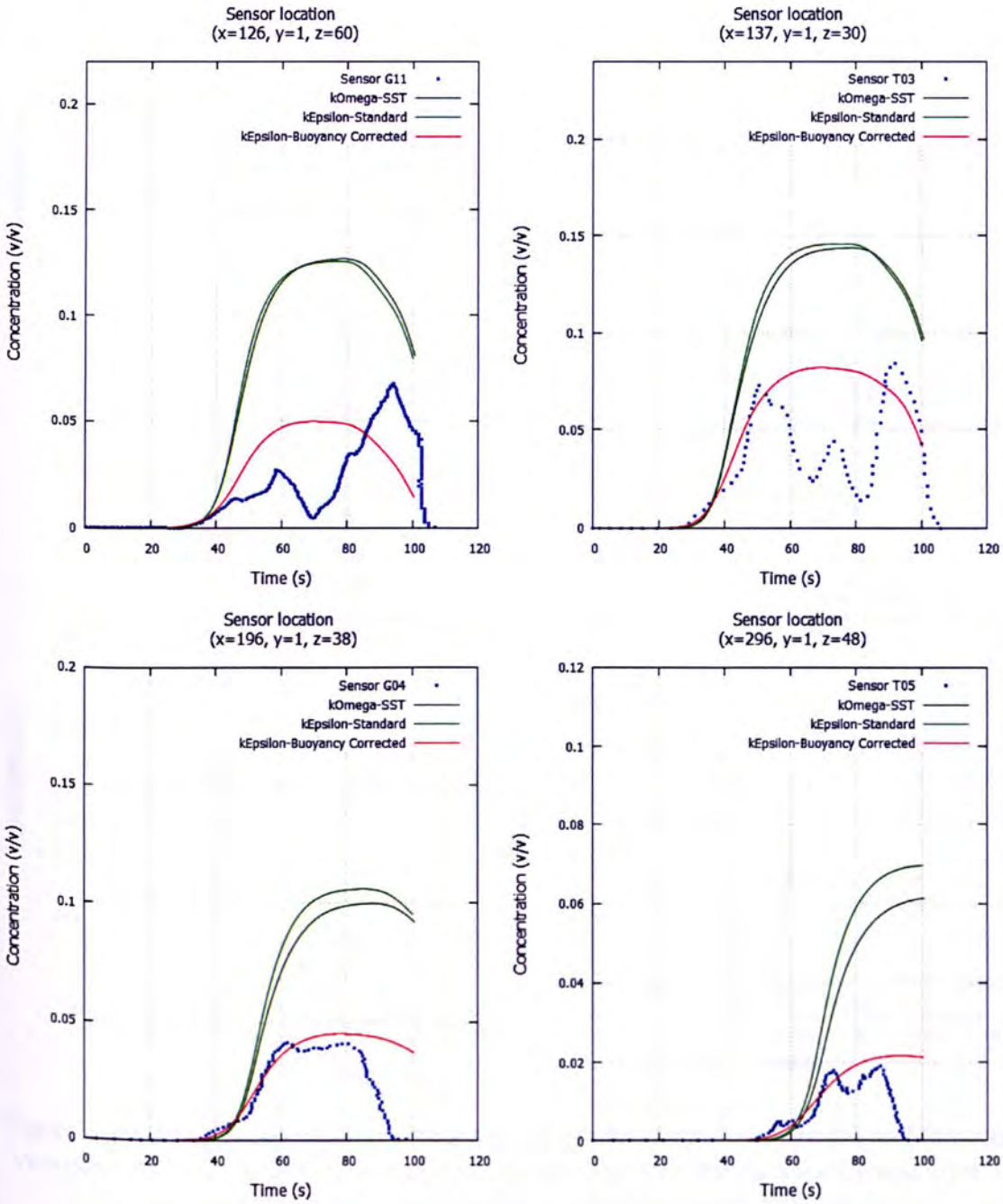

Figure 4-48: Predictions using the buoyancy-corrected turbulence model and those of two other turbulence models compared against experimental data for Coyote trial 3 for sensors located at several downwind distances and elevation 1m .

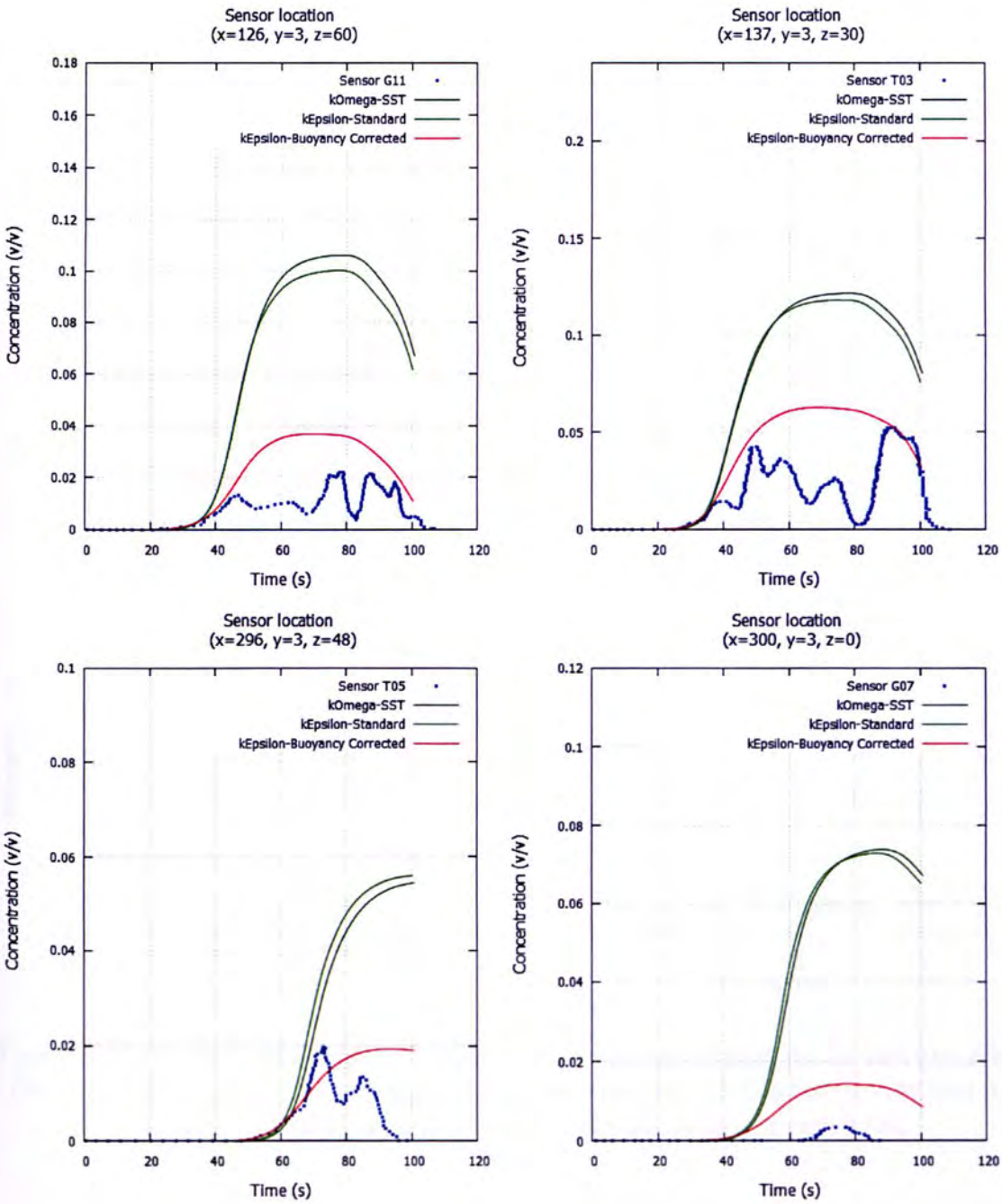

Figure 4-49: Predictions using the buoyancy-corrected turbulence model and those of two other turbulence models compared against experimental data for Coyote trial 3 for sensors located at several downwind distances and elevation 3m .

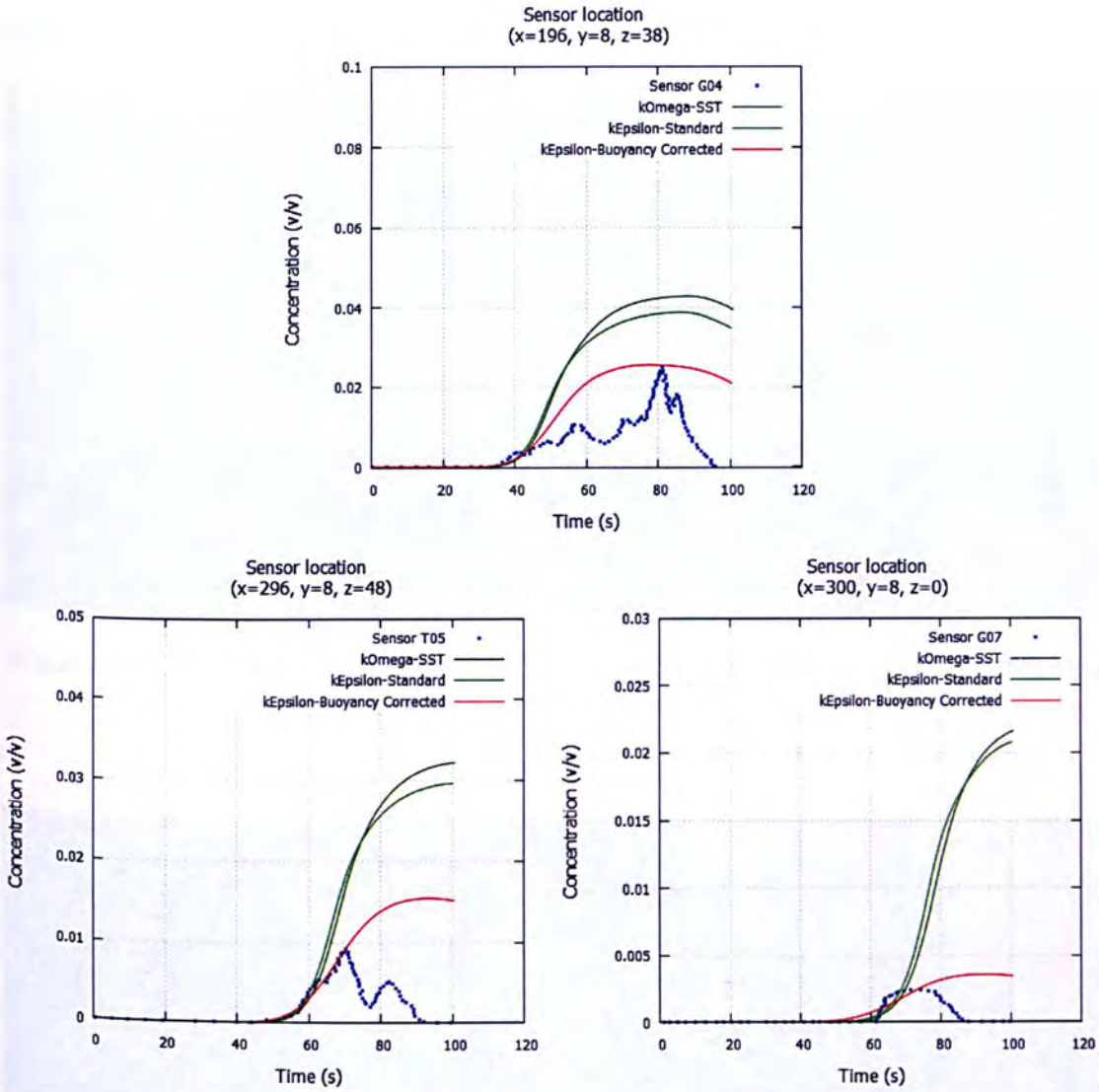

Figure 4-50: Predictions using the buoyancy-corrected turbulence model and those of two other turbulence models compared against experimental data for Coyote trial 3 for sensors located at several downwind distances and elevation 8m.

In order to further assess the effect of the buoyancy correction implemented to the K-ε model, contour plots of CH4 volume fractions at four times during the dispersion process has been plotted for the buoyancy-corrected K-ε model case and the Standard K-ε models in Figure 4-51 and Figure 4-52 respectively. As it is evident from the figures, the case which includes the buoyancy term produced contours which are typical of heavy gas dispersing in a stably stratified atmosphere. This is evident as the cloud from the buoyancy-corrected case attains greater heights at all

four times during the dispersion process as evident in the contour plots. This is expected, as it is well known that unstable condition enhance turbulence leading to enhanced vertical motion of dispersing cloud.

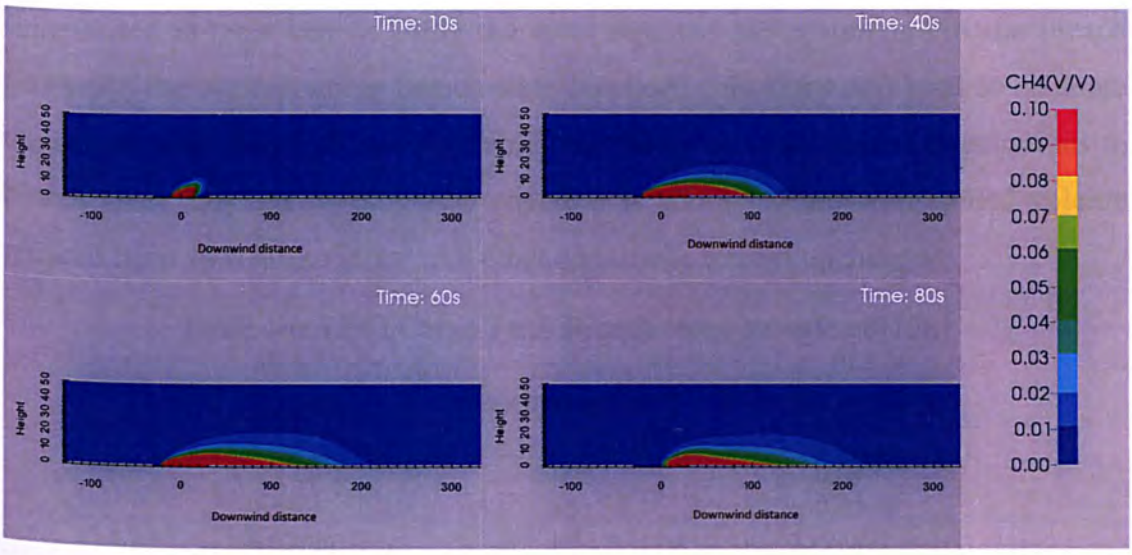

Figure 4-51: Contours of CH4 volume fraction at four different times obtained using buoyancy-corrected K-ε model

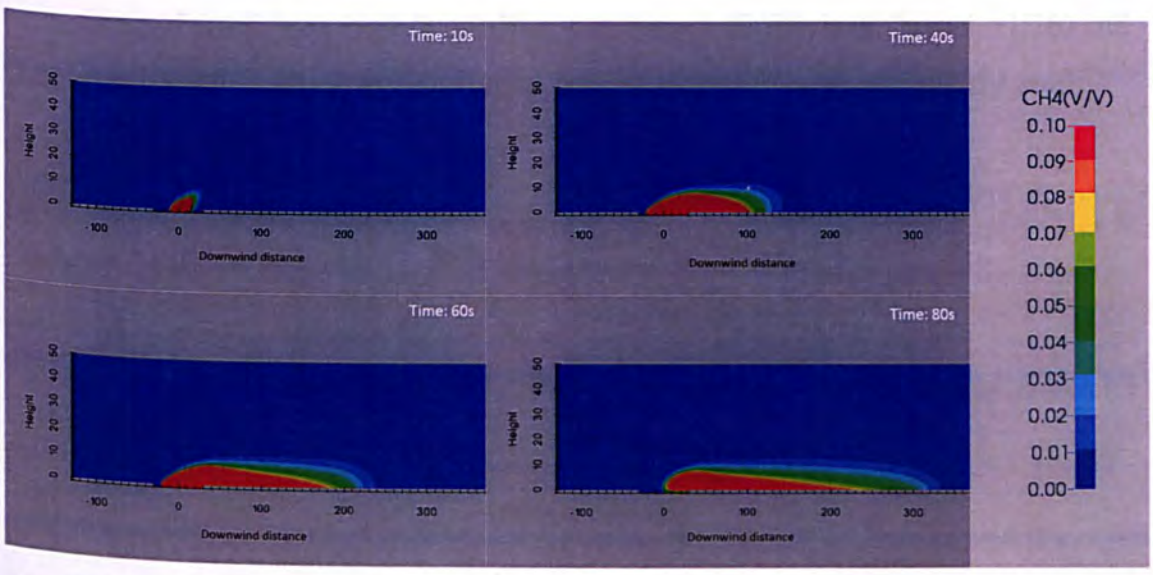

Figure 4-52: Contours of CH4 volume fraction at four different times obtained using Standard K-ε model

In summary, both models produce contour plots which are typical of heavy gas cloud (low lying cloud), but the case with buoyancy term better captured the behaviour of a dispersing gas cloud under unstable condition as vertical motion is more pronounced compared to the case without buoyancy term

4.3.2. Effect of breach size

In a recent report compiled for the US Congress[128], the Department of Energy categorised potential LNG Cargo Tank breach into five based on breach area as summarised in table below. Using the areas reported and assuming circular breach geometry, the corresponding breach sizes has been calculated and used to calibrate the source term model to investigate the sensitivity of downwind concentrations to breach sizes. For this investigation coyote 3 is simulated but with spilled volume reduced from 14.6 m^3 to 10 m^3. All other conditions remain unchanged

Table 4-6: LNG Cargo Tank Breach sizes considered[128]

Type	Breach area (m^2)	Breach radius (m)
Very small	0.005	0.04
Small	0.5	0.40
Medium	2-3	0.79-0.97
Large	5	1.26
Very large	15	2.20

Figure 4-53 shows the sensitivity of the downwind concentrations to the breach size comprising of small breach (0.4), medium size breach (0.79), large breach (1.26) and very large breach (2.20) at three different heights at time 30 seconds into the spill.

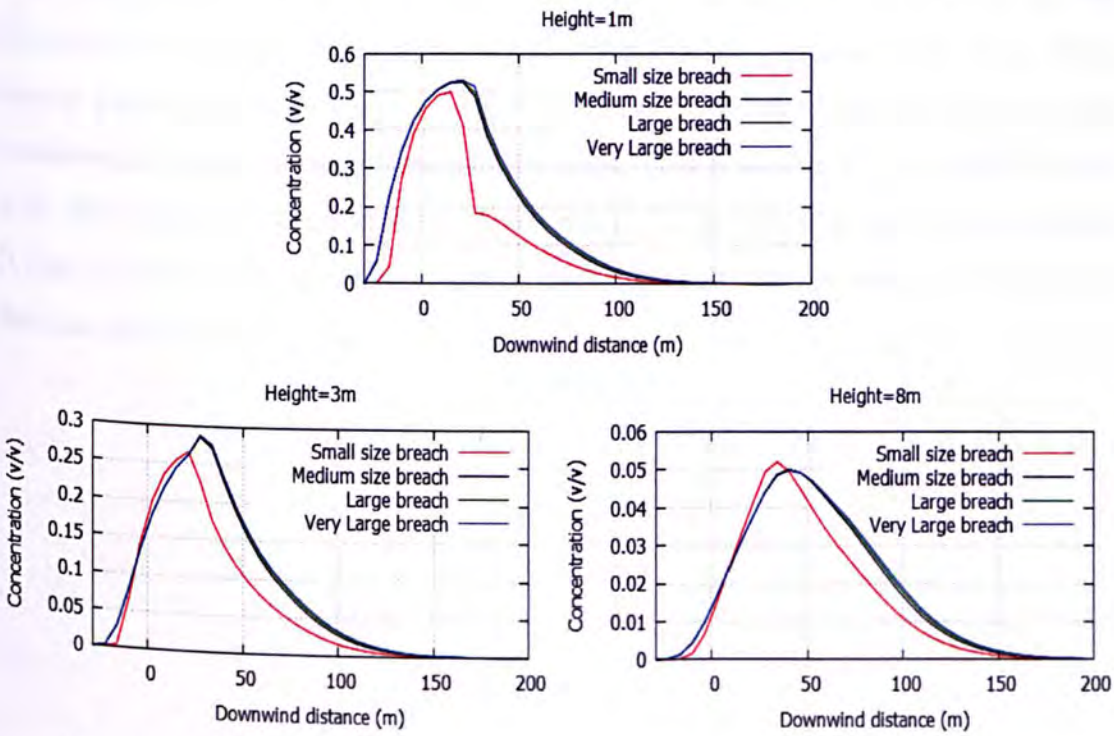

Figure 4-53: Sensitivity of downwind concentration profiles to breach sizes

As it can be readily deduced from the plots, the peak concentration is almost unaffected by the size of the breach. However, the downwind concentrations increased as the breach size is increased from small size to medium. This is particularly evident from 50 meters downwind of the spill. Also, it is interesting to notice that as the breach size is increased from medium to large and then very large, the downwind concentrations remain unchanged.

Table 4-7: Sensitivity of maximum distance to LFL to the breach size

Breach size	Maximum distance to LFL
small	180m
Medium	250m
Large	250m
Very large	250m

The sensitivity of the lower flammability limit to breach sizes is as presented in Table 4-7. With small breach size, the predicated distance to the lower flammability was 180m.As the breach is increased from small to medium size, the maximum distance to LFL increased significantly to 250m.Further increases from the medium size to large and finally very large breach size did not introduce any change in the maximum distance to lower flammability limit. This is similar to the trend observed with the downwind concentrations. Thus, one can conclude that up to breach size of 0.79m (medium), the downwind concentration distribution becomes unaffected by the size of the breach.

Chapter 5: Conclusion and future work

5.1. Summary

A CFD model has been developed and validated in this thesis for the numerical simulation of the combined processes of spill, spreading, vapourization and atmospheric dispersion of Liquefied Natural Gas. The model is therefore termed integrated pool spreading, evaporation and dispersion (I-PSED) model.

Firstly, rhoReactingBuoyantFoam which is an existing combustion model in OpenFOAM was modified to a form suitable for dispersion simulation by deleting the reaction term in the species transport equation. This became necessary as OpenFOAM does not have any dedicated solver for dispersion calculation and the solver chosen for modification is the only one that incorporates species transport and full buoyancy model and hence most suitable for LNG vapour dispersion. Following the establishment of the basic dispersion solver, a buoyancy correction term which is based on density gradient was added to the standard k-ε model to account for turbulence generation due to buoyancy effect as described in section 3.2.1. Also, the effect of atmospheric stability and stratification on the dispersing gas cloud has been incoporated into the model through a series of equations (depending on stability class) as described in section 3.2.2.

Going forward, an integral type source term model was developed for the source term i.e. simulation of the spilling (blow down) process, pool spreading and evaporation processes (see section 3.3). The aim was that the source term model provide an input file (source term) to the dispersion model developed and this has been achieved in this present study as illustrated in the coupling algorithm of Figure 3-2. The release rate of LNG from a reservoir is modelled via the orifice model which derives from Bernoulli principle. The spreading of the pool resulting from the spillage was characterised using Hissong model which is a balance of the inertia and gravitational forces acting on the pool. Heat transfer to the pool was modelled using the film boiling correlation of Klimenko and the subsequent evaporation prescribed through energy balance and depends on the heat flux to the pool and the heat of vapourization of LNG.

Coupling of the dispersion model and the source term model in the framework of OpenFOAM gave the I-PSED model which is the main objective of this work. The coupling (integration) process was achieved via the creation of a new boundary condition in OpenFOAM. The newly created boundary condition (poolInletFixedValue) has the capability to read input files provided by the source term model and use the data as source term for the dispersion model. Thus, the source term model provides a look-up file from which newly developed boundary condition reads radius and evaporation rate at every calculation step. These values are then used to inject appropriate mass flow rate of LNG vapour into the domain through the boundary cells that fall within the radius at every step of the calculation process.

To ascertain the integrity of the newly developed approach, a validation study has been conducted in which the I-PSED model was applied to simulate experimental trials and results compared with experimental data. First and foremost, the source term model was validated based on data from the ESSO/API spill experiment which is the only field scale experiment for which source data is available for spill on water. Then the integrated (I-PSED) model is validated based on the Coyote series experiments as well as the Maplin Sands experiments. The Coyote series consists of four experiments, three of which were included in the MEP for validation of dispersion models. All three cases included in the MEP have been simulated in this work. The Maplin Sand series consist of three experiments all of which have been simulated in this study for further validation. Also, conventional approach (non-transient source) was used to simulate these experiments and results compared with those obtained using I-PSED Model.

5.2. Conclusion

Computational results of the validation studies put the newly developed I-PSED model well ahead of the hitherto used conventional modelling approach. For the arc-wise validation studies carried out, the newly developed model produced results with only about 25% bias at most of the downwind arc radii as opposed to 75% bias which resulted from the conventional approach at most arc radii. For the point-wise comparison, the I-PSED model gave results which are in very good agreement with the experimental data. The conventional model on the other hand over-predicted

concentrations at most of the sensor points. Moreover, the cloud arrival time are much better captured with the newly developed model than with the conventional approach. Thus, I-PSED model can be reliably in risk analysis of environmental flows related to cryogenic release of flammable gases.

Having established the integrity of the newly developed model, parametric studies was then conducted to investigate the effect of certain physical models and key parameters. These include an analysis of the effect of the inclusion and non-inclusion of the buoyancy term in the turbulent kinetic energy equation. Simulation results show that under unstable atmospheric condition, including the buoyancy term produces results which are in better agreement with experimental measurements at most sensor locations. The better performance of the newly developed I-PSED model was also further reinforced by contour plots of the concentration field. As it is evident from the concentration distribution, vertical motion is well enhanced in the case with buoyancy correction. This is expected as it is well known from the physical point of view that unstable atmospheric condition enhances turbulence and consequently vertical motion. Again from a physical and simulation point of view, we find it inappropriate to use the buoyancy production term in neutral and unstable atmospheric conditions for Cryogenic releases such as LNG spill and dispersion.

5.3. Recommendations for future work

In the course of the model development carried out in this thesis, a number of areas that require research attention have been identified which has not been addressed in the current research as they are outside the scope of the work proposed. Therefore, suggestions and recommendations for future development of this work are proposed in what follows.

LNG-water turbulence

Accidental release of LNG from Cargo Tanks during marine transportation would likely result in a spill from above the water surface. In this situation, the spilled liquid will penetrate the water surface creating enormous turbulence which could enhance heat transfer and consequently vapour generation rate. Current models have assumed quiescent release at the water-line level (category II releases) and modelled the heat transfer based on a quiescent heat transfer coefficient. The only attempt so far to address this issue was made by Hissong in which a new parameter was

proposed (turbulent factor) which is essentially the ratio of turbulent heat transfer coefficient to the heat transfer coefficient based on quiescent boiling. Therefore, by knowing the value of the turbulent factor and the heat transfer coefficient based on quiescent boiling, the heat transfer coefficient for turbulent boiling can be obtained. However, the correlations for the evaluation of the turbulent factor was not fully developed as Hissong admitted there are currently very little basis for parameterisation of certain variables in the model.

Underwater LNG release

The release of LNG from below the water surface can occur in event of ship grounding during LNG transportation. For such a scenario, the source term modelling becomes a bit more complex and there may be no pool formation on the surface of the water. Moreover, the possibility of droplets formation may necessitate the use of Lagrangian particle tracking in the near field. Even though, this will require a huge computational power, the continued advancement in computational effort has opened it up as an area that can be further investigated. Considering that the model developed in this study (I-PSED) can read an input file from any kind of source term model, it can therefore be interfaced with a Lagrangian particle tracking code for LNG dispersion simulation of underwater release. Alternatively, a full-fledged multiphase flow model can be adapted with the associated additional computational expense. This is an area requiring huge research attention.

Wind direction and meandering

A pool of LNG boiling on a substrate (water or land) generates vapour which is thrown up into the atmosphere with some weak upward momentum acquired due to the vapourization process. This makes it possible for the wind to play a major role in the downwind motion of the dispersing gas cloud. Typically, the wind direction is a key factor that determines which way the gas cloud goes. Therefore, accurate meteorological information about wind speed and direction at the site of the spill is very important input on which a dispersion model relies. While information about wind speed at specific site locations is normally reported for test sites, the same cannot be said of the wind direction. This is further complicated by the fact that wind changes direction intermittently making it inappropriate to specify an average wind direction in a simulation of a dispersion process. While an average wind direction

can produce conservative results in the case of arc-wise validation study, the cloud may miss some sensors in the case of point-wise study causing the entire dispersion model to break down. This is the essence of arc-wise comparison as it circumvents the effect of the meandering wind. Here, we recommend that accuracy of dispersion models can be improved if better ways are devised to account for wind meandering particularly in situations where information about the time varying wind angle is lacking. In cases where time varying wind angle is available at specific positions, method should be sought to extrapolate this information to the location of the domain wind inlet.

LNG pool geometry

Current pool spreading models assume a circular or semi-circular geometrical configuration for the spreading pool. But in reality, the pool is expected to be irregular in shape. Even though, this is not expected to introduce significant difference in the downwind dispersion of the gas cloud, it is worth examining the extent to which it can be important. This can be in form of the introduction of some form of shape correction factor or using alternative approaches based on physics.

References

[1] C. J. Wang, J. X. Wen, and Z. B. Chen, "Simulation of Large-Scale LNG Pool Fires Using FireFoam," *Combust. Sci. Technol.*, vol. 186, no. 10–11, pp. 1632–1649, 2014.

[2] B. Sun, R. P. Utikar, V. K. Pareek, and K. Guo, "Computational fluid dynamics analysis of liquefied natural gas dispersion for risk assessment strategies," *J. Loss Prev. Process Ind.*, vol. 26, no. 1, pp. 117–128, Jan. 2013.

[3] A. Luketa-Hanlin, R. P. Koopman, and D. L. Ermak, "On the application of Computational Fluid Dynamics codes for liquefied natural gas dispersion," *J. harzadous Mater.*, vol. 140, pp. 504–517, 2007.

[4] J. L. W. and R. M. Pitblado, *LNG RISK BASED SAFETY Modeling and Consequence Analysis*. John Wiley & Sons, Inc., Hoboken, New Jersey, 2010.

[5] DNV Offshore Technical Guidance, "Floating Liquefied Gas Terminals," *Float. Liq. Gas Termin. Rep. OTG-02.*, no. March, pp. 1–96, 2011.

[6] ABS Consulting, "Consequence assessment methods for incidents involving releases from liquefied natural gas carriers," American Bureau of Shipping (ABS) Consulting *Report GEMS 1288209*, 2004.

[7] D. M. Webber, SE Gant, MJ Ivings & SF Jagger, "LNG source term models for hazard analysis RR789," *HSE Rep. RR789*, 2010.

[8] A. Luketa-Hanlin, "A review of large-scale LNG spills: Experiments and modeling," *J. Hazard. Mater.*, vol. 132, no. 2–3, pp. 119–140, 2006.

[9] British Standards, "Installation and equipment for liquefied natural gas — Design of onshore installations (BS EN1473:2007)," 2007.

[10] NFPA59A, "Standards for the Production, Storage and Handling of Liquefied Natural Gas (LNG)." 2013.

[11] D. Siuta, A. S. Markowski, and M. S. Mannan, "Uncertainty techniques in liquefied natural gas (LNG) dispersion calculations," *J. Loss Prev. Process Ind.*, vol. 26, no. 3, pp. 418–426, 2013.

[12] M. Pontiggia, M. Derudi, V. Busini, and R. Rota, "Hazardous gas dispersion: A CFD model accounting for atmospheric stability classes," *J. Hazard. Mater.*, vol. 171, no. 1–3, pp. 739–747, 2009.

[13] M. J. Ivings, S.F. Jagger, C. J. Lea, D.M. Webber, "Evaluating Vapor Dispersion Models for Safety Analysis of LNG Facilities," *Heal. Saf. Exec. Res. Rep. JC7300025.Health Saf. Lab.*, no. February, 2007.

[14] S. Sklavounos and F. Rigas, "Simulation of Coyote series trials—Part I:: CFD estimation of non-isothermal LNG releases and comparison with box-model predictions," *Chem. Eng. Sci.*, vol. 61, no. 5, pp. 1434–1443, Mar. 2006.

[15] F. Gavelli, E. Bullister, and H. Kytomaa, "Application of CFD (Fluent) to LNG spills into geometrically complex environments," *J. Hazard. Mater.*, vol. 159, no. 1, pp. 158–168, Nov. 2008.

[16] F. Gavelli, M. K. Chernovsky, E. Bullister, and H. K. Kytomaa, "Quantification of source-level turbulence during LNG spills onto a water pond," *J. Loss Prev. Process Ind.*, vol. 22, no. 6, pp. 809–819, Nov. 2009.

[17] R. Qi, D. Ng, B. R. Cormier, and M. S. Mannan, "Numerical simulations of LNG vapor dispersion in Brayton Fire Training Field tests with ANSYS CFX.," *J. Hazard. Mater.*, vol. 183, no. 1–3, pp. 51–61, Nov. 2010.

[18] D. W. Hissong, "Keys to modeling LNG spills on water," *J. Hazard. Mater.*, vol. 140, no. 3, pp. 465–477, 2007.

[19] N. S. Holmes and L. Morawska, "A review of dispersion modelling and its application to the dispersion of particles: An overview of different dispersion models available," *Atmos. Environ.*, vol. 40, no. 30, pp. 5902–5928, 2006.

[20] J. Steven, R.; Hanna Gary A.; Briggs Rayford P.; Hosker, *Handbook on atmospheric diffusion; prepared for the U.S Department of Energy*, no. 3. Technical Information Center, U.S Department of Energy, 1983.

[21] T. O. Spicer and J. a Havens, "Field test validation of the DEGADIS model," *J. harzadous Mater.*, vol. 16, pp. 231–245, 1987.

[22] D. L. Ermak, S. T. Chan, D. L. Morgan, and L. K. Morris, "A comparison of dense gas dispersion model simulations with Burro series LNG spill test results," *J. Hazard. Mater.*, vol. 6, no. 1–2, pp. 129–160, 1982.

[23] J. S. Puttock, "Comparison of Thorny Island data with predictions of HEGABOX/HEGADAX," *J. harzadous Mater.*, vol. 16, pp. 439–455, 1987.

[24] A. Bernatik and M. Libisova, "Loss prevention in heavy industry: Risk assessment of large gasholders," *J. Loss Prev. Process Ind.*, vol. 17, no. 4, pp. 271–278, 2004.

[25] D. R. Brook, N. V Felton, C. M Cle, D.C.H Strickland, I. H Griffiths, R. D Kingdon, "Validation of Urban Dispersion Model (UDM)," *Int. J.Env. Pollu.*, vol. 20, pp. 11–21, 2003.

[26] J. Spicer, T.; Havens, "User's guide for DEGADIS 2.1: DENSE GAS DISPERSION MODEL," *Off. Air Qual. Plan. Stand. Air Radiation, US Environ. Prot. Agency*, 1989.

[27] W. Dai, "Applying proper dispersion models for industrial accidental release," *2004 AWMA Annu. Conf.*, 2004.

[28] D. L. Morgan, Jr., L.K Morris, D.L Ermak, "SLAB : A Time-Dependent Computer Model For the Dispersion of Heavy Gas Releases in the atmosphere," *UCRL-53383, Lawrence Livermore Natl. Lab. Livermore, CA*, 1983.

[29] D. Ermak, "Users Manual for SLAB: An Atmospheric Model for Denser-than-air releases," *Lawrennce Livermore Natl. Lab.*, 1990.

[30] A. Dissertation and R. Qi, "LIQUEFIED NATURAL GAS (LNG) VAPOR DISPERSION MODELING WITH COMPUTATIONAL FLUID DYNAMICS CODES," no. August, 2011.

[31] K. Sun, B.; Guo, "LNG accident dynamic simulation: Application for hazardous consequence reduction," *J. Loss Prev. Process Ind.*, vol. 26, pp. 82–97, 2013.

[32] H. K. Versteeg and W. Malalasekera, "An introduction to computational fluid dynamics: the finite volume method," *Fluid flow handbook. McGraw-Hill ....* 2007.

[33] S. Patankar, "Numerical heat transfer and fluid flow," *Series in coputational methods in mechanics and thermal sciences.* pp. 1–197, 1980.

[34] D. R. Stull, H. Prophet, "JANAF Thermochemical Table, Second Edition, National Bureau of Standards(US)." 1971.

[35] W. Sutherland, "The vicosity of gases and molecular force," *Philos. Mag. S.5*, vol. 36, pp. 507–531, 1893.

[36] N. Jarrin, "Syntethic Inflow Boundary Conditions for the Numerical Simulation of Turbulence," *PhD Thesis Submitt. to Fac. Eng. Phys. Sci. Univ. Manchester*, pp. 1–258, 2008.

[37] T. X. Qin, Y. C. Guo, W. Y. Lin, "Large Eddy Simulation of Heavy Gas Dispersion around an Obstacle," in *Proceedings of the Fifth International Conference on Fluid Mechanics, Shanghai, China*, 2007, pp. 15–19.

[38] R. Stoll and F. Porté-Agel, "Dynamic subgrid-scale models for momentum and scalar fluxes in large-eddy simulations of neutrally stratified atmospheric boundary layers over heterogeneous terrain," *Water Resour. Res.*, vol. 42, no. 1, p. n/a–n/a, Jan. 2006.

[39] F. Nicoud and F. Ducros, "Subgrid-scale stress modelling based on the square of the velocity gradient tensor," *Flow, Turbul. Combust.*, vol. 62, no. 3, pp. 183–200, 1999.

[40] J. Boussinesq, "Theorie de L'Ecoulement Toubillant," *Mem. Acad. Sci.*, vol. 23, 1877.

[41] Y. Tominaga and T. Stathopoulos, "Turbulent Schmidt numbers for CFD analysis with various types of flowfield," *Atmos. Environ.*, vol. 41, no. 37, pp. 8091–8099, 2007.

[42] M. I. Luca, "Development and Validation of an Object Oriented CFD Solver for Heat Transfer and Combustion Modeling in Turbomachinery Applications," *Thesis*, vol. Doctor of, p. 261, 2008.

[43] B. E. Jones, W.P.; Launder, "The prediction of laminarization with a two-equation model of turbulence," *Int. J. Heat Mass Transf.*, vol. 15, pp. 301–314, 1972.

[44] B. E. Launder, D.B. Spalding, "The Numerical Computation of Turbulent Flows," *Comput. Methods Appl. Mech. Eng.*, vol. 3, pp. 269–289, 1974.

[45] C. Alinot, C.; Mason, "k-ϵ model for the atmospheric boundary layer under various thermal stratifications," *J. Sol. energy Eng.*, pp. 438–443, 2005.

[46] J. Bredberg, "On the Wall Boundary Condition for Turbulence Models," *Chalmer's Intern. Rep. 00/4 , Goteborg, Sweden.*, p. 25, 2000.

[47] B. Blocken, T. Stathopoulos, and J. Carmeliet, "CFD simulation of the atmospheric boundary layer: wall function problems," *Atmos. Environ.*, vol. 41, no. 2, pp. 238–252, 2007.

[48] J. Wieringa, "Updating the Davenport roughness classification," *J. Wind Eng. Ind. Aerodyn.*, vol. 41, no. 44, pp. 357–368, 1992.

[49] Fluent, "ANSYS FLUENT User ' s Guide," vol. 15317, no. November, p. 2498, 2011.

[50] T. Cebeci, P. Bradshaw, "Momentum transfer in boundary layers," *Hemisph. Publ. Corp. York*, 1997.

[51] J. Nikuradse, "Stromungsgesetze in rauhen Rohren," *Forschg.Arb.Ing.-Wes. No 361*, 1993.

[52] M. M. Chalchooghi, "Modelling and CFD Simulation of a Fluidized Bed Process for the Capture of CO2 from Fossil Fuel Combustion Sources," Greenwhich Univrsity, 2013.

[53] A. Heidari, "Numerical simulation of Deflagration to Detonation Transition in Hydrogen Explosion Ali Heidari Philosophy of Kingston University of London," Kingston University London, 2012.

[54] L. Li, H.Liao, L. Qi, "An improved r-factor algorithm for TVD schemes," *Int. J. heat mass tranfer*, vol. 51, pp. 610–617, 2008.

[55] A. Harten, "High Resolution Schemes for Hyperbolic Conservation Laws," *J. Comput. Phys.*, vol. 135, no. 2, pp. 260–278, 1997.

[56] H. Jasak, "Error Analysis and Estimation for the Finite Volume Method with Applications to Fluid Flows," PhD thesis, Imperial College London, 1996.

[57] B. van Leer, "Towards the ultimate conservative difference scheme. V. A second-order sequel to Godunov's method," *J. Comput. Phys.*, vol. 32, no. 1, pp. 101–136, 1979.

[58] P. L. Roe, "Some contributions to the modelling of discontinuous flows," in *AMS/SIAM seminar, San Diego*, 1983.

[59] G. D. Van Albada, B. Van Leer, and W. W. Roberts, "A comparative study of computational methods in cosmic gas dynamics," *Astron. Astrophys.*, vol. 108, pp. 76–84, 1982.

[60] P. K. Sweby, "High Resolution Schemes Using Flux Limiters for Hyperbolic Conservation Laws," *SIAM J. Numer. Anal.*, vol. 21, no. 5, pp. 995–1011, 1984.

[61] J. E. Pieters, T. M. Harms, "Investigation of atmospheric boundary layer under different thermal stability conditions," *J. Wind Eng. Ind. Aerodyn.*, vol. 121, pp. 82–97, 2013.

[62] B. R. Cormier, R. Qi, G. Yun, Y. Zhang, and M. Sam Mannan, "Application of computational fluid dynamics for LNG vapor dispersion modeling: A study of key parameters," *J. Loss Prev. Process Ind.*, vol. 22, no. 3, pp. 332–352, May 2009.

[63] M. Metzger, B. J. McKeon, and H. Holmes, "The near-neutral atmospheric surface layer: turbulence and non-stationarity.," *Philos. Trans. A. Math. Phys. Eng. Sci.*, vol. 365, no. 1852, pp. 859–876, 2007.

[64] A. Sathe and W. Bierbooms, "Influence of different wind profiles due to varying atmospheric stability on the fatigue life of wind turbines," *J. Phys. Conf. Ser.*, vol. 75, p. 012056, 2007.

[65] P. Argyle and S. J. Watson, "Assessing the dependence of surface layer atmospheric stability on measurement height at offshore locations," *J. Wind Eng. Ind. Aerodyn.*, vol. 131, pp. 88–99, 2014.

[66] M. Mohan and T. a. Siddiqui, "Analysis of various schemes for the estimation of atmospheric stability classification," *Atmos. Environ.*, vol. 32, no. 21, pp. 3775–3781, 1998.

[67] S. Magidi, "Determining the atmospheric stability classes for Mazoe in Northern Zimbaboe," *Int. J. Eng. Res.*, vol. 3, no. 2, pp. 178–181, 2013.

[68] I. D. Udechukwu, Heidari Ali, Volkov Konstantin, Dembele Siaka, Jeniffer X. Wen, "Investigation of Liquefied Natural Gas (LNG) dispersion using Computational Fluid Dynamics," in *Proceedings of the 11th World congress on computational mechanics (WCCM), July 20-25,* 2014.

[69] R. K. Calay, A. E.Holdo, "Modelling the disperion of flashing jet using CFD," *J. harzadous Mater.*, vol. 154, pp. 198–209, 2008.

[70] P. Midha, M. Ichard and B. J. Artzen, "Validation of CFD modelling of LH2 spread and evaporation against large-scale spill experiments," *Internatinal J. Hydrog. Energy*, vol. 36, pp. 2620–2627, 2011.

[71] A. Parihar, C. Vergara, and J. K. Clutter, "Methodology for consequence analysis of LNG releases at deepwater port facilities," *Saf. Sci.*, vol. 49, no. 5, pp. 686–694, 2011.

[72] P. Cleaver, M. Johnson, B. Ho, "A summary of some experimental data on LNG safety," *J. harzadous Mater.*, vol. 140, pp. 429–438, 2007.

[73] A. Kneebone and L.R. Prew, "Shipboard Jettison Test of LNG onto the Sea," in *Fourth International Conference on LNG, Session 5 paper 5*, 1974.

[74] B. R. Cormier, "Computational Fluid Dynamics for LNG Vapour Dispersion Modelling : A Key Parameters Study," Texas A &M University, 2008.

[75] R. C. Reid, R. Wang, "The boiling rate of LNG on typical dyke floor materials," *Cryogenics (Guildf).*, vol. 18, no. 7, pp. 401–404, 1978.

[76] R. Boe, "Pool boiling of hydrocarbon mixtures on water," *Int. J. Heat Mass Transf.*, vol. 41, no. 97, pp. 1003–1011, 1998.

[77] G. J. Boyle and A. Kneebone, "Laboratory investigations into the characteristics of LNG spills on water," Evaporation, spreading and vapour dispersion," *Am. Pet. Inst. Proj. LNG spills water (Ref. 6Z32). Chester, England, Shell Res. Ltd, Thornt. Res. Cent.*, 1973.

[78] G. F. Feldbauer, J.H. Heigl, W. McQueen, R.H. Whipp and W.G. May, "Spills of LNG on water - vaporisation and downwind drift of combustible mixtures," *Esso Res. Eng. Rep. No. EE61E-72*, 1972.

[79] E. M. Drake and R. C. Reid, "How LNG Boils on Soils", Hydrocarbon Processing," *Hydrocarb. Process.*, vol. 54, no. 5, pp. 191–194, 1975.

[80] J. A. Valencia-Chavez and R.C. Reid, "The effects of composition on the boiling rates of Liquefied Natural Gas for Confined Spills on Water," *Int. J. Heat Mass Transf.*, vol. 22, pp. 831–838, 1979.

[81] E. M. Drake, A.A. Jeje, and R.C. Reid, "Transition boiling of Liquefied Cryogens on a water surface II," *Int. J. Heat Mass Transf.*, vol. 18, pp. 1369–1375, 1975.

[82] AICHE (American Institute of Chemical Engineers), *Guidelines for Chemical Process Quantitative Risk Analysis*, 2nd ed. New York, 2000.

[83] M. Ichard, O.R Hansen, P. Middha and D. Willoughby, "CFD Computation of liquid hydrogen releases," *Internatinal J. Hydrog. Energy*, vol. 37, pp. 17380–17389, 2012.

[84] M. J. Ivings and D.M. Webber, "Modelling bund overtopping using a shallow water CFD model," *J. Loss Prev. Process Ind.*, vol. 20, no. 1, pp. 38–44, 2007.

[85] M. J. Ivings and D.M. Webber, "Development of SPLOT: A numerical model for the two dimensional shallow layer equations," *Heal. Saf. Lab. Rep. C.*, 2002.

[86] M. J. Ivings, E. F. Toro and D.M. Webber, "Numerical Schemes for the 2D Shallow Layer Equation including Dry Fronts," *Comput. Fluid Dyn. J.*, vol. 12, no. 1, pp. 41–52, 2003.

[87] D. M. Webber, M. J. Ivings, W. A Maru, A M. Thyer, "Validation of the shallow water model 'SPLOT' against experimental data on bund overtopping," *Heal. Saf. Exec. Res. Rep. RR755.Health Saf. Lab.*, 2009.

[88] O. R. Hansen, J.A. Melheim and I.E. Storvik, "CFD-modeling of LNG dispersion experiments," in *7thTopical Conference on Natural Gas Utilization*, 2007.

[89] O. R. Hansen, J.A. Melheim and I.E. Storvik, "'Validating the data'LNG Industry (a supplement to Hydrocarbon Engineering)," *Spring Ed.*, pp. 103–107, 2008.

[90] P. F. Linden, Daish, S.B. Dalziel, M.T. Jackson, R.P. Cleaver, A.R. Halford, J.M. Perroux, Wiersma, "LSMS: a new model for spills of LNG and other hazardous liquids," in *Proc. Int. Gas Research Conference. San Diego, California, USA, 8-11 November*, 1998.

[91] J. Moorhouse and R.J. Carpenter, "Factors affecting vapour evolution rates from liquefied gas spills," in *Proc. IchemE Symposium on Refinement of Estimates of the Consequences of Heavy Toxic Vapour Release, UMIST, Manchester, UK, 8 January*, 1986.

[92] Reid, "Boiling of LNG on typical dike floor materials," *Rep. GRI-79/0026, LNG Res. Center, MIT, Cambridge, USA*, 1980.

[93] N. Clark and J. Savery, "The catastrophic failure of containment vessels," *3rdYear Link Proj. Dept. Chem. Eng., Chem. Technol. Imp. Coll. London, Heal. Saf. Exec. Buxt.*, 1993.

[94] B. Dienhart, "'Ausbreitung und Verdampfung von flüssigemWasserstoff auf Wasser und festemUntergrund,'" *(Spreading Vap. Liq. Hydrog. onto water solid ground), PhD Thesis, ForschungszentrumJülich*, 1995.

[95] F. Briscoe and P. Shaw, "Spread and evaporation of liquid," *Prog. Energy Combust. Sci.*, vol. 6, pp. 127–140, 1980.

[96] A. S. Kalelkar and Raj, "Assessment Models in Support of the Hazard Assessment Handbook U.S. Coast Guard Report No. CG-446-3, Report submitted by Arthur D. Little, Inc. to Department of Transportation, U.S. Coast Guard, Contract No. DOT-CG24655A, January 1974." 1974.

[97] D. M. Webber, "A model for pool spreading and vaporisation and its implementation in the computer code GASP"UKAEA Report SRD R507." 1990.

[98] D. M. Webber and S.J. Jones, "A model of spreading vaporising pools"in Proc. International conference on Vapour Cloud Modelling, Boston Massachusetts, USA, ed. J Woodward, pub. AICHE." .

[99] FAY, "Spread of large LNG pools on the sea," *J. Hazard. Mater.*, vol. 140, pp. 541–551, 2007.

[100] V. V. Klimenko, "Film boiling on a horizontal plate—new correlation," *Int. J. Heat Mass Transf.*, vol. 24, pp. 69–79, 1981.

[101] H. W.M. Witlox and A. Oke, "Verification and validation of consequence and risk models for accidental releases of hazardous chemicals to the atmosphere," in *Process Safety Technical Exchange Meeting*, 2007.

[102] S. Atallah, M. Sirdesai and D.M. Jennings', "Source5: A model for creating a DEGADIS input file," *Gas Res. Inst. Rep. GRI-92/0543,* 1993.

[103] J. Havens and T. Spicer, "United states regulations for siting LNG terminals: Problems and potential," *J. Hazard. Mater.*, vol. 140, no. 3, pp. 439–443, 2007.

[104] P. M. O'Farrell and Raj, "Development of additional hazard assessment models U.S. Coast Guard Report No. CG-D-36-77, Report submitted by Arthur D. Little, Inc. to Department of Transportation, U.S. Coast Guard, Office of Research and Development, NTIS AD A042365." 1977.

[105] G. Opschoor, "Investigations into spreading and evaporation of LNG spilled on water," *Cryogenics (Guildf).*, pp. 629–633, 1977.

[106] B. S. E. Launder and B. I, "Applications of energy-dissipation model of turbulence to the calculation of flow near a spinning disc," *Lett. Heat Mass Transf.*, pp. 131–138, 1974.

[107] C. J. Yap, "Turbulent Heat and Momentum Transfer in Recirculating and Impinging flows, PhD thesis, Faculty of Technology, University of Manchester,United Kingdom." 1987.

[108] G. Anand, "I. A Modified k-ε Turbulence Model for High Speed Jets at Elevated Temperatures. II. Modelling and a Computational Study of Spliced Acoustic Liners, PhD thesis, Department of Mathematics,The Florida State University." 2005.

[109] H. A. Panofsky, J.A. Dutton, *Atmospheric Turbulence: Models and Methods for Engineering Applications*. Wiley, New York, 1984.

[110] C. J.H. van den Bosch and R.A.P.M Weterings, *Methods for the Calculation of Physical Effects (TNO Yellow Book), TNO, The Hague, The Netherlands*, Third Edit. 1997.

[111] F. P. Lees, *Loss Prevention in the Process Industries*. Butterworth-Heinemann, Oxford, 1996.

[112] Y. A. Cengel, *Heat and Mass Transfer-A Preactical Approach*. McGraw-Hill, 2006.

[113] R. P. Koopman, J. Baker, R.T Cederwell, H.C Goldwire, Jr., W.J. Hogan, L.M Kamppinnen, R. D. Keifer, J.W. McClure, T.G. McRae, D.L Morgan, L.K. Morris, M.W. Spann and C.D Lind, "Burro Series Data Report LLNL/NWC 1980 LNG Spill Tests,Report number UCID 19075:Lawrence Livermore Natioal Laboratory." .

[114] R. D. Goldwire, H.C. Jr.; Rodean, H.C.; Cederwall, R.T.; Kansa, E.J.; Koopman, R.P.; McClure, J.W.; McRae, T.G.; Morris, L.K.; Kamppinen, L.; Kiefer, "Coyote series data report LLNL/NWC 1981 LNG spill tests dispersion, vapor burn, and rapid-phase-transition. Volume 1." 1983.

[115] T. C. Brown, R.T. Cederwell, D. L. Ermak, R.P. Koopman, J.W. McClure and L.K. Morris, "Falcon Series Data Report 1987. LNG Vapour Barrier Verification Field Trials, Lawrence Livermore National Laboratory,UCRL-CR-104316." 1990.

[116] D. R. Blackmore, G.W. Colenbrander and J.S. Puttock, "Maplin Sands Experiments 1980: Dispersion results from continuous releases of refrigerated liquid propane and LNG," *Nafo Challenges Mod. Soc. - Air Pollut. Model. ifs Appl. 3*, vol. 5, pp. 353–373, 1984.

[117] R. P. Koopman and D. L. Ermak, "Lessons learned from LNG safety research," *J. Hazard. Mater.*, vol. 140, pp. 412–428, 2007.

[118] M. J. Ivings, C. J. Lea, D. M. Webber, S. F. Jagger, and S. Coldrick, "A protocol for the evaluation of LNG vapour dispersion models," *J. Loss Prev. Process Ind.*, vol. 26, no. 1, pp. 153–163, 2013.

[119] A. J. Prince, "Details and results of spill experiments of cryogenic liquids onto land and water, Joint HSE and UKAEA, SRD Report, HSE/SRD/PD058/WP4." 1983.

[120] A. M. Thyer, "Review of data on spreading and vapouriation of cryogenic liquid spills," *J. harzadous Mater.*, vol. 91, pp. 31–40, 2003.

[121] FERC, "Evaluation of DEGADIS 2.1 Using Advisory Bulletin ADB-10-07. U.S. Department of Transportation, Pipeline and Hazardous Materials Safety Administratio:Federal Energy Regulatory Council." 2011.

[122] S. B. King, J. Nordin, D. Sheesley, and T. Routh, "The Department of Energy HAZMAT Spill Center Data Base S. Bruce King, John Nordin, David Sheesley, and Thayne Routh Albany County Research Corporation 365 N. 9." pp. 1–55, 1970.

[123] G. W. Colenbrander, A. Evans, J. S. Puttock, "Spill Test of LNG and Refrigerated Liquid Propane on the Sea, Maplin Sands 1980:Dispersion Data Digest:Trial 27, Shell Research Limited, TNER 84.028." 1984.

[124] G. W. Colenbrander, A. Evans, J. S. Puttock, "Spill Test of LNG and Refrigerated Liquid Propane on the Sea, Maplin Sands 1980:Dispersion Data Digest:Trial 34, Shell Research Limited, TNER 84.030." 1984.

[125] G. W. Colenbrander, A. Evans, J. S. Puttock, "Spill Test of LNG and Refrigerated Liquid Propane on the Sea, Maplin Sands 1980:Dispersion Data Digest:Trial 35, Shell Research Limited, TNER 84.031." 1984.

[126] O. R. Hansen, F. Gavelli, M. Ichard, and S. G. Davis, "Validation of FLACS against experimental data sets from the model evaluation database for LNG vapor dispersion," *J. Loss Prev. Process Ind.*, vol. 23, no. 6, pp. 857–877, Nov. 2010.

[127] M. J. Ivings, S.F. Jagger, C. J. Lea, D.M. Webber, "Evaluating Vapour Dispersion Models for Safety Analysis of LNG Facilities, HSE Report Technical Report." 2007.

[128] U.S. Department of Energy (DOE), "Liquefied Natural Gas (LNG) Safety Research. Report to Congress.," no. May, p. 27, 2012.

Appendix A

Complete discretization of the governing equations

The complete discretization of equation (2-90) is described here, including the method of solution of the resulting linear equation set. Discrete approximation of the integrals is first sought over a representative three dimensional control volume is described here. Each individual term i.e. the time dependent term, the convection

term and the diffusion term are integrated separately in OpenFOAM, first over a control volume, and then over time as described in what follow. The Figure A-1 is a representative control volume chosen for illustration of the integration technique.

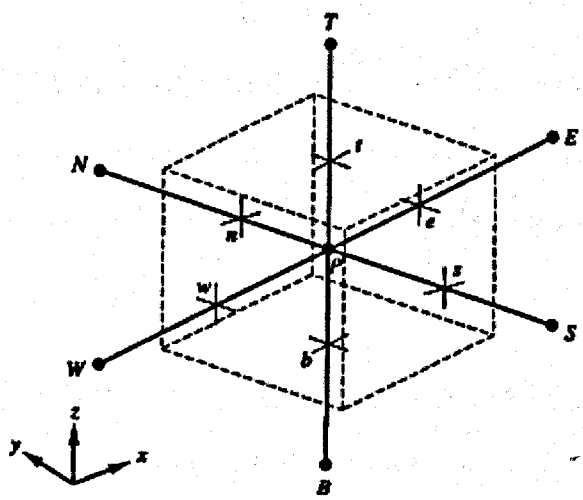

Figure A-1: A representative control volume

The control volume has six neighbouring cells whose central nodes are identified as east, west, north, south, top and bottom (E, W, N, S, T and B) as shown. The notations e, w, n, s ,t and b are used to refer to east, west, north, south, top and bottom faces respectively.

First time derivative

In OpenFOAM, the first time derivative of equation (2-90) is integrated over the control volume by simple differencing in time using Euler Scheme or Backward Euler. With Euler scheme:

$$\int \frac{\partial \rho \phi}{\partial t} \mathrm{dv} \approx \frac{\Delta x \Delta y \Delta x}{\Delta t} (\rho_P^n \phi_P^n - \rho_P^0 \phi_P^0) \tag{A-1}$$

Where $\phi^n \equiv \phi(t + \Delta t)$ denotes the new value at the time-step being solved for and $\phi^0 \equiv \phi(t)$ stands for values at the previous time step, Δx, Δy and Δx are the spatial dimensions of the control volume and Δt is the integration step

Discretization of convective term

The three dimensional form of the convective term $\int(\rho\phi u_i)\cdot \boldsymbol{n}\mathrm{ds}$ can be written as:

$$\int(\rho\phi u_x)\ dA_{yz} + \int(\rho\phi u_y)\ dA_{xz} + \int(\rho\phi u_z)\ dA_{xy} \tag{A-2}$$

Integrating Equation (A-2) above over the surfaces of the control volume yields:

$$\begin{aligned}&[(\rho\phi u_x A)_e - (\rho\phi u_x A)_w] + \left[(\rho\phi u_y A)_n - (\rho\phi u_y A)_s\right]\\ &+ [(\rho\phi u_z A)_t - (\rho\phi u_z A)_b]\end{aligned} \tag{A-3}$$

Here$(\rho\phi u_x)_e$ is the flux of the property ϕ leaving the east face and $(\rho\phi u_x)_w$ is the flux entering the west face. Notice that cell face values are involved in the discretised equation and hence need to be evaluated. This can be achieved by using an interpolation scheme. There exist a number of interpolation schemes, each with specific strength and weaknesses. The most widely used interpolation schemes are discussed here and the one used in current simulations is mentioned later on.

Central differencing

The central differencing scheme represents the simplest interpolation scheme used in CFD and is based on an assumption of linear variation of values of variables between the centres of adjoining cells. Thus, the distance of each node of any two adjoining cells from the target face determines the effect of that node on the face. This entails that the distance from each node acts as a weighting parameter. For the representative control volume represented in Figure A-1, applying the central differencing scheme gives the following for the variable ϕ, on the East face:

$$\begin{cases}\phi_e = (1-\delta_e)\phi_P + \phi_E\\ \delta_e = \dfrac{x_e - x_p}{x_E - x_p} = \dfrac{x_{Pe}}{x_{PE}}\end{cases} \tag{A-4}$$

Using equation (A-4) above and considering the cells to be identical (for simplicity), places the target face half way between the two centroids, such that:

$$\begin{cases} \phi_e = (\phi_E + \phi_P)/2 \\ \phi_w = (\phi_P + \phi_W)/2 \\ \phi_n = (\phi_N + \phi_P)/2 \end{cases} ; \quad \begin{cases} \phi_s = (\phi_S + \phi_P)/2 \\ \phi_t = (\phi_P + \phi_T)/2 \\ \phi_b = (\phi_B + \phi_P)/2 \end{cases} \tag{A-5}$$

A homogeneous isotropic turbulence is then assumed, hence convection fluxes can then be expressed as follows:

$$F = \rho u \tag{A-6}$$

So that equations (A-5) and (A-6) can now be substituted into equation (A-3) and then rearranged in terms of cell centre values to obtain:

$$\begin{aligned} &\frac{F_e A_e}{2}(\phi_E + \phi_P) - \frac{F_w A_w}{2}(\phi_P + \phi_W) + \frac{F_n A_n}{2}(\phi_N + \phi_P) \\ &- \frac{F_w A_w}{2}(\phi_P + \phi_W) + \frac{F_t A_t}{2}(\phi_T + \phi_P) \\ &- \frac{F_b A_b}{2}(\phi_P + \phi_B) \end{aligned} \tag{A-7}$$

Equation (A-7) is the discretised form of the convective term. Also, the values of, F, are evaluated on the faces of the control volume and not at the centre where variables are defined. Thus, similar toϕ, the central differencing can be applied leading to the values summarised in Table A-1.

Table A-1: Evaluation of face values of fluxes using central differencing scheme

F_w	F_e	F_n	F_s	F_t	F_b
$\frac{F_W + F_P}{2}$	$\frac{F_P + F_E}{2}$	$\frac{F_N + F_P}{2}$	$\frac{F_P + F_S}{2}$	$\frac{F_T + F_P}{2}$	$\frac{F_P + F_B}{2}$

A disadvantage of the central difference interpolation scheme is about flow direction changes, where some of the coefficients turn out negative. This can result in an unbounded solution at high Peclet number, a well-known issue with central differencing. To circumvent this issue, higher order interpolation scheme can be adopted for the face values. For instance, the upwind scheme uses values at upwind node rather than taking an average. This makes all coefficients positive thereby help

achieve a bounded solution. But, upwind schemes are not free from limitations as will be seen in the next section.

Upwind scheme

The upwind differencing otherwise called 'donor cell differencing' scheme takes into account flow direction when evaluating cell face values. The convected value of ϕ at a cell face is considered equal to the value at the upstream node. Therefore, depending on the flow direction, cell face values are obtained accordingly. When the flow is in the positive direction (left to right),

$$\phi_e = \phi_P;\ \phi_w = \phi_W;\ \ \phi_t = \phi_P\ ;\ \phi_b = \phi_B;\ \phi_s = \ \phi_S;\ \ \phi_n = \phi_P \qquad \text{(A-8)}$$

Substituting equation (A-8) above into the discretised equation (A-7) and applying the same argument for the convective fluxes gives:

$$[F_P\phi_P A_e - \ F_W\phi_W A_w] + [F_P\phi_P A_n - \ F_S\phi_S A_S] + [F_P\phi_P A_t - \ F_B\phi_B A_b] \qquad \text{(A-9)}$$

Equation (A-9) above is the form of the discretised convective term using the upwind scheme. If the flow is however in the negative direction, the same principle is applied but with the upstream nodes being the reverse of those used for flow in positive direction. The upwind scheme is very stable but only first order accurate. Moreover, this scheme is susceptible to false diffusion.

Hybrid/blended schemes

The hybrid differencing scheme is designed to exploit the favourable properties of upwind and central differencing schemes. It has the capability to switch between central difference and upwind differencing scheme, thereby combine the advantage of both to achieve boundedness and stability. This is achieved through the use of the local Peclet number of flow, which is the ratio of the strength of convection to diffusion, to switch between central differencing and upwind schemes. The Peclet number is expressed as follows:

$$Pe = \frac{\rho u}{\Gamma/_{\delta x}} \qquad \text{(A-10)}$$

Central differencing is used at Peclet number within $-2 < Pe < 2$. Outside of this range, upwind differencing is used with diffusion set to zero. The typical disadvantage of hybrid scheme however, is that it is only first order accurate in terms of Taylor's series truncation error. But it has been widely established to be very useful in in various CFD procedures and is deemed highly stable in comparison to higher order schemes, such as the quadratic upwind differencing scheme (QUICK).

Discretization of diffusive and source term

The diffusion term of Equation (2-90) is expressed in three dimensions as follows:

$$\int\left(\Gamma\frac{\partial\phi}{\partial x}\right)dA_{yz}+\int\left(\Gamma\frac{\partial\phi}{\partial y}\right)dA_{xz}+\int\left(\Gamma\frac{\partial\phi}{\partial z}\right)dA_{xy}+\ S=0 \qquad \text{(A-11)}$$

Integrating equation (A-11) over the control volume shown gives

$$\left[\Gamma_e A_e\left(\frac{\partial\phi}{\partial x}\right)_e-\Gamma_w A_w\left(\frac{\partial\phi}{\partial x}\right)_w\right]+\left[\Gamma_n A_n\left(\frac{\partial\phi}{\partial x}\right)_n-\Gamma_s A_s\left(\frac{\partial\phi}{\partial x}\right)_s\right]$$
$$+\left[\Gamma_t A_t\left(\frac{\partial\phi}{\partial x}\right)_t-\Gamma_b A_b\left(\frac{\partial\phi}{\partial x}\right)_b\right]+\ S\Delta V\ =0 \qquad \text{(A-12)}$$

Applying linear interpolation for all gradients, then linearizing the source term as a function of the dependent variable ϕ, equation (A-12) transforms into:

$$\left[\Gamma_e\frac{\phi_E-\phi_P A_e}{\delta x_{PE}}-\Gamma_w\frac{\phi_P-\phi_W A_w}{\delta x_{WP}}\right]$$
$$+\left[\Gamma_n\frac{\phi_N-\phi_P A_n}{\delta y_{PN}}-\Gamma_s\frac{\phi_P-\phi_S A_s}{\delta y_{SP}}\right] \qquad \text{(A-13)}$$
$$+\left[\Gamma_t\frac{\phi_T-\phi_P A_t}{\delta z_{PT}}-\Gamma_b\frac{\phi_P-\phi_B A_b}{\delta z_{BP}}\right]+(S_u+\ S_P\phi_P)$$

The values of the diffusion coefficients are evaluated on the faces of the control volume and not at the centre where variables are defined. Thus, similar to the gradient terms, some form of interpolation is needed to obtain the cell face values of these coefficients. Again *central differencing* can be used and the values take the form summarised in

Table A--2

Table A-2: Evaluation of face values of coefficients using central differencing scheme

Γ_w	Γ_e	Γ_n	Γ_s	Γ_t	Γ_b
$\frac{\Gamma_W+\Gamma_P}{2}$	$\frac{\Gamma_P+\Gamma_E}{2}$	$\frac{\Gamma_N+\Gamma_P}{2}$	$\frac{\Gamma_P+\Gamma_S}{2}$	$\frac{\Gamma_T+\Gamma_P}{2}$	$\frac{\Gamma_P+\Gamma_B}{2}$

Hybrid schemes have the capability to switch between central difference and upwind differencing scheme, thereby combine the advantage of both to achieve boundedness and stability. This is achieved through the use of the local Peclet number of flow, which is the ratio of the strength of convection to diffusion, to switch between central differencing and upwind schemes. The numerical Peclet number is expressed as follows:

$$Pe = \frac{\rho u}{\Gamma/_{\delta x}} \tag{A-14}$$

Central differencing is used at Peclet number within $-2 < Pe < 2$. Outside of this range, upwind differencing is used with diffusion set to zero

Temporal Discretization

In transient problems such as the one represented by equation (2-90), each of the terms need to be discretised in time as well. Using the Euler Implicit method, the time derivate term can be expressed as:

$$\int_t^{t+\Delta t}\left[\int \frac{\partial \rho\phi}{\partial t}\mathrm{dv}\right]\mathrm{dt} = \int_t^{t+\Delta t}\left[\frac{\Delta x\Delta y\Delta x}{\Delta t}(\rho_P^n\phi_P^n - \rho_P^0\phi_P^0)\right]dt \tag{A-15}$$

$$= \left[\frac{\Delta x\Delta y\Delta x}{\Delta t}(\rho_P^n\phi_P^n - \rho_P^0\phi_P^0)\right]\Delta t$$

For the diffusion, convection and source term discretization, a lumped parameter $L(\phi)$is used here to represent these terms for simplicity. Thus, the combined time integration can be written as:

$$\int_t^{t+\Delta t} L(\phi)\,dt = \int_t^{t+\Delta t} L^*(\phi)\,dt \tag{A-16}$$

Where L^* represents the spatial discretization of L and has been described in previous sections. Then the time integration can be achieved using a wighted average procedure. This methodology states that the time integral of a variable equals a weighted average between current and future values. Assuming that values in a given control volume are known at an initial time t, the values at time $t + \Delta t$ can be expressed.

$$\int_{t}^{t+\Delta t} L^*(\phi)\, dt \;=\; [f\, L^*(\phi)^n + (1-f)L^*(\phi)^0]\Delta t \qquad \text{(A-17)}$$

Where f is a weighting factor and can take values of 0, 0.5 or 1 resulting in Euler explicit, Crank-Nicolson and Euler Implicit schemes respectively. Thus it follows that implicit schemes use the current values, explicit scheme use values at the previous time step while in Crank Nicholson scheme, the average of the new and old values is used. Crank-Nicolson scheme is second order accurate and unconditionally stable. This however does not guarantee obtaining physically realistic results irrespective of the time step and the mesh size used. Therefore it is possible to observe oscillations and physically unrealistic results when using Crank-Nicolson. The stability only means that the oscillations would disappear eventually. Moreover, Crank-Nicolson does not guarantee boundedness. Implicit schemes are first order accurate in time, guarantees boundedness and are unconditionally stable. Explicit schemes are first order accurate but since the values at the current time step depends only on the values of the old time-step, there is no need to form matrix of equations and seek solution for it. Therefore explicit schemes are much simpler and less costly computationally, however, they are limited by the Courant-Friedrichs-Lewy (CFL) condition.

The CFL Condition

This condition requires that in the computation of a flow across a discrete spatial grid, the computational time step has to be very much less than the time it would take the flow to transverse the spatial grid. To achieve this requirement, equation(A-18) which is generally referred to as CFL condition must be satisfied.

$$Co = \frac{u\Delta t}{\Delta x} \leq 1 \qquad \text{(A-18)}$$

The term Co is called the courant number and it is an important limiting factor in CFD simulations. Solution becomes unstable if the condition is not satisfied in a simulation. Therefore, it is recommended in every simulation using explicit scheme to set the Courant number to less than unity and allow the solver to choose time step accordingly.

Solution of the algebraic equations

All along, attention has been focused on the linearization of the governing equations into algebraic form in a process known as discretization. About three different interpolation were analysed. Here, the work is taken a step further by finding an efficient solution for the algebraic equations. Any known solution method can be adopted from this point since no form of solution was assumed during the derivation of the equations. But, it has to be noted that attempt to employ a direct method (no iteration) in three dimensional space will be so complicated and expensive in terms of memory space. This is even worse in a non-linear problem where the equations need to be solved repeatedly with updated coefficients.

Based on the foregoing, iterative method of solution is definitely more appropriate for CFD discretised equations. The iterative approach starts the solution with a guessed value of a dependent variable, such asϕ, and in an iterative procedure, keeps improving the initial guess until successive iterations lead to a converged solution. There are many iterative methods for solving algebraic equations, but the most widely used is the Gauss-Seidel point-by-point method.

Gauss-Seidel method

The Gauss-Seidel method represents the simplest of all iterative techniques. With this method, the values of quantities are obtained by visiting the nodes in a certain order (ϕ , for example). Only one set of $\phi's$ are kept in the computer memory. At the beginning of the solution process, the stored values represent the initial guess or values obtained from a previous iteration. As each the node point is visited, the corresponding value of ϕ in the memory is altered as will be descried shortly. By

rearranging the discretised equations in terms of the cell centred points, the spatial discretised equations can be expressed as

$$a_P\phi_P = \sum a_{nb}\phi_{nb} + b \tag{A-19}$$

In equation (A-19) above, the subscript nb, denote neighbouring cells and, b stand for the linearized source term. Therefore ϕ_P at the visited node point can be calculated from,

$$\phi_P = \frac{\sum a_{nb}\phi_{nb}^* + b}{a_P} \tag{A-20}$$

Where ϕ_{nb}^* denotes the neighbour point values present in the computer memory. If a neighbour has been visited already during the current iteration, the up to date value is then used forϕ_{nb}^*. A complete iteration is considered to have been completed when all the grid points have been visited in this manner. A major drawback of the otherwise appealing Gauss-Seidel method is that it converges too slowly. This is especially worse in problems that involve a large number of grid points. The slowness arises quite understandably from the fact that this method conveys boundary condition information at a rate of one grid interval for each iteration. Fortunately, a procedure exists which can be used to speed up convergence as discussed in what follows.

Under-relaxation and over-relaxation

When solving the linearized algebraic equations, it is often desirable to slow down or speed up the convergence of the iterations. This process is known as *under-relaxation* or *over-relaxation,* depending on whether variable changes are slowed down or accelerated. Considering that slow convergence is the main problem with Gauss-Seidel method, it is normally used in conjunction with over-relaxation, the resulting scheme being referred to as Successive Over-relaxation (SOR).Under-relaxation is used a great deal in nonlinear problems, where it is employed to avoid divergence in the iterative solution of strongly nonlinear equations. There are a number of ways through which over-relaxation or under-relaxation can be introduced. For instance, equation (A-19) can be rewritten in terms of ϕ_P as

$$\phi_P = \left(\frac{\sum a_{nb}\phi_{nb} + b}{a_P}\right) \tag{A-21}$$

Again, by taking ϕ_P^* as the result of the previous iteration on the dependent variable, the adding and subtracting it from the right hand side of equation (A-21) above gives

$$\phi_P = \phi_P^* + \left(\frac{\sum a_{nb}\phi_{nb} + b}{a_P} - \phi_P^*\right) \tag{A-22}$$

Here, the content of the parenthesis clearly represents change in ϕ_P which resulted from the current iteration. This change can be accelerated or slowed down by the introduction of a relaxation factor (Ψ),

$$\phi_P = \phi_P^* + \Psi\left(\frac{\sum a_{nb}\phi_{nb} + b}{a_P} - \phi_P^*\right) \tag{A-23}$$

When the relaxation factor is in the range 0 to 1, it produces under-relaxation effect, such that the values of ϕ_P^* stays close to ϕ_P.When the relaxation factor (Ψ) is more than one, overrelaxation is obtained and the convergence is faster. Thus, a relaxation factor can be chosen during simulation set-up to either speed up or slow the solution process. Solutions in the present study were neither over-relaxed nor under-relaxed as the need did not arise.

Appendix B

Table B-1: errors resulting from arc-wise maximum concentration predictions for coyote trial 3

Arc-radius (m)	Experiment	Predictions	Remark	Actual bias $\frac{X_P - X_M}{X_M} \times 100$
I-PSED				
140 (long time-av)	0.05380	0.0491	Under Prediction	-8.74%
140 (short time-av)	0.10400	0.0760	Under Prediction	-26.9%
200 (long time-av)	0.02830	0.0332	Over Prediction	17.3%
200 (short time-av)	0.05380	0.0420	Over Prediction	21.9%
300 (long time-av)	0.00763	0.0172	Over Prediction	125%
300 (short time-av)	0.01850	0.0210	Over Prediction	13.5%
400 (long time-av)	0.00735	0.0080	Over Prediction	8.84%
400 (short time-av)	0.02040	0.0127	Under Prediction	-37.7%
500 (long time-av)	0.00198	0.0000	Under Prediction	-100%
500 (short time-av)	0.00941	0.0004	Under Prediction	-95%
CONVENTIONAL				
140 (long time-av)	0.05380	0.0699	Over Prediction	29.9%
140 (short time-av)	0.10400	0.1290	Over Prediction	24%
200 (long time-av)	0.02830	0.0337	Over Prediction	19.08%
200 (short time-av)	0.05380	0.0700	Over Prediction	30%
300 (long time-av)	0.00763	0.0179	Over Prediction	134%
300 (short time-av)	0.01850	0.0340	Over Prediction	83.7%
400 (long time-av)	0.00735	0.0100	Over Prediction	36%
400 (short time-av)	0.02040	0.0210	Over Prediction	7.84%
500 (long time-av)	0.00198	0.0000	Under Prediction	-100%
500 (short time-av)	0.00941	0.0001	Under Prediction	-99%

Table B-2: errors resulting from arc-wise maximum concentration predictions for coyote trial 5

Arc-radius (m)	Experiment	Predictions	Remark	Actual bias $\frac{C_P - C_M}{C_M} \times 100$
I-PSED				
140 (long time-av)	0.0512	0.0700	Over Prediction	36.7%
140 (short time-av)	0.1090	0.1300	Over Prediction	19.3%
200 (long time-av)	0.0300	0.0350	Over Prediction	16.7%
200 (short time-av)	0.0740	0.0700	Under Prediction	-5.40%
300 (long time-av)	0.0185	0.0180	Under Prediction	-8.56%
300 (short time-av)	0.0350	0.0320	Under Prediction	-2.70%
400 (long time-av)	0.0100	0.0040	Under Prediction	-60.0%
400 (short time-av)	0.0160	0.0210	Over Prediction	31.25%
500 (long time-av)	0.0020	0.0020	N/A	0.00%
500 (short time-av)	0.0130	0.0160	Over Prediction	23.08%
CONVENTIONAL				
140 (long time-av)	0.0512	0.120	Over Prediction	134.4%
140 (short time-av)	0.1090	0.170	Over Prediction	55.9%
200 (long time-av)	0.0300	0.060	Over Prediction	100.0%
200 (short time-av)	0.0740	0.093	Over Prediction	25.7%
300 (long time-av)	0.0185	0.020	Over Prediction	8.1%
300 (short time-av)	0.0350	0.040	Over Prediction	14.3%
400 (long time-av)	0.0100	0.010	N/A	0.0%
400 (short time-av)	0.0160	0.028	Over Prediction	75.0%
500 (long time-av)	0.0020	0.005	Over Prediction	150.0%
500 (short time-av)	0.0130	0.021	Over Prediction	61.5%

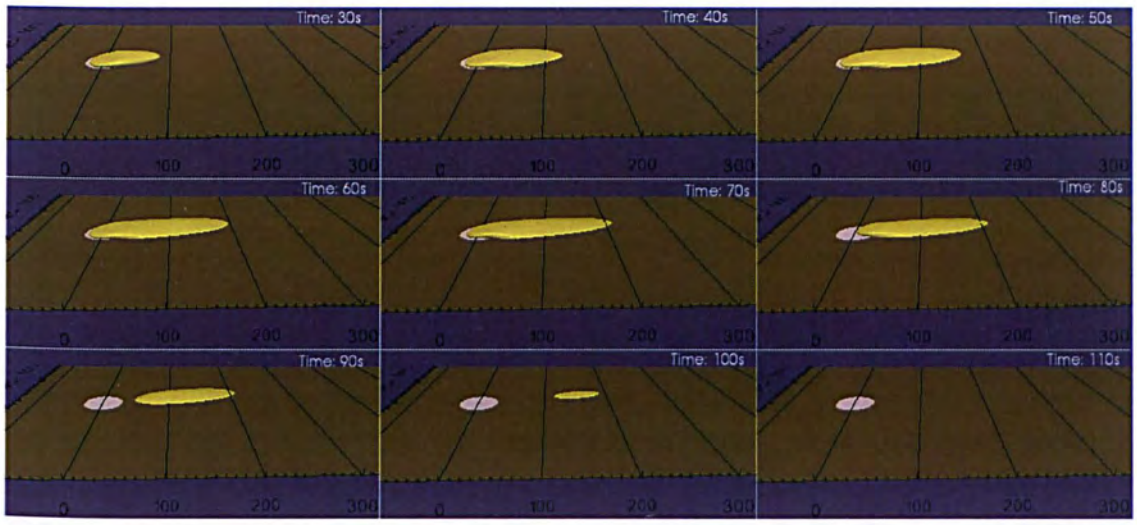

Figure B-1: Snapshots of LFL contours for test Coyote 3

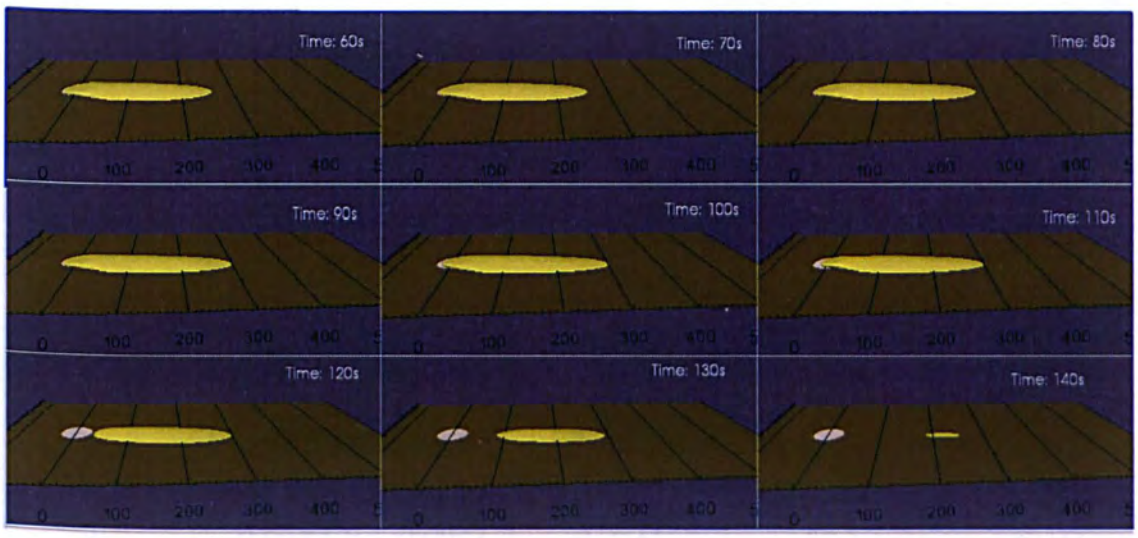

Figure B-2: Snapshots of LFL contours for test Coyote 5

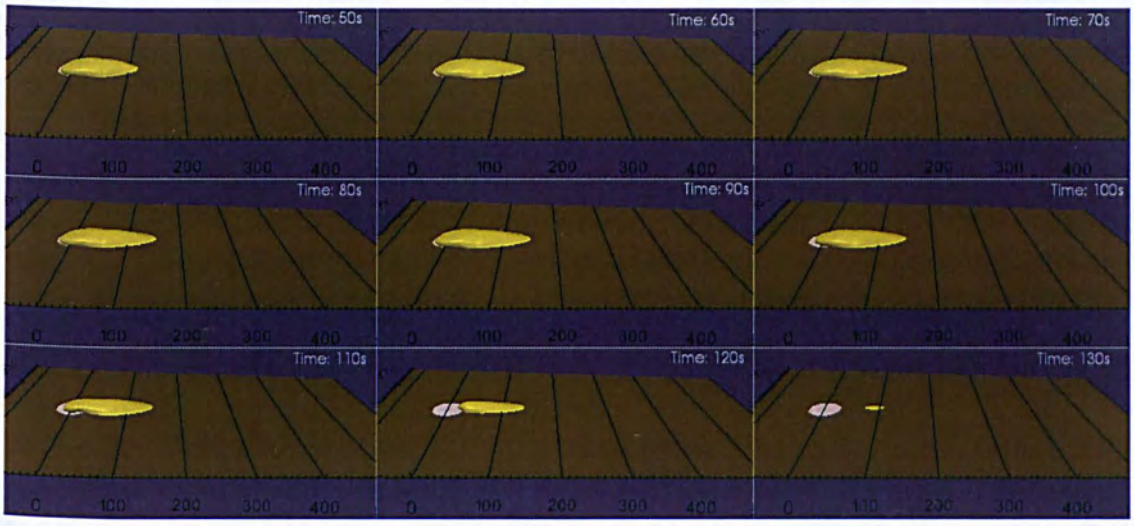

Figure B-3: Snapshots of LFL contours for test Coyote 6

Table B-3: Percentage errors associated with the CFD Predictions of Maplin 35

Arc radius(m)	Experiment	I-PSED	Conventional	% Bias (I-PSED)	% Bias (Conventional)
58	0.1340	0.1077	0.0603	-19.63	-55.00
88	0.0989	0.0943	0.0534	-4.65	-46.00
129	0.0775	0.0803	0.0467	3.61	-39.74
250	0.0321	0.0499	0.0318	55.45	-0.93
399	0.0267	0.0296	0.0199	10.86	-25.47